Radiative Heat Transfer with Nanowire/Nanohole Metamaterials for Thermal Energy Harvesting Applications

by

Jui-Yung Chang

A Dissertation Presented in Partial Fulfillment
of the Requirements for the Degree
Doctor of Philosophy

Approved October 2017 by the
Graduate Supervisory Committee:

Liping Wang, Chair
Patrick Phelan
Robert Wang
Hongbin Yu
Owen Hildreth

ARIZONA STATE UNIVERSITY

December 2017

ABSTRACT

Recently, nanostructured metamaterials have attracted lots of attentions due to its tunable artificial properties. In particular, nanowire/nanohole based metamaterials which are known of the capability of large area fabrication were intensively studied. Most of the studies are only based on the electrical responses of the metamaterials; however, magnetic response, is usually neglected since magnetic material does not exist naturally within the visible or infrared range. For the past few years, artificial magnetic response from nanostructure based metamaterials has been proposed. This reveals the possibility of exciting resonance modes based on magnetic responses in nanowire/nanohole metamaterials which can potentially provide additional enhancement on radiative transport. On the other hand, beyond classical far-field radiative heat transfer, near-field radiation which is known of exceeding the Planck's blackbody limit has also become a hot topic in the field.

This PhD dissertation aims to obtain a deep fundamental understanding of nanowire/nanohole based metamaterials in both far-field and near-field in terms of both electrical and magnetic responses. The underlying mechanisms that can be excited by nanowire/nanohole metamaterials such as electrical surface plasmon polariton, magnetic hyperbolic mode, magnetic polariton, etc., will be theoretically studied in both far-field and near-field. Furthermore, other than conventional effective medium theory which only considers the electrical response of metamaterials, the artificial magnetic response of metamaterials will also be studied through parameter retrieval of far-field optical and radiative properties for studying near-field radiative transport. Moreover, a custom-made AFM tip based metrology will be employed to experimentally study near-field radiative

transfer between a plate and a sphere separated by nanometer vacuum gaps in vacuum. This transformative research will break new ground in nanoscale radiative heat transfer for various applications in energy systems, thermal management, and thermal imaging and sensing.

ACKNOWLEDGMENTS

Five years and a half is not a long time in our lives if we live long enough, but for sure, this is a period of time I will never forget in the rest of my life. No one will say perusing a degree is easy. However, with all the help I received these years, I will say I lived a colorful American dream with laughter and tears. First, I would like to thank my families. My wife Chiao-Hui is the one who takes care of me every day and stays by my side no matter what happened; she made my life 100 times easier. Without her, I'm not even sure if I can earn my degree at the end. Furthermore, without my parents Hsi-Hsiung and Chieh-Feng, I wouldn't even think of leaving my country and my comfort zone to get a PhD degree here. Of course, their financial support is also one of the most important things I need to focus on research. Also, if it is not because of the virtual and mental supports from my sisters Jui-Han and Jui-Ko, my parents in law Chao-Pin and Yu-Chen, and my brother in law Justin, I don't even think I can reach this stage and write these acknowledgments. I really appreciate all the help I received from my families, they are the best!

Second, I would like to thank all my committee members and ASU faculties. My advisor Prof. Liping Wang trained and helped me to accomplish what is required for a doctor title. Committee members Profs. Patrick Phelan, Robert Wang, Hongbin Yu, and Owen Hildreth helped me a lot on my comprehensive exam, defense, and my dissertation. I've learned a lot from them about how to do theoretical research and experiments. I would also like to thank Prof. Konrad Rykaczewski and Dr. Bruce Steele, they trained me to become a responsible teaching assistant. Moreover, ASU faculties Susan Terkelsen,

Christine Quintero, and Shannon Pete helped me more than I could even imagine on all the school issues and degree requirements so that I can focus myself fully on my research.

At the end, I would like to thank my lab mates/best friends for life: Hao, Yue, Hassan, Sydney, Payam, Xiaoyan, Linshuang, Qing, Xiaoda and Viraj. They stood beside me all the way on this adventure, and I am so lucky to have them in my life for the rest of my life. I could not have achieved what I have right now without anyone of them. I would also like to thank Akshat, Hang, Nate, Pouya, Lee, and Niko, who worked with me in our lab and helped me a lot on my research. On the other hand, I want to give special thanks to Mirza and Leah, who helped me a lot on adapting the culture and life here while we worked together on our first class project. I am truly grateful for all the help I received; I also hope I can return the favor some day in the future.

TABLE OF CONTENTS

Page

CHAPTER Page

LIST OF TABLES

Table Page

LIST OF FIGURES

Figure Page

CHAPTER 1 INTRODUCTION

1.1 Potential Impact and Applications of Metamaterials

For the past few decades, materials that naturally exist on earth can no longer catch up with the rapid improvement of technology and artificial materials that fit the diversified needs of scientists become a new frontier to explore. Micro and nano structured materials, also known as metamaterials, jumped into the scope of radiative heat transfer related applications while tuning the radiative surface properties can easily be achieved by finding suitable materials and geometric features. This is due to the fact that the radiative behaviors of the materials can be tailored by tuning the resonance frequency of the dominating enhancement mechanism caused by the micro/nano structure such as surface plasmon/phonon polariton [1], interference effect [2], wave guide mode [3], Wood anomaly [4], hyperbolic mode [5], epsilon-near-zero and epsilon-near-pole [6], and magnetic polariton [7]. These mechanisms, either affect spectral radiative transport in broad or narrow frequency bands, can be used to construct components for applications such as energy harvesting [8], imaging [9], and sensing [10]. Nowadays, metamaterials based on gratings [11], multilayer [12], and nanowire/nanohole [13, 14] structures are already widely investigated. Among them, nanowire/nanohole structures are advantageous over multilayers that suffer from thermal stress issue and submicron periodic grating metamaterials whose large-area fabrication is prohibited.

1.2 Unique Characteristics of Nanowire/Nanohole Metamaterials

Recently, metamaterials made of vertically aligned nanowire/nanohole arrays have been extensively studied in aspect of negative refraction, selective absorbers and emitters

based on different mechanisms [15, 16]. Excitation of magnetic polariton (MP) is one fundamental mechanism to obtain exotic radiative properties within metamaterials [17-19]. MP refers to the coupling between incident electromagnetic wave and internal magnetic resonance inside the structure, and its excitation has been widely investigated for 1D and 2D gratings, disk arrays, cross bars, and ring arrays [17, 20, 21]. However, effective medium approximation which has widely been employed to investigate nanowire-based metamaterials only considers the response to the electric field (i.e., the metamaterial is usually assumed to be non-magnetic). The validity of the effective medium theories would become questionable, and it needs to be reconsidered if magnetic resonance could be excited inside nanowire-based metamaterials, which has not been well understood.

1.3 Near-Field Thermal Radiation

Due to the coupling of evanescent waves, near-field radiation can overcome the far-field Planck blackbody limit and has become a hot topic in the field of energy harvesting [22, 23] and thermal management [24, 25] when the vacuum gap distance between the emitter and receiver is less than the characteristic thermal wavelength [23]. In particular, near-field radiation can be further enhanced by coupling the surface plasmon/phonon polaritons (SPP/SPhP) of the interfaces on either side of the nanometer vacuum gap [26-28]. Several studies have been performed in order to enhance the near-field heat flux due to coupled surface modes in terms of different materials as well as structures [13, 29-31]. Furthermore, since coupled SPP/SPhP mode is usually unexcitable between dissimilar materials or can only be excited within a narrow band; hyperbolic metamaterial (HMM) however, is a promising mechanism on enhancing near-field radiation between dissimilar

materials which is known by its unlimited length of wavevector (high-k mode) [32, 33] and broadband enhancement on photonic density of state (PDOS) [34, 35]. Even though these two mechanisms are widely used and can highly enhance the near-field radiative heat transfer, these two modes are both excited due to the electrical response of the material which associates with electrical permittivity while the magnetic response of the material is again usually neglected [27, 28].

1.4 Primary Objective of This Research

Recently, several researches have shown the possibility of artificial magnetic response for metamaterials [17, 20, 36, 37], which results in the fact that neglecting the response to magnetic waves might no longer be a feasible assumption. My PhD research aims to understand the electrical and artificial magnetic responses of nanowire/nanohole based metamaterials in both far-field and near-field. Materials such as tungsten, indium tin oxide (ITO), doped silicon and graphene are used here in order to excide different physical mechanisms to enhance or manipulate radiative heat transfer. This research aims to answer several major fundamental questions in the following:

- Could magnetic response be achieved artificially in the optical region with nanowire metamaterials?
- Could nanowire metamaterials improve the solar thermal energy systems?
- What are the fundamental effects of nanowire/nanohole based metatarsals in near-field radiative transfer?
- Could nanowire metamaterials improve near-field TPV systems with higher performance?

- How to account the artificial magnetic response of metamaterials in homogenization methods?
- How does the artificial magnetic response impact the near-field radiative transfer?
- How to experimentally validate the effects of nanowire metamaterials in both far-field and near-field thermal energy systems?

For far-field radiation, the spectral absorptance of a tungsten nanowire array is theoretically analyzed. Although optical behaviors of metal nanowire arrays have already been widely studied and explained, this is the first time the enhancement mechanism is explained by magnetic polaritons (MP) which is based on the artificial magnetic response of metamaterials. Furthermore, an LC circuit model is also presented the first time between nanowires to predict the occurrence of enhancement peaks on spectral absorptance. In addition, the tungsten nanowire structures are systematically studied potentially as high-efficiency solar thermal absorbers for enhancing solar thermal energy harvesting.

For near-field radiation, electrical responses of metamaterials are first analyzed theoretically by effective medium theory (EMT) for different enhancement mechanisms that can be excited. In order to overcome the weak coupling between dissimilar materials, graphene is introduced on the receiver to couple the surface wave of doped silicon nanohole emitter and thereby increase the radiative heat transfer. Furthermore, hyperbolic mode and the effect of special dispersion on EMT are also studied between two ITO nanowire arrays. These studies give a fundamental understanding of some of the most important physical mechanisms in the near-field. One step further for systematic applications of nanowire structures, an emitter made of tungsten nanowire array embedded alumina is introduced in a thermophotovoltaic (TPV) system to improve the performance and efficiency of the cell.

This is the first time hyperbolic mode been used in TPV systems since broadband enhancement usually deteriorates the efficiency. By studying the effect of thin film TPV cells, the problem has been overcome and the possibility of exciting different mechanisms to improve TPV systems is suggested.

Artificial magnetic response of nanowire based metamaterials are also investigated in the near-field. This is crucial for near-field radiative heat transfer because magnetic material property does not naturally exist within the visible or infrared wavelength/frequency range and therefore artificial magnetic responses cannot be predicted by field averaging homogenization methods. The effect of artificial magnetic response is first studied by arbitrary material properties where physical mechanisms that can possibly be excited are targeted. Then by introducing parameter retrieval, which is based on the reflection and transmission coefficients of metamaterials simulated by finite-difference time-domain method, the artificial magnetic response can be considered by the permeability of metamaterials that contributes to the radiative heat transfer. This method provides extra tunability on manipulating radiative heat transfer as well as better accuracy on simulations since both electric and magnetic responses are included.

The last part of my dissertation (recommendations) is focused on a sphere-to-plate near-field radiative heat transfer experiment. This is one of the state of the art methods to measure near-field radiative transport at nanometer vacuum gaps. Instead of using a commercial atomic force microscope (AFM), I designed and built a homemade AFM probe based metrology for near-field radiation experiments in vacuum. In fact, this metrology is also a foundation of future research since it can be further modified for applications such

as near-field scanning optical microscope, near-field infrared spectroscopy, near-field imaging and manufacturing, etc.

The main goal of this dissertation is to understand the behavior of nanowire/nanohole based metamaterials in both far-field and near-field in terms of electrical and artificial magnetic responses. For far-field radiative heat transfer, a nanowire based metamaterial is first analyzed as a selective solar absorber in terms of its artificial magnetic response and systematic performance in Chapter 2. Next, for near-field radiative transport, the fundamental studies of nonmagnetic nanowire/nanohole based metamaterials is discussed in Chapter 3. Chapter 4 takes one step further and focuses on the application of nanowire metamaterials in near-field energy harvesting systems. As for the effect of artificial magnetic response of metamaterials, Chapter 5 presents the effects of uniaxial permeability as well as the retrieval process and the modified near-field theory. Finally, the conclusion and recommendations will be provided in Chapter 6 which illustrates the experimental setup and procedure of a sphere-plate based near-field experiment.

CHAPTER 2 MAGNETIC NANOWIRE METAMATERIALS IN FAR-FIELD ENERGY HARVESTING SYSTEMS

In this section, we will employ the finite-difference time-domain (FDTD) method to numerically study the optical and radiative properties of vertically aligned tungsten nanowires sitting on a tungsten thin film, which can potentially serve as an efficient selective solar thermal absorber. Resonance behaviors within the tungsten nanowire structures are observed in the short wavelengths, leading to enhanced solar absorption, while reflective nature of tungsten in the IR leads to a high reflectance in that spectral region. A comparison will first be made between the radiative properties obtained by the EMT and the FDTD simulation, in order to check the validity of EMT when MP is excited inside nanowire-based metamaterials. Furthermore, the electromagnetic field distribution at the resonance wavelengths will be presented, which clearly shows the exact MP behaviors of different modes. Moreover, an analytic inductor-capacitor (LC) circuit model will be introduced based on the electromagnetic field distribution to quantitatively predict the resonance wavelength of MP, further confirming the excitation of MP from the comparison with the FDTD simulation. The study on the geometric effects such as unit cell period, nanowire diameter, and nanowire height will be performed as well in order to fully understand the MP behavior in nanowire-based metamaterials. In addition, the incidence angle dependency on the optical properties and the conversion efficiency of the nanowire based absorber will also be studied.

2.1 Selective Absorption by Nanowire Metamaterials

As illustrated in Fig. 2.1(a), the selective solar absorber is constructed by vertically aligned tungsten nanowire array deposited on a tungsten thin film. Geometric parameters *P*, *D*, and *H* represent the array period, nanowire diameter, and height, respectively. The directions of electric field and magnetic field of a transverse magnetic (TM or p-polarized) wave at normal incidence are also illustrated in the figure respectively by $\vec{\mathbf{E}}$ and $\vec{\mathbf{H}}$. Note that, for normal incidence, the radiative properties of the selective absorber such as spectral absorptance under different polarized waves will be the same due to the geometric symmetry on for nanowires. The tungsten thin film substrate will be considered as optically opaque as its thickness is set to be 500 nm.

Radiative properties of the designed selective solar absorber were obtained by FDTD method (Lumerical Solutions, Inc.) within the wavelength range between 0.3 μm to 4 μm with 200 data points. Here, excellent numerical convergence is ensured by comparing the results with those obtained from 1851 wavelength points (i.e., a 2-nm interval). The optical property of tungsten is obtained from Palik's tabular data and assumed to be independent of temperature [38]. A plane-wave source with 0° polarization angle (TM wave as illustrated in Fig. 2.1 (a) is placed above the absorber. Bloch boundary conditions which account for phase shifts between each period are established on both x and y directions for simulating periodic structures, while perfectly matched layers were set on z direction to avoid wave reflections from simulation domain boundaries. A minimum mesh size of 4 nm is used with non-uniform meshing while the numerical error is less than 0.5% compared to the simulation using a minimum element size of 3 nm. Since the tungsten thin film substrate is thick enough to be opaque, the spectral absorptance α_λ of the selective absorber can then

be obtained as $\alpha_\lambda = 1 - R_\lambda$ with R_λ obtained from a frequency-domain field and power monitor located above the plane-wave source.

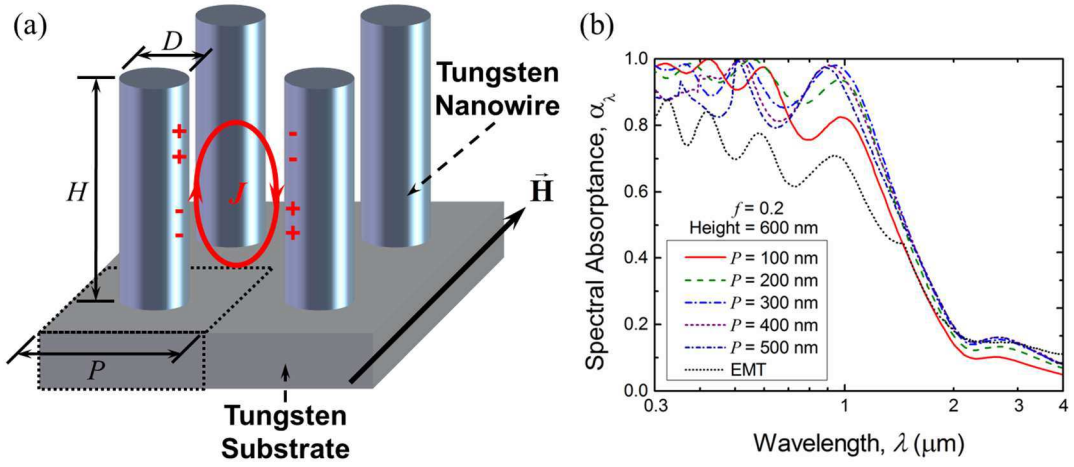

Fig. 2.1 (a) Schematic of the tungsten nanowire based selective absorber; and (b) the spectral absorptance of the selective absorber based on FDTD simulation and EMT with fixed filling ratio.

An inhomogeneous nanowire array can be approximated as a homogeneous medium with widely used effective medium theories, which are homogenization approaches based on field average method [39]. For small filling ratios $f = \pi D^2/(4P^2) < 0.5$ considered in this study, the Maxwell-Garnett EMT method gives the effective dielectric functions as [40]:

$$\varepsilon_{\parallel,\mathrm{eff}} = \frac{(\varepsilon_\mathrm{W} + 1) + \mathrm{f}(\varepsilon_\mathrm{W} - 1)}{(\varepsilon_\mathrm{W} + 1) - \mathrm{f}(\varepsilon_\mathrm{W} - 1)} \tag{2.1}$$

$$\varepsilon_{\perp,\mathrm{eff}} = 1 + f(\varepsilon_\mathrm{W} - 1) \tag{2.2}$$

where subscript W, (∥,eff), and (⊥,eff) denote tungsten, the parallel (in x-y plane) and vertical (out of plane) components of dielectric functions, respectively. Note that, the variation of geometric parameters can only take effect by changing the filling ratio of the

nanowire array. That is, the dielectric functions stay the same even with different array period and nanowire diameter as far as the filling ratio is fixed.

Previously, two methods (i.e., FDTD and EMT) are introduced to acquire the radiative properties of the designed structure. Now, let us first compare the results obtained from EMT with the results from FDTD to check its validity as FDTD is a full-wave simulation which numerically solves the Maxwell equations in every mesh element. The geometric parameters of the selective solar absorber are set to be D = 150 nm, P = 300 nm, and H = 600 nm, which are used as base values to excite resonances within the solar spectrum. These geometric parameters are chosen considering the possibility of fabrication as well as the distinguishability of absorption peaks. The presented structure can be possibly fabricated by directional solidified eutectic NiAl–W alloy [41] while the tungsten substrate is sputtered before etching the NiAl host. As shown in Fig. 2.1(b), the spectral absorptance obtained from FDTD and EMT are different from each other in magnitude, while the EMT could obtain similar oscillating resonance peaks but cannot accurately predict the absorptance in comparison with FDTD results with the same geometric parameters (P = 300 nm). Due to the fact that the results of EMT calculation will not change under fixed filling ratio f, this figure also illustrates the spectral absorptance with fixed f but different array period and nanowire diameter in order to verify the accuracy of the results from EMT calculation. Clearly, the simulation result shows that the resonance peaks blue shift to shorter wavelengths when increasing the array period. On the other hand, EMT predicts the same spectral absorptance distribution with fixed f. Therefore, the EMT is proven to be inaccurate for predicting the optical response of considered tungsten nanowire structures. Furthermore, since EMT is a homogenization process which is not able to

predict the resonance effects inside the material but only the bulk response, this can also show that the enhancement peaks are caused by resonance effects between the nanowires instead of the bulk responses of the structure such as interference effect.

In order to understand the resonance effect indicated by spectral absorption peak, the electromagnetic field distributions are calculated by FDTD at resonance wavelengths: (a) 2.67 μm, (b) 0.93 μm, and (c) 0.52 μm are presented in Fig. 2.2. The contour plots show the magnetic field normalized to the incident field and the arrows represent the electric field vector. It can clearly be seen in Fig. 2.2 (a) that there is a strong magnetic energy confinement between the nanowires. Furthermore, the electrical field vectors on both sides of the energy confinement are pointing at opposite directions (pointing down on right and up on left) while that inside the substrate points towards the left. This indicates that while the electric field forms a loop surrounding the confining region (blue circle). The similar behavior has been observed in grating-based metamaterials, which has been proven to be the resonance of MP [7]. When the excitation of MP is induced by the incident electromagnetic fields, an oscillating resonant electrical current caused by the free charges at the surface is generated inside the nanowire structures. The resonant electrical current loop oscillates between neighboring nanowires with strongly confined electromagnetic energy in the air gap, resulting in the enhancement of spectral absorptance/emittance at resonance wavelengths. Furthermore, higher harmonic modes of MP (i.e., MP2 and MP3) which contribute to the selective absorptance near visible range can also be obtained by FDTD simulation at shorter resonance wavelengths as shown in Figs. 2.2(b) and 2.2(c). For the selective solar absorber, all harmonic MP modes are very important to achieve high

broadband absorption. Note that the surface plasmon polariton resonance cannot be excited in the visible range since the real part of tungsten permittivity is positive within the range.

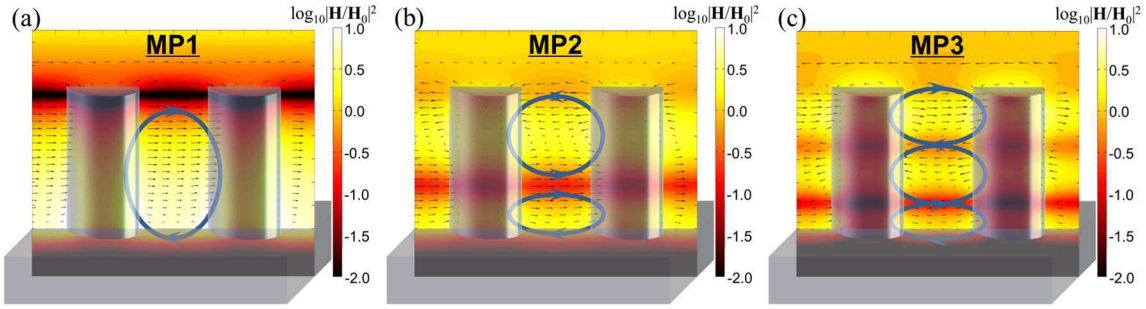

Fig. 2.2 The contour plots of electromagnetic field distribution on the x-z plane when MP resonances are excited at wavelengths of (a) 2.66 μm, (b) 0.93 μm, and (c) 0.52 μm.

2.2 Inductor-Capacitor Circuit Model and Geometric Effects for Nanowire Metamaterials

As demonstrated by previous works [36, 42, 43], an analytical inductor-capacitor (LC) model based on surface charge distribution at MP resonance wavelength has been successfully used for predicting the resonance condition for grating based metamaterials. However, one major challenge in developing the LC model is the difficulty to quantify the inductance and capacitance due to the curved nanowire surface. Here, we propose a modified LC model by simplifying the nanowires to an effective plate, based on the similar strongly localized magnetic field distributions. The LC circuit model between two closely spaced and vertically aligned nanowires is presented by Fig. 2.3(a), where the air gap between two neighboring nanowires forms a capacitor C_g, $L_{m,NW}$ is the mutual inductance between nanowires, $L_{k,NW}$ and $L_{k,SUB}$ are the kinetic inductance contributed by the drifting electrons in nanowires and substrate, respectively. Therefore, the total impedance of the LC circuit can be expressed as:

$$Z_{\text{total}} = i\left[\omega(2L_{\text{m,NW}} + 2L_{\text{k,NW}} + L_{\text{k,SUB}}) - \left(\omega C_{\text{g}}\right)^{-1}\right] \tag{2.3}$$

Thus by zeroing the total impedance of the circuit, the MP resonance wavelength of the fundamental mode can be obtained as:

$$\lambda = 2\pi c\sqrt{C_{\text{g}}(2L_{\text{m,NW}} + 2L_{\text{k,NW}} + L_{\text{k,SUB}})} \tag{2.4}$$

Now, the challenging part of constructing the LC circuit model is to quantify the capacitance and inductances due to the curvy surface of the nanowire. Considering that the LC circuit model is a simple estimation method, it would not be worthwhile to integrate the parameters over the circular nanowire surfaces and end up with complicated expressions, which would defeat the purpose of the LC model. Instead, we chose to simplify the problem by approximating the nanowires as effective parallel plates with spacing in between, setting the non-uniform charge distribution factor c_1 as 0.4, and setting the effective penetration depth δ_{eff} as $3\delta_{\text{W}}$ based on the electromagnetic field distribution. In this way, all the formulae of capacitance and inductance for deep gratings, which can be found in Refs. [36, 43, 44] and will not be repeated here, can be directly adopted for nanowires as effective parallel plates.

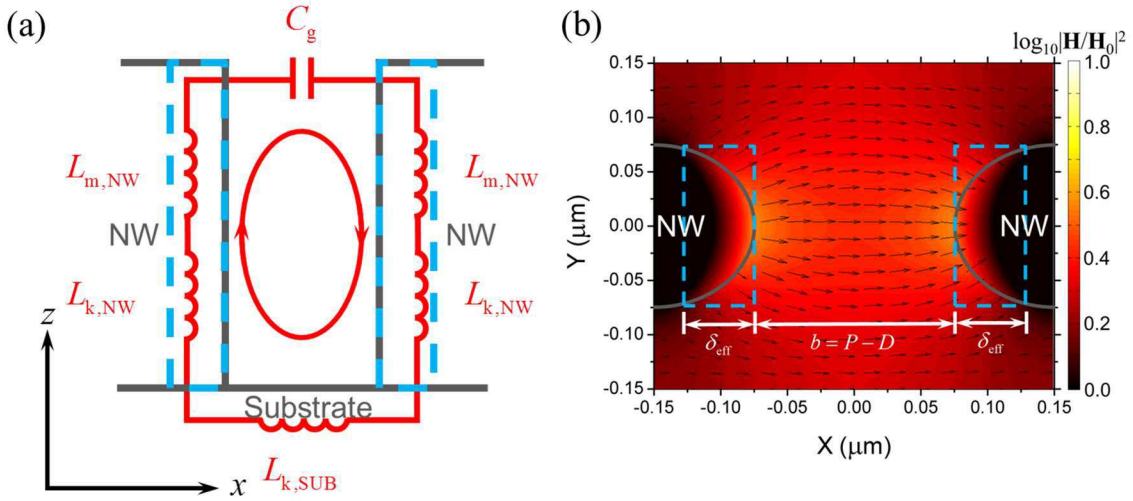

Fig. 2.3 (a) The LC circuit model based on charge and field distribution and (b) the electromagnetic field distribution on the x-y plane located at 0.3 μm above the bottom of the nanowires when MP is excited at 2.66 μm in wavelength.

Figure 2.3 (b) reveals the electromagnetic field distribution in x-y plane located at 0.3 μm above the bottom of the nanowires (i.e., at the middle of the nanowires) when MP1 resonance is excited (2.66 μm). Based on the strength of the magnetic field, the effective penetration depth δ_{eff} within the effective plates is thereby taken as three times of that within the bulk tungsten, which is $\delta_{\text{W}} = \lambda/4\pi\kappa$ with κ being the wavelength-dependent extinction coefficient. The capacitance and the inductance are then calculated by the geometric parameters of the effective plates according to the LC circuit model for deep gratings [7, 44]. As a result, the resonance wavelength of MP1 on the base geometry predicted by the LC circuit model is 2.82 μm compare to 2.66 μm obtained from FDTD simulation with 6% relative error, confirming that the resonance is actually due to excitation of magnetic resonance.

The main goal of the study is to achieve selective spectral absorptivity for efficient solar absorbers. In other words, near-unity absorptance in the solar spectrum and near-zero spectral emittance/absorptance (spectral absorptance = spectral emittance according to Kirchhoff's law) in the infrared regime is required. One of the most beneficial features of MP resonance is the tunability provided by geometric parameters as illustrated by Fig. 2.4. As shown by Fig. 2.4(a), the spectral absorptance peaks at MP resonances blue shift to shorter wavelengths (where most of the solar energy is distributed) when increasing the array period and fixing the diameter and height. Meanwhile, the amplitude of the enhancement peaks at shorter wavelengths also increased to near-unity. On the other hand,

the resonance peak of MP1 is suppressed which is opposite to higher harmonic modes under larger array period. All these phenomena would benefit the design of selective solar absorber.

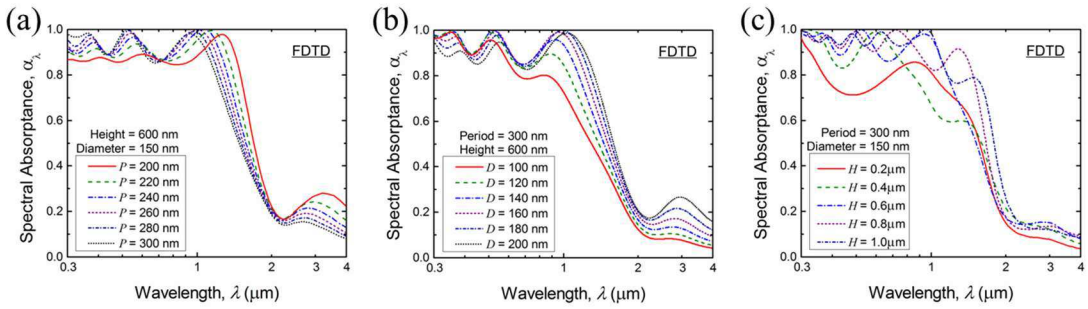

Fig. 2.4 The spectral absorptance with respect to different nanowire (a) array period, (b) diameter, and (c) height simulated by FDTD.

Figure 2.4(b) indicates that increasing nanowire diameter or decreasing the air gap under fixed *P* and *H* lead to opposite trend of spectral absorptance tunability as it results in smaller air gap. Both the red shifting and the increase of magnitude of the resonance peaks can clearly be observed. However, the higher harmonic terms of MP resonance maintains red shifting but again a reverse trend of the enhancement strength occurs. This is due to the fact that with a smaller air gap, energy can be better confined between neighboring nanowires under higher harmonic terms of MP resonance. Figure 2.4(c) shows the effect of nanowire height on spectral absorptance with both *P* and *D* fixed. The blue shifting of resonance peaks are clear, but the tunability of *H* on spectral absorptance enhancement is not that obvious. Furthermore, the effect of high harmonic resonance terms cannot be seen as the nanowires are too short. Note that, when it comes to fabrication process, the uncertainties of fabrication might lead to the shifting of enhancement peaks as shown in Fig. 2.4. More specifically, an uncertainty at the order of tens of nanometer on either period

or diameter will lead to slight shift of the resonance peaks which will little affect the performance of the absorber. On the other hand, the uncertainty on nanowire height will affect the performance significantly when it is on the order of micrometer.

The resonance wavelengths of MP1 with different geometric parameters obtained by FDTD simulation are also compared with that predicted by LC circuit model. As shown by Fig. 2.5(a), the blue shift of resonance wavelength with increasing unit cell period can clearly be seen while the result of LC circuit model also presents the same trend. As for the effects of nanowire diameter and height as shown by figs. 2.5(b) and 2.5(c), similar trends are also observed which can further verify the accuracy and rationality of the LC circuit model presented in this study.

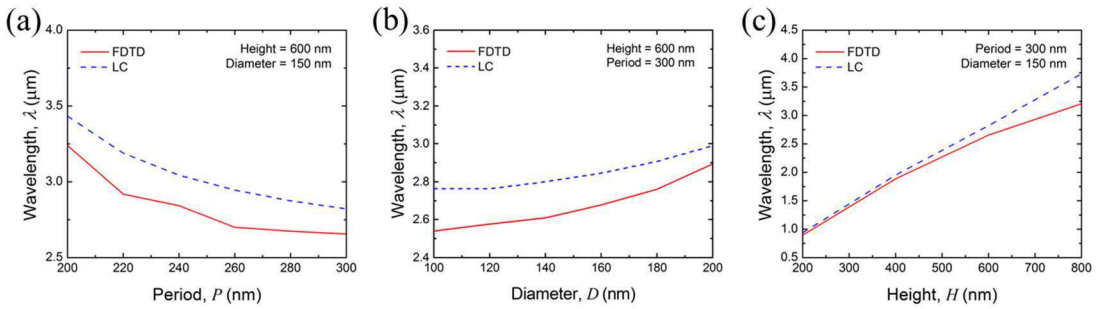

Fig. 2.5 The MP1 wavelengths predicted by FDTD and LC circuit model with respect to different nanowire (a) array period, (b) diameter, and (c) height.

As for the practicability of a selective solar absorber without tracing devices under sunlight (considered as randomly polarized or unpolarized wave), the dependence of incidence angle is also important and need to be studied. Figures 2.6(a) and 2.6(b) illustrates the incident angle dependence of the spectral absorptance at MP2 and MP3 respectively for TE and TM waves. The two wavelengths (0.93 μm for MP2 and 0.52 μm for MP3) are selected since these two enhancement peaks are the main resonance that can

be tuned to the visible regime by geometric parameters. As shown in Fig. 2.6, for both TE and TM waves, these two resonance peaks show great independency for incidence angles up to ±60°. That is, the spectral absorptance can still reach about 0.8 at ±60° for TE waves and even at ±75° for TM waves. Furthermore, both two peaks maintain at above 0.9 within ±30° for TE waves and ±45° for TM waves. This can greatly reduce the cost of selective solar absorbers by providing large clearance on tracking devises or even using them for non-tracking solar absorbers. Note that, the spectral absorptance of both wavelengths shows small spikes at large incident angle under TE waves but not TM waves. This is due to the fact that for TM waves, the direction of magnetic field (i.e., y direction) is independent of incident angle, which is contrary to the case for TE waves. MP resonance strength becomes weaker under large incident angle for TM waves since electrical field that forms the resonance current loop becomes weaker; however, for TE waves the direction of magnetic field changes and thus instead of forming an electrical current loop in x-z plane, the loop is formed in x-y plane between the two neighboring nanowires.

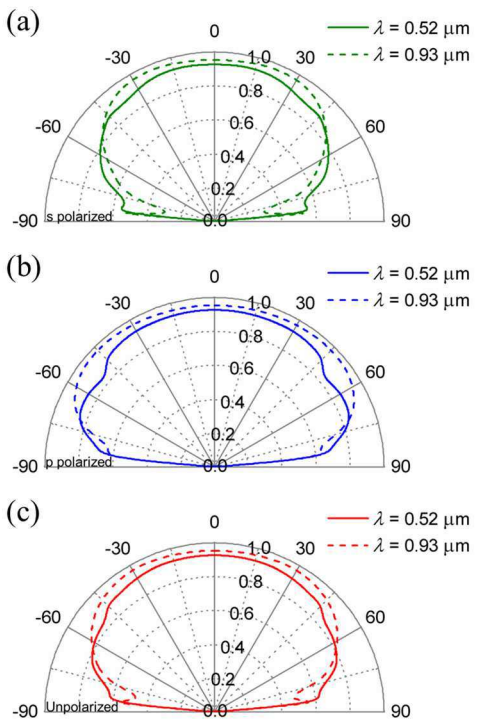

Fig. 2.6 The spectral absorptance at two resonance frequencies (MP2 and MP3) as a function of incident angle under (a) s-polarized, (b) p-polarized and (c) unpolarized waves.

Figure 2.6(c) reveals the spectral absorptance at MP2 and MP3 for unpolarized waves which indicates solar incidence. This further proves that the selective solar absorber has high spectral absorptance with low incident angle dependence at the resonance wavelengths of interest. Note that, the spectral absorptance is independent of wave polarization angle at normal incidence due to the geometric symmetry of nanowires as mentioned previously (i.e., 2-D periodic structure with same parameters).

2.3 Solar Thermal Efficiency Enhanced by Nanowire Metamaterials

After confirming the resonance effect, the conversion efficiency of the nanowire based selective absorber will then be presented. Here, since the main goal of this study is to verify the mechanism and show the potential of achieving selective absorptance by

nanowire structures, the performance analysis performed here will not be optimized with geometric parameters. That is, the performance analysis will only be carried out by the base geometry. The conversion efficiency is obtained through [7]:

$$\eta = \frac{\alpha_{\text{total}} CG - \varepsilon_{\text{total}} \sigma (T_{\text{A}}^4 - T_{\text{sky}}^4)}{CG} \tag{2.5}$$

where

$$\alpha_{total} = \frac{\int_{0.3\ \mu m}^{4\ \mu m} \alpha_{\lambda,N} I_{\text{AM1.5}}(\lambda) d\lambda}{\int_{0.3\ \mu m}^{4\ \mu m} I_{\text{AM1.5}}(\lambda) d\lambda} \tag{2.6}$$

and

$$\varepsilon_{total} = \frac{\int_{0.3\ \mu m}^{20\ \mu m} \varepsilon_{\lambda,N} I_{\text{BB}}(\lambda,\ T_{\text{A}}) d\lambda}{\int_{0.3\ \mu m}^{20\ \mu m} I_{\text{BB}}(\lambda,\ T_{\text{A}}) d\lambda} \tag{2.7}$$

Here, C is the concentration factor of sun light and the T_{A} is the absorber temperature. The constants sky temperature T_{sky} and incidence heat flux of solar irradiation G (AM1.5 is assumed) are kept to be 273 K and 1000 W/m^2, respectively. Figure 2.10(a) first shows the conversion efficiencies of four different absorbers with respect to different absorber temperature under one sun. The ideal absorber assumes unity absorptance and zero emittance with an optimal cutoff wavelength and the blackbody absorber assumes unity absorptance/emittance throughout the whole spectrum. The tungsten nanowire absorber is solid tungsten with the parameters of: P = 300 nm, H = 600 nm, and D = 150 nm. As shown in the figure, ideally the conversion efficiency can reach about 95%, but only the nanowire based absorber can reach ~80% efficiency at 100℃ while the two absorbers made of bare tungsten (~43.1%) and blackbody (~21.7%) are both far below that. However, as the absorber temperature rises, the efficiency of nanowire based absorber drops much faster than that of bare tungsten absorber. This is due to the fact that the nanowire absorber has a

broader absorption/emission band which extends to the near infrared. Although the efficiencies of the two absorbers are about the same when the absorber temperature reaches 350℃ and the nanowire based absorber performs even worse with further increasing temperature, this does not mean the absorber is only applicable for low temperature conditions. In fact, as shown in Fig. 2.10(b) while the absorber temperature is fixed at 400 ℃, the nanowire based absorber works much efficiently as long as the concentration factor is above 1.6. Note that, due to the unity absorptance throughout the whole spectrum, the efficiency of blackbody absorber increases rapidly under high concentration factor.

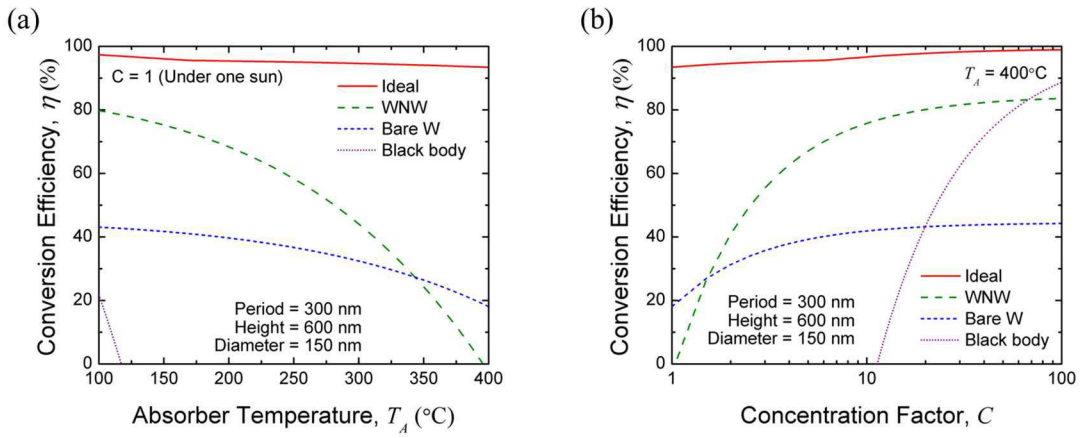

Fig. 2.7 The comparison of conversion efficiencies between ideal, nanowire based, bare tungsten, and blackbody absorbers with different (a) absorber temperature and (b) concentration factor.

CHAPTER 3 FUNDEMETAL UNDERSTANDING OF NEAR-FIELD RADIATIVE TRANSFER WITH NONMAGNETIC NANOWRIE/NANOHOLE METAMATERIALS

3.1 Theory of Near-Field Radiative Transfer between Nonmagnetic Uniaxial Media

Based on thermal stochastic nature of charges or dipoles in media [45], fluctuational electrodynamics can be applied to calculate the near-field radiative transport between objects at different temperatures. Recent work mainly focused on the near-field thermal radiation between isotropic thin films [46] or between semi-infinite uniaxial media [26]. However, since nanostructured periodic metamaterials usually supports tunable enhancement mechanisms and usually presents uniaxial properties, the theory of near-field radiation between two uniaxial thin films is required. Here, we extend theoretical framework from Francoeur et al. [47] on the near-field heat transfer between isotropic thin films to that between two uniaxial layers with finite thicknesses, by incorporating anisotropic wave optics. The net near-field heat flux between two uniaxial media with finite thicknesses at different temperatures (T_1 = 2000 K for the emitter and T_3 = 300 K for the receiver in this study) separated by a vacuum gap of d can be expressed as [29, 47, 48]:

$$q = \int_0^\infty q_\lambda d\lambda = \int_0^\infty q_\omega d\omega = \frac{1}{4\pi^2}\int_0^\infty d\omega\left[\Theta(\omega,T_1)-\Theta(\omega,T_3)\right]\int_0^\infty \xi(\omega,\beta)\beta d\beta \qquad (3.1)$$

where $\Theta(\omega,T)=\dfrac{\hbar\omega}{\exp(\hbar\omega/k_BT)-1}$ represents the spectral mean energy of a Planck oscillator at temperature T. $\hbar$ and k_B denote the reduced Planck constant and the Boltzmann constant, respectively. The energy transmission coefficient $\xi(\omega,\beta)$ has different expressions for propagating waves and evanescent waves as [47]:

$$\xi_{prop}(\omega,\beta)=\frac{\left(1-\left|R_1^s\right|^2-\left|T_1^s\right|^2\right)\left(1-\left|R_3^s\right|^2-\left|T_3^s\right|^2\right)}{\left|1-R_1^sR_3^se^{i2\gamma_2d}\right|^2}$$

$$+\frac{\left(1-\left|R_1^p\right|^2-\left|T_1^p\right|^2\right)\left(1-\left|R_3^p\right|^2-\left|T_3^p\right|^2\right)}{\left|1-R_1^pR_3^pe^{i2\gamma_2d}\right|^2} \tag{3.2a}$$

and $$\xi_{evan}(\omega,\beta)=\frac{4\,\mathrm{Im}(R_1^s)\,\mathrm{Im}\left(R_3^s\right)e^{-2\,\mathrm{Im}(\gamma_2)d}}{\left|1-R_1^sR_3^se^{i2\gamma_2d}\right|^2}+\frac{4\,\mathrm{Im}(R_1^p)\,\mathrm{Im}\left(R_3^p\right)e^{-2\,\mathrm{Im}(\gamma_2)d}}{\left|1-R_1^pR_3^pe^{i2\gamma_2d}\right|^2} \tag{3.2b}$$

where $$R_j^\alpha=\frac{r_{j-1,j}^\alpha+r_{j,j+1}^\alpha e^{i2\gamma_jt_j}}{1+r_{j-1,j}^\alpha r_{j,j+1}^\alpha e^{i2\gamma_jt_j}} \tag{3.3a}$$

and $$T_j^\alpha=\frac{t_{j-1,j}^\alpha t_{j,j+1}^\alpha e^{i\gamma_jt_j}}{1+r_{j-1,j}^\alpha r_{j,j+1}^\alpha e^{i2\gamma_jt_j}} \tag{3.3b}$$

Here, the subscript number j = 0, 1, 2, 3, or 4 is the layer index, which represents the vacuum substrate, emitter, vacuum gap, TPV receiver, and vacuum substrate, respectively. α = s or p denotes the polarization states. $r_{j-1,j}^s=(\gamma_{j-1}-\gamma_j)/(\gamma_{j-1}+\gamma_j)$ and $r_{j-1,j}^p=(\varepsilon_j\gamma_{j-1}-\gamma_j)/(\varepsilon_j\gamma_{j-1}+\gamma_j)$ are the Fresnel reflection coefficients for s and p polarizations at the interface of layers $j-1$ and j, respectively. γ_j is the z-component wavevector in an uniaxial layer j and can be expressed differently for s and p polarizations [13, 26]:

$$\gamma_j^{\,s}=\sqrt{\varepsilon_{j\|}\omega^2/c^2-\beta^2} \tag{3.4}$$

and $$\gamma_j^{\,p}=\sqrt{\varepsilon_{j\|}\omega^2/c^2-\frac{\varepsilon_{j\|}}{\varepsilon_{j\perp}}\beta^2} \tag{3.5}$$

where β is the parallel component of wavevector k_j, and is identical in different layers due to the continuity boundary condition at the interfaces. When the layer is isotropic, $\gamma_j^{\,p} = \gamma_j^{\,s}$ is held with $\varepsilon_{j\parallel} = \varepsilon_{j\perp}$.

Note that when the thicknesses of emitter and receiver become infinitely large, the structure reduces to a three-layer configuration with a half-space emitter (Layer 1), vacuum (Layer 2), and a half-space receiver (Layer 3). In this case, $\xi(\omega,\beta)$ in Eqs. (3.2) can be simplified through replacing the reflection coefficient of a thin film (R_j^{α}) by that at an interface ($r_{j,j-1}^{\alpha}$ or $r_{j,j+1}^{\alpha}$) and setting T_j^{α} = 0 [26]. In addition, the near-field radiative transfer in a four-layer thermal rectifier made of vacuum, a thin-film emitter, vacuum gap, and a half-space receiver has been investigated with a similar approach [24].

3.2 Graphene Assisted Surface Wave Coupling

In this section, we theoretically investigate the near-field radiative transfer between a nanostructured metamaterial emitter made of doped silicon nanohole (D-SiNH) arrays and a doped silicon plate covered by monolayer graphene, as depicted in Fig. 3.1(a). The emitter and receiver, which are separated by a vacuum gap with distance *d*, are respectively maintained at T_1 = 400 K and T_2 = 300 K with doping levels N_1 and N_2. The SiNH emitter is described as a uniaxial homogeneous medium by effective medium theory (EMT) and graphene modifies the reflection coefficients at the vacuum-receiver interface as a surface current. Fluctuational electrodynamics incorporated with uniaxial wave propagation is employed to calculate the near-field radiative heat flux. The enhancement in spectral near-field radiative transfer will be illustrated, while the underlying mechanism will be

elucidated as surface plasmon coupling between dissimilar materials with fluctuational electrodynamics and dispersion relation. The effects of graphene chemical potential and emitter doping level on the near-field energy transfer will be studied in detail as well.

The dielectric function of doped silicon used in this section can be obtained by a Drude model [49]:

$$\varepsilon_{\mathrm{Si}}\left(\omega, N, T\right) = \varepsilon_{\infty} - \frac{\omega_{\mathrm{p}}^2}{\omega^2 + i\Gamma\omega} \tag{3.6}$$

where ε_{∞} = 11.7 is the high-frequency constant, Γ is the temperature-dependent scattering rate, and $\omega_{\mathrm{p}} = \sqrt{N_{\mathrm{c}} e^2 / m^* \varepsilon_0}$ is the plasma frequency with carrier concentration N_{c}, electron charge e, carrier effective mass m^*, and the permittivity of free space ε_0. Here, the effect of doping level is accounted by carrier concentration which is the product of doping level and degree of ionization.

The dielectric function of graphene monolayer can be calculated by [50]:

$$\varepsilon_{\mathrm{GR}} = 1 + i\sigma / \omega\varepsilon_0\Delta \tag{3.7}$$

where Δ = 0.5 nm is the thickness of graphene, and the graphene conductivity $\sigma = \sigma_{\mathrm{I}} + \sigma_{\mathrm{D}}$ consists of interband and intraband (Drude) contributions [51, 52]:

$$\sigma_{\mathrm{I}}\left(\omega, \mu\right) = \frac{e^2}{4\hbar}\left[G\left(\frac{\hbar\omega}{2}\right) + i\frac{4\hbar\omega}{\pi}\int_0^{\infty} \frac{G\left(\xi\right) - G\left(\hbar\omega/2\right)}{\left(\hbar\omega\right)^2 - 4\xi^2} d\xi \right] \tag{3.8a}$$

and

$$\sigma_{\mathrm{D}}\left(\omega, \mu\right) = \frac{i}{\omega + i/\tau}\frac{2e^2 k_{\mathrm{B}} T}{\pi\hbar^2} \ln\left[2\cosh\left(\frac{\mu}{2k_{\mathrm{B}}T}\right)\right] \tag{3.8b}$$

where $\hbar$ is the reduced Planck constant, k_{B} is the Boltzmann constant, T is the absolute temperature, τ = 10^{-13} s is the relaxation time, μ is the chemical potential of

graphene, and $G(\xi)=\sinh(\xi/k_{\mathrm{B}}T)/\left[\cosh(\mu/k_{\mathrm{B}}T)+\cosh(\xi/k_{\mathrm{B}}T)\right]$.

The near-field radiative heat flux between two semi-infinite homogeneous media (when the equations are reduced to a 3-layer case) at temperatures of T_1 and T_2 ($T_1 > T_2$) can be calculated with fluctuational electrodynamics as illustrated in section 3.1. Since the contribution from propagating ($\beta < \omega/c$) and s-polarized waves are negligible when surface plasmon or phonon coupling exists [24, 29, 53], only the exchange function $s(\omega,\beta)$ for p-polarized evanescent ($\beta > \omega/c$) waves is considered here [29]:

$$s_{\mathrm{evan}}(\omega,\beta)=\frac{\mathrm{Im}(r_{01}^{p})\,\mathrm{Im}\left(r_{\mathrm{GR02}}^{p}\right)\beta e^{-2\mathrm{Im}(\gamma_0)d}}{\left|1-r_{01}^{p}r_{\mathrm{GR02}}^{p}e^{i2\gamma_0 d}\right|^{2}} \tag{3.9}$$

where r_{GR02}^{p} is the modified reflection coefficient for p-polarized waves at the vacuum-receiver interface by treating the graphene as a surface current, which is given by [50]:

$$r_{\mathrm{GR02}}^{p}=\frac{\omega\varepsilon_0(\varepsilon_2\gamma_0-\gamma_2)+\sigma\gamma_0\gamma_2}{\omega\varepsilon_0(\varepsilon_2\gamma_0+\gamma_2)+\sigma\gamma_0\gamma_2} \tag{3.10}$$

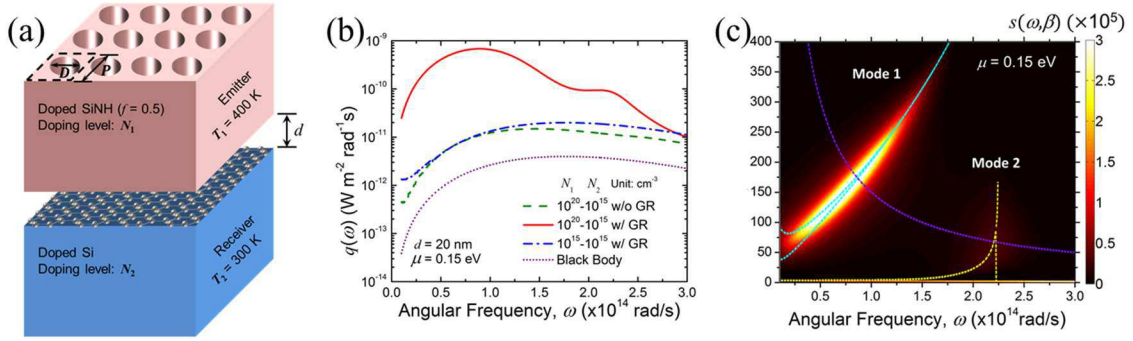

Fig. 3.1 (a) Schematic of the simulated structure separated by vacuum gap d where both the doped SiNH emitter and graphene covered D-Si receiver are assumed to be semi-infinite. (b) The spectral heat flux of four different setups: SiNH emitter (N_1 = 10^{20} cm^{-3}) with D-Si receiver (N_2 = 10^{15} cm^{-3}), SiNH emitter (N_1 = 10^{20} cm^{-3}) with graphene covered D-Si receiver (μ = 0.15 eV, N_2 = 10^{15} cm^{-3}), SiNH emitter (N_1 = 10^{15} cm^{-3}) with graphene

covered D-Si receiver ($\mu = 0.15$ eV, $N_2 = 10^{15}$ cm^{-3}), and two blackbodies as a function of angular frequency. (c) The exchange function between SiNH emitter ($N_1 = 10^{20}$ cm^{-3}) and graphene ($\mu = 0.15$ eV) covered D-Si receiver ($N_2 = 10^{15}$ cm^{-3}) separated by a vacuum gap of $d = 20$ nm. The $c/d\omega$ curve is shown by the purple dashed line.

In order to illustrate the near-field coupling effect between the D-SiNH emitter and the graphene-covered receiver, the spectral heat fluxes of three different cases are studied as shown in Fig. 3.1(b), where the Si plate receiver is lightly doped with $N_2 = 10^{15}$ cm^{-3} and the vacuum gap $d = 20$ nm for all three cases. Firstly, a heavily doped SiNH emitter with $N_1 = 10^{20}$ cm^{-3} and a bare Si plate receiver are considered, which results in the spectral heat flux on the order of 10^{-11} Wm^{-2}rad^{-1}s. Note that the maximum spectral radiative flux between two black bodies at the same temperatures of 400 K and 300 K is on the order of 10^{-12} Wm^{-2}rad^{-1}s as shown in Fig. 3.1(b). However, by simply coating the Si plate receiver with a monolayer graphene at a chemical potential $\mu = 0.15$ eV, the spectral heat flux is improved significantly with nearly two orders of magnitude enhancement. One major spectral peak with maximum $q_\omega = 6.8 \times 10^{-10}$ Wm^{-2}rad^{-1}s at the frequency of $\omega_1 = 0.9 \quad 10^{14}$ rad/s, while the other minor one with a peak value of $q_\omega = 9.4 \quad 10^{-11}$ Wm^{-2}rad^{-1}s at $\omega_2 = 2.1 \quad 10^{14}$ rad/s. The enhanced spectral enhancement leads to an improvement of 72 times in the total heat flux over the blackbody limit. In order to examine whether the extraordinary enhancement in spectral heat flux is solely due to the graphene layer on the plate receiver or caused by the mutual coupling between the emitter and receiver, the doping level of the SiNH emitter is then reduced to $N_1 = 10^{15}$ cm^{-3}, while the receiver is still covered by the graphene sheet. It turns out that, the spectral heat flux between the lightly doped SiNH emitter and graphene-covered plate receiver is significantly reduced

and becomes nearly the same as the first case with the heavily doped SiNH emitter and bare Si plate receiver without graphene. The two spectral peaks disappear as well. The comparison among all three cases clearly indicates that the extraordinary enhancement in near-field spectral heat flux is because of the coupling of the D-SiNH emitter and the graphene-covered receiver across the vacuum gap.

Figure 3.1(c) shows the exchange function $s(\omega,\beta)=\xi(\omega,\beta)\beta$ between the heavily-doped SiNH emitter (N_1 = 10^{20} cm^{-3}, f = 0.5) and the graphene-covered Si plate receiver (N_2 = 10^{15} cm^{-3}, μ = 0.15 eV) at the same vacuum gap of d = 20 nm. Note that the brighter contour indicates larger values of exchange function or stronger near-field energy transfer. One bright and broad enhancement band (mode 1) can be clearly seen at the low-frequency regime, which is responsible for the major q_ω peak around ω_1 = 0.9* 10^{14} rad/s observed in Fig. 3.1(b). The excitation of the resonance mode 1 requires large normalized parallel wavevector β^* = $\beta c/\omega$ from 50 to 400. In the meantime, another relatively weaker enhancement (mode 2) in the s(НО,Д) contour occurs around ω_2= 2.1* 10^{14} rad/s at smaller β^* values less than 200, which actually causes the minor spectral enhancement peak observed at higher frequencies. On the other hand, when the graphene is not present at the receiver surface or the emitter doping level becomes N_1 = 10^{15} cm^{-3}, i.e., the first and third cases considered in Fig. 3.1(b), both enhancement modes in the exchange function disappear in either case (though not shown here), suggesting that both enhancements in the $s(\omega, \beta)$ are the results of strong coupling between the emitter and receiver across the nanometer vacuum gap.

In order to understand the underlying coupling mechanism between the D-SiNH

emitter and the graphene-covered dielectric receiver, the dispersion relation of coupled SPPs across the vacuum gap can be analytically obtained by zeroing the denominator of the exchange function described in Eq. (3.9) as:

$$1 - r_{01}^{p} r_{\mathrm{GR}\,02}^{p} e^{i2\gamma_0 d} = 0 \tag{3.11}$$

The coupled SPP dispersion curves are then solved and plotted along with the contour in Fig. 3.1(c). Excellent agreement is observed between the $s(\omega,\beta)$ contour enhancement and the coupled SPP dispersion, clearly verifying that the enhanced energy transfer between the D-SiNH and the graphene is due to the coupled SPPs. Furthermore, the purple dashed line shown along with the dispersion curves indicates the line of $c/d\omega$. The crossing of the line and the two exchange function enhancement (or dispersion curves) matches the two resonance peaks on spectral heat flux shown in Fig. 3.1(b) which again prove the coupling effect of surface plasmons.Note that the optical properties of the D-SiNH would be significantly changed by the emitter doping level N_1 and filling ratio f, while those of the graphene-covered receiver would be largely altered by graphene chemical potential μ. Therefore, the Fresnel reflection coefficients r_{01}^{p} and $r_{\mathrm{GR}\,02}^{p}$ at both vacuum interfaces would change, leading to the possible shifts of coupled SPP modes and thereby the near-field radiative transfer.

Let us first investigate the effects of graphene chemical potential μ and emitter doping level N_1 on the respective single-interface SPP without coupling across vacuum gap. μ affects the SPP resonance mode at the vacuum-receiver interface while N_1 impacts SPP at the emitter-vacuum interface. Note that the emitter filling ratio f = 0.5 and receiver doping level $N_2 = 10^{15}$ cm^{-3} are kept unchanged. The SPP dispersion relation at the single

graphene-covered vacuum-receiver interface can be calculated by zeroing the Fresnel reflection coefficient $r^{p}_{\mathrm{GR}02}$:

$$\varepsilon_{2\|}\gamma_0 + \gamma_2 + \sigma\gamma_0\gamma_2 / \varepsilon_0\omega = 0 \tag{3.12}$$

Figure 3.2(a) shows how the single receiver interface SPP dispersion changes as a function of frequency ω and normalized parallel wavevector $\beta^* = \beta c/\omega$ when μ varies from 0 to 0.5 eV. Clearly, a larger graphene chemical potential will result in the SPP peak, where the two SPP modes merge, to shift towards higher frequencies. Note that higher β^* values indicate more channels of radiative energy transfer modes. The maximum $\beta^*_{\max}$ is 78 at ω = 0.7×1014 rad/s with μ = 0 eV, and further increases to 139 at ω = 2.28×1014 rad/s with μ = 0.1 eV. Within the frequency range of interests, the number of radiative transfer modes becomes less with further increase of μ.

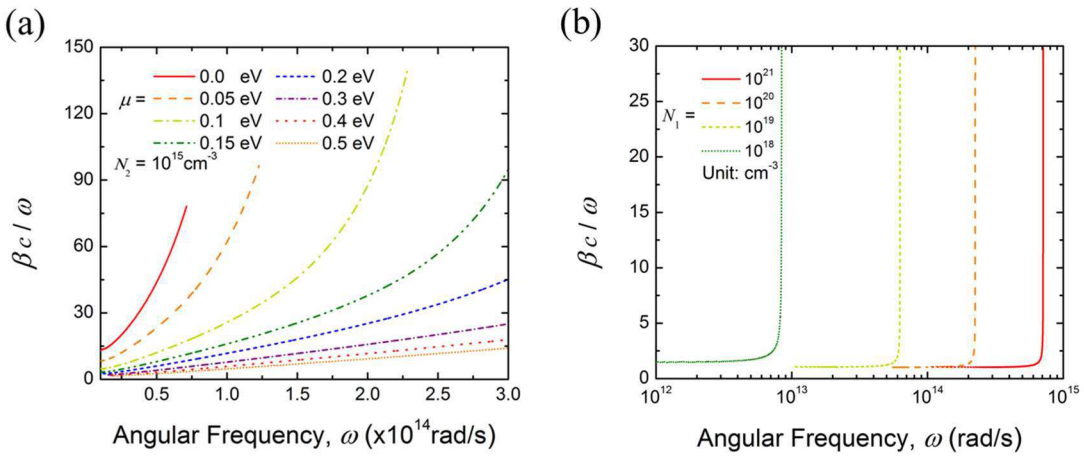

Fig. 3.2 The single interface SPP between (a) vacuum and graphene covered D-Si receiver (N_2 = 10^{15} cm^{-3}) with respect to different graphene chemical potential and (b) vacuum and SiNH of different doping level N_1.

On the other hand, the SPP dispersion at the single emitter-vacuum interface can be

obtained by solving $r_{01}^{p} = 0$ or equivalently

$$\varepsilon_{1\|}\gamma_0 + \gamma_1^{p} = 0 \tag{3.13}$$

As shown in Fig. 3.2(b), the single SPP at the SiNH interface shows strong dependence on the emitter doping level N1. Larger N1 values would result in the SPP mode to shift towards higher frequencies. For a given doping level, the SPP dispersion shows little selectivity on angular frequencies with small β^* values less than 2, suggesting few radiative transfer modes. The number of near-field energy transfer channels significantly increases as seen via the abrupt increase of β^* values when it approaches the asymptotic frequency, e.g., ω_{asy} = 2.1×10^{14} rad/s for N_1 = 10^{20} cm^{-3}. In general, the asymptotic frequency can be obtained under the condition of $\mathrm{Re}\left(\varepsilon_{\perp}\varepsilon_{\|}\right)=1$, which can be analytically derived from Eq. (12) with $\beta^* \gg 1$.

Now let us study the effects of P and N_1 on the near-field SPP coupling. Figures 3.3(a) and 3.3(b) present the exchange functions between the D-SiNH emitter (N_1 = 10^{20} cm^{-3}) and graphene-covered receiver across a 20-nm vacuum gap at different graphene chemical potentials of P = 0.3 and 0.5 eV, respectively. In comparison with the exchange function at P = 0.15 eV shown in Fig. 3.1(c), it can be clearly seen that, larger P values cause the shift of the enhancement mode 1 in $s(\omega,\beta)$ towards higher frequencies. Although β^* values becomes smaller, the strength of the exchange function actually increases with larger μ. The μ effect on the coupled SPP shifting is consistent with that on the single-interface SPP shown in Fig. 3.2(a). On the other hand, the enhancement mode 2 barely changes by the P. The behaviors of both SPP coupling modes 1 and 2 at different P are further verified by the excellent agreement between the coupled SPP dispersion and the

enhancement in exchange function. The SPP dispersion curves enhancement mode 2 also indicates an asymptotic frequency of 2.1×10^{14} rad/s, which matches well with that of the SPP at the single emitter-vacuum interface with $N_1 = 10^{20}$ cm^{-3} as indicated in Fig. 3.2(b).

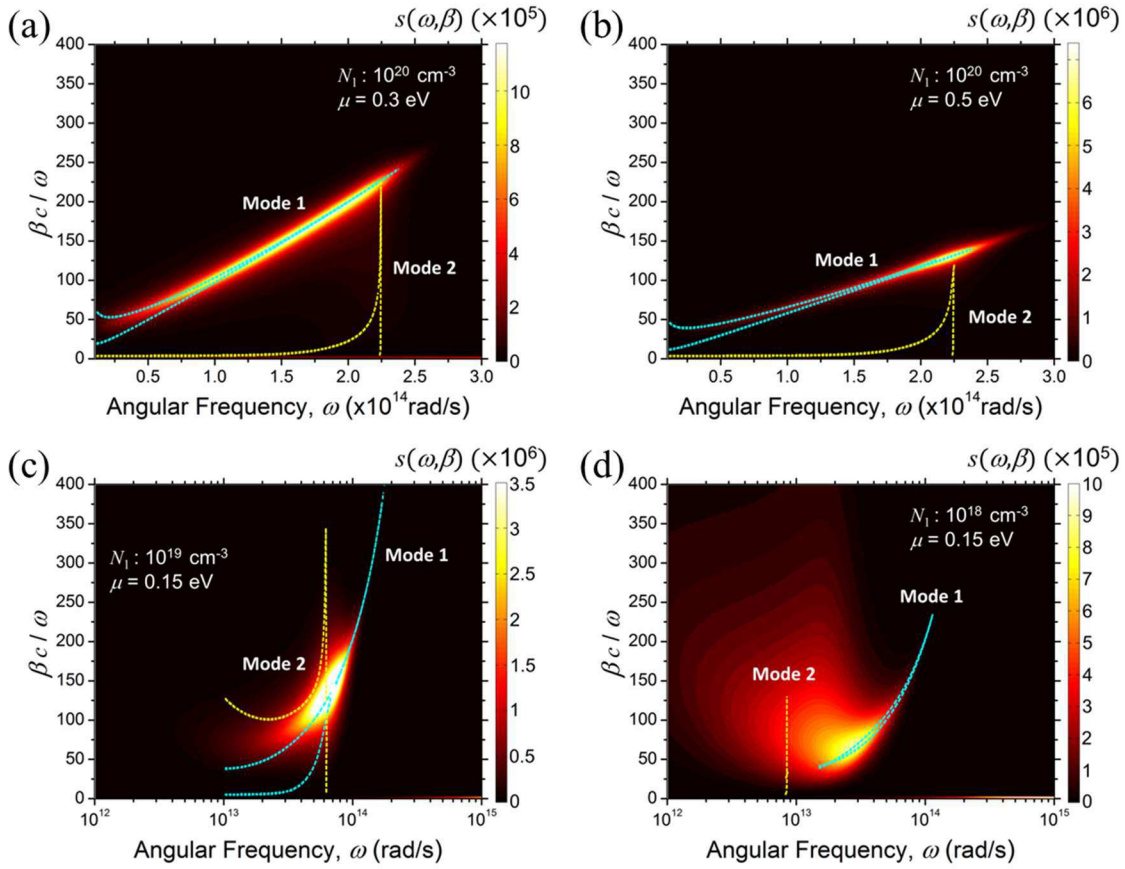

Fig. 3.3 The exchange function between SiNH emitter ($N_1 = 10^{20}$ cm^{-3}) and graphene covered D-Si receiver ($N_2 = 10^{15}$ cm^{-3}) with graphene chemical potential (a) 0.3 eV and (b) 0.5 eV; and that between SiNH emitter and graphene ($\mu = 0.15$ eV) covered D-Si receiver ($N_2 = 10^{15}$ cm^{-3}) with emitter doping level of (c) 10^{19} cm^{-3} and (d) 10^{18} cm^{-3}. The vacuum gap d is 20 nm.

On the other hand, when reducing the N_1 values to 10^{19} cm^{-3} and 10^{18} cm^{-3} as shown respectively in Figs. 3.3(c) and 3.3(d), the enhancement in exchange function changes significantly. As learned from the single-interface SPP behavior, the asymptotic frequency

of the SPP at the emitter interface would shift toward lower frequencies when N_1 decreases, resulting in the coupled SPPs associated with the enhancement mode 2 to be pushed towards lower frequencies and couple with the enhancement mode 1 region. As a result, with $N_1 = 10^{19}$ cm^{-3} the four coupled modes which occurs within the same frequency region strongly interact with each other, leading to a merged and much stronger enhancement in the exchange function contour. When N_1 further decreases to 10^{18} cm^{-3}, the enhancement mode 2 shifts to even lower frequencies than the enhancement mode 1, as seen by the coupled SPP dispersion curves, resulting in a much broader enhancement in $s(\omega,\beta)$. Note that, the enhancement mode 1 region due to the coupled SPP little shifts with N_1. Clearly, the emitter doping level N_1 or the surface plasmon at the emitter-vacuum interface dominates the enhancement mode 2 on $s(\omega,\beta)$ contour, while graphene chemical potential μ or the surface plasmon at the vacuum-graphene interface plays a significant role only in the enhancement mode 1 due to SPP coupling. By manipulating the N_1 and μ values, all the coupled SPP modes could interact with each other at different strengths, which could significantly change the exchange function and thereby modulate the near-field radiative transfer.

In order to quantitatively demonstrate the near-field coupling effect on the energy transfer, a near-field enhancement factor is defined as $\Xi = q / q_{BB}$, where q is the total near-field radiative flux between the D-SiNH emitter and graphene-covered planar receiver integrated over frequency range from 1* 10^{13} rad/s to 3* 10^{14} rad/s, and $q_{BB} = 992$ W/m^2 is the radiative flux between two black bodies at temperatures of 400 K and 300 K respectively. Figure 3.4(a) shows the near-field enhancement factor as a function of chemical potential μ from 0 to 1 eV at different emitter doping levels N_1 from 10^{15} to 10^{21}

cm^{-3}. The receiver doping level N_2 is 10^{15} cm^{-3} and the vacuum gap is d = 20 nm. Firstly of all, when N_1 = 10^{20} cm^{-3}, the enhancement factor is only about 55 at P = 0 eV, starts to increase at P = 0.1 eV, reaches about 370 at P = 0.6 eV, and then saturates with larger P values. The P effect on the near-field radiative flux enhancement can be clearly understood by the exchange functions in Figs. 3.3(a) and 3.3(b), where the two enhancement regions of different SPP modes couple with each other. As a result of stronger coupling, the exchange function and thereby the radiative flux become larger. Note that, after the two modes are coupled together, further increment of chemical potential will only result in saturation of heat flux. The P effect on the near-field radiative flux is similar with more doping at N_1 = 10^{21} cm^{-3}, while only 40 times enhancement is achieved over the blackbody limit. This is because the asymptotic frequency of the SPP at the emitter interface is at γ 10^{14} rad/s shown in Fig. 3.2(b), which is much higher than the resonance frequencies of the major coupled SPP modes (i.e., mode 1) dominated by the receiver interface. Therefore, the coupling strengths of the two modes at large P is much weaker compared to that with N_1= 10^{20} cm^{-3}.

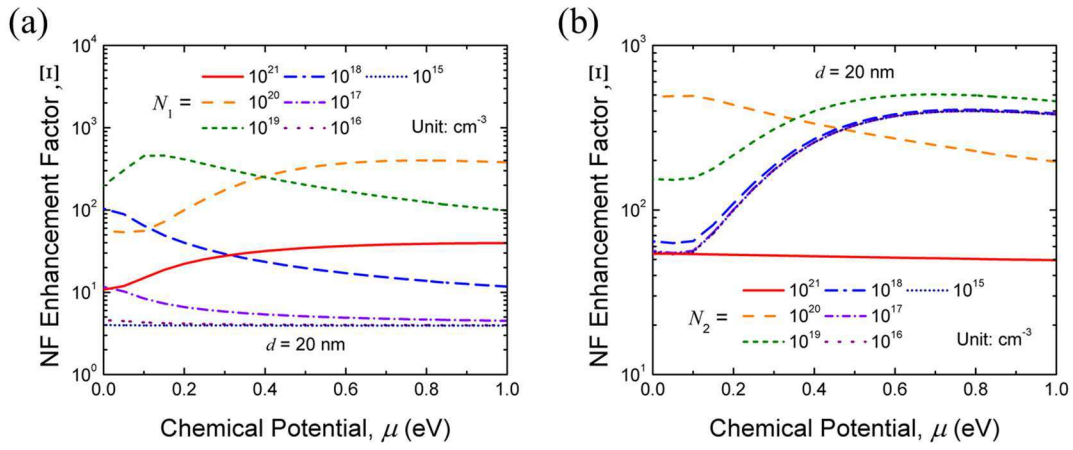

Fig. 3.4 The near-field enhancement factor Ξ as a function of graphene chemical potential with respect to different (a) emitter doping level N_1 while the receiver has a doping level of $N_2 = 10^{15}$ cm^{-3} and (b) receiver doping level N_2 while the emitter has a doping level of $N_1 = 10^{20}$ cm^{-3}. The gap distance is set to be $d = 20$ nm.

Interestingly, the P effect on the enhancement factor is different for N_1 ↑ 10^{19} cm^{-3}. There occurs a maximum enhancement at N_1 ≈ 10^{19} cm^{-3} and $\mu = 0.15$ eV, which is about 460 times higher than the heat flux between two blackbodies, while the enhancement becomes smaller at either smaller or larger P. This is actually not surprising after the exchange function in Fig. 3.3(c) is understood, where strongest coupling between the two modes occurs. Different P values will shift the enhancement mode 1 which is dominated by the receiver interface to different frequencies that are away from the asymptotic frequency of the SPP at the emitter interface, leading to weaker SPP coupling and thus smaller near-field radiative heat flux. On the other hand, when N_1 is further decreased, the asymptotic frequency would shift towards lower frequencies less than ≈ 10^{13} rad/s indicated by Fig. 3.2(b). As a consequence, the surface plasmon at the emitter interface cannot couple efficiently with the other graphene-dominated interface, whose SPP occurs at higher frequencies. Thus, it is understandable that the enhancement factor for $N_1 = 10^{18}$ and 10^{17} cm^{-3} is high only at $P = 0$ eV, and then monotonically decreases with larger P values, which actually shifts the enhancement mode 1 towards higher frequencies further away from the enhancement mode 2 at low frequencies. For lightly doped SiNH emitter with N_1 ↑ 10^{16} cm^{-3}, the surface plasmon at two interfaces cannot couple at all across the nanometer vacuum gap, resulting in the lowest radiative flux, and the graphene chemical potential could barely take into any effect.

It should be noted that, besides N_1 and P, the receiver doping level N_2, which changes the reflection coefficient $r_{\mathrm{GR}02}^{p}$ at the vacuum-graphene-D-Si plate interface, could potentially affect the near-field energy transfer as well. Figure 3.4(b) presents the near-field enhancement factor as a function of P at different N_2 values with the emitter doping level N_1 is fixed at 10^{20} cm^{-3} and d = 20 nm. After low doping levels from 10^{15} to 10^{18} cm^{-3}, N_2 does have little effect on the normalized radiative heat flux. On the other hand, the enhancement factor Ξ first does not change with P, then starts to monotonically increase at P = 0.1 eV, and finally saturates at 400 for P > 0.5 eV. Basically at low doping level N_2, which has almost no effect on tuning the surface plasmon at the graphene-covered interface, graphene chemical potential dominates and the near-field coupling between the two modes becomes stronger with larger P as explained previously. N_2 starts to play a role in further enhancing the radiative flux up to about 500 times over the blackbody limit when it increases to 10^{19} cm^{-3}, at which the P effect is similar with that at less doping in the silicon plate.

However, when N_2 further increases to 10^{20} cm^{-3}, enhancement factors around 500 is achieved with small P values less than 0.1 eV, and starts to monotonically decrease when P becomes larger. The different trend of the P effect can be understood by the effect of N_2 on tuning the surface plasmon of doped silicon plates. As studied in Ref. [54], higher doping level increases the charge density of doped silicon and pushes the plasmon frequency towards higher frequencies into the infrared region under investigation. In other words, larger doping level N_2 could shift the coupled SPP mode 1 toward higher frequencies but have no effect on the emitter-dominated mode 2, as demonstrated by the dispersion curves in Fig. 3.5(a) in comparison with Fig. 3.1(c). Therefore, even at small P

like 0.1 eV in this case, both coupled SPP modes could already occurs at nearby frequencies, and strong coupling and merging could occur. When further increasing the P, the coupled enhancement mode 1 shifts to higher frequencies, resulting in decreased coupling strength between the two modes, as demonstrated by Fig. 3.5(b) with P= 0.5 eV, and thereby smaller radiative flux. If the silicon plate receiver is heavily doped with $N_2 = 10^{21}$ cm^{-3}, the coupled mode 1 will occur at higher frequencies than the coupled mode 2 even at $\mu = 0$, in which case the coupling between the two modes are already weak. Larger Pvalues, which pushes the mode 1 towards even higher frequencies, will not strengthen but keep weakening the coupling of two modes, leading to much smaller near-field enhancement factor around 50 times with little μ effect, as can clearly be seen in Fig. 3.4(b).

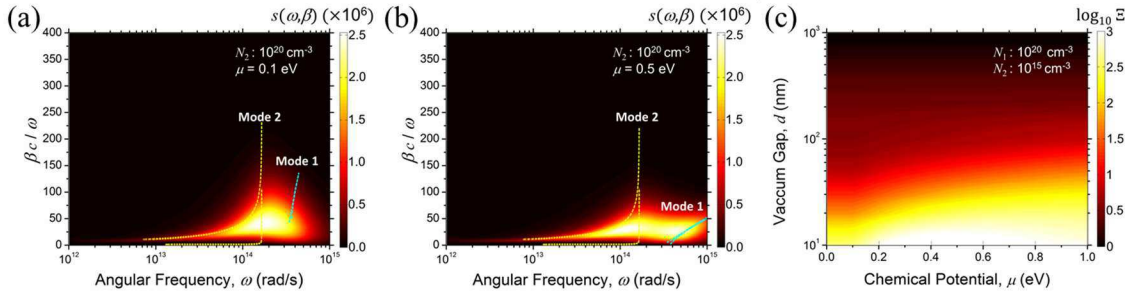

Fig. 3.5 The exchange function between SiNH emitter (N_1 = 10^{20} cm^{-3}) and graphene covered D-Si receiver ($N_2 = 10^{20}$ cm^{-3}) with graphene chemical potential of (a) 0.1 eV and (b) 0.5 eV while the gap distance is set to be d = 20 nm. (c) The impact of vacuum gap distance d and graphene chemical potential μ on near-field enhancement factor Ξ under the emitter doping level $N_1 = 10^{20}$ cm^{-3} and receiver doping level $N_2 = 10^{15}$ cm^{-3}.

Finally, the effect of vacuum gap on the near-field energy transfer is investigated. Figure 3.5(c) shows the near-field enhancement factor Ξ at different vacuum gap distance d from 10 nm up to 1 μm with varying graphene chemical potential P from 0 eV to 1 eV. The doping levels for the SiNH emitter and the silicon plate receiver are $N_1 = 10^{20}$ cm^{-3} and

$N_2 = 10^{15}$ cm^{-3}, respectively. Overall, the near-field radiative transfer decreases with larger vacuum gap, which is understandable as the coupled SPP modes becomes weaker when the emitter and receiver further apart. When $d > 500$ nm the near-field enhancement factor approaches one, in other words, the radiative transfer goes to the far-field limit. As a matter of fact, the graphene dominated resonant mode 1 disappears when gap distance is larger than 200 nm, while the SiNH dominated resonant mode 2 vanishes when $d > 70$ nm, both of which are confirmed by exchange function plots (not shown here). The near-field radiative transfer is greatly enhanced at $d < 70$ nm, where both resonant modes exist and could further couple with each other. More than two orders of magnitude enhancement over the blackbody limit can be achieved at vacuum gaps less than 40 nm, in which case larger graphene chemical potentials greatly promotes the enhanced near-field energy transfer. Note that, cautions need to be paid at sub-20-nm vacuum gaps as the effective medium approximation for the SiNH emitter may no longer be valid depending on the comparison of the pattern size such as period P to the vacuum gap d, as EMT is generally valid for near-field radiative transfer only when $P < \pi d$.

3.3 Hyperbolic Modes between Nanowire Arrays

In this section, we investigate the application of Indium-Tin-Oxide (ITO) nanowires as hyperbolic metamaterials for near-field thermal radiation. Let us consider near-field radiative heat transfer between ITO nanowire arrays (ITONWAs) separated by vacuum gap of d as shown in Fig. 3.6. One of the nanowire arrays or the emitter is at temperature T_1 while the receiver is at temperature T_2. The two arrays are separated by a vacuum gap and are assumed to be in local thermal equilibrium. The wires are long enough for both the emitter

and receiver to be considered semi-infinite. As a symmetric case, the filling ratio f is assumed to be the same for both nanowire arrays. In previous studies, the nanowire arrays with large filling ratios can be considered as a homogenous medium with anisotropic optical properties by applying effective medium theory (EMT) [26]. However, since the spatial dispersion effect should not be excluded for nanowire structures with small filling ratios [55, 56], the effective medium theory considering spatial dispersion is applied here to describe the uniaxial optical properties of nanowire arrays [57, 58].

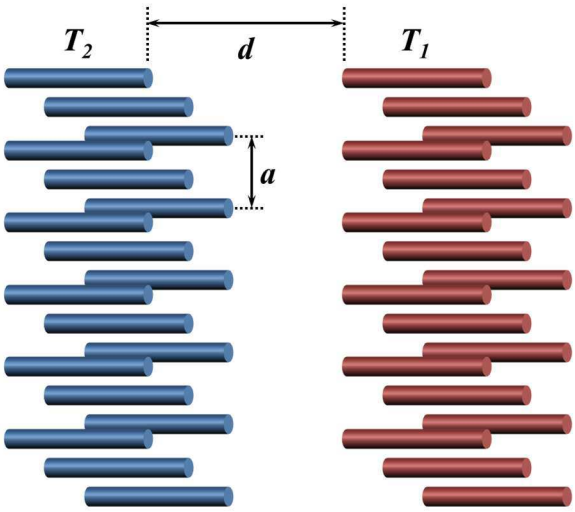

Fig. 3.6 Schematic of near-field radiation between ITONW arrays at different temperatures separated by a vacuum gap d.

The spatial dispersion dependent EMT is used to treat the ITONW as homogenous layers since it accurately predicts optical properties for highly conductive nanorods with filling ratios less than 0.5 [57, 58]. As part of the formulation for the ITONWA, air is considered as the host medium and the ITO nanowires are taken as spatially separated embedded grains. For ordinary waves in which the electric field is perpendicular to the axis of nanowires, the effective dielectric function $\varepsilon_{O,eff}$ is given as

$$\varepsilon_{\mathrm{O,eff}} = 1 + \frac{2}{\frac{1}{f}\frac{\varepsilon_{\mathrm{ITO}}+1}{\varepsilon_{\mathrm{ITO}}-1}-1} \tag{3.8}$$

Note that, this equation yields the same equation for ordinary waves given by Maxwell-Garnett EMT [40] since the effect of spatial dispersion applies only for extraordinary waves. On the other hand for extraordinary waves where the electric field is parallel to the axis of the nanowires, the effective dielectric function $\varepsilon_{\mathrm{E,eff}}$ is given by

$$\varepsilon_{\mathrm{E,eff}} = 1 + \frac{1}{\frac{1}{(\varepsilon_{\mathrm{ITO}}-1)f} - \left(\frac{c\beta}{\omega_{\mathrm{p}}}\right)^2} \tag{3.9}$$

where c is the speed of light in vacuum, β is the wave vector component normal to the wire direction, and ω_{p} is 3.362* 10^{15} rad/s which is the plasmon frequency of ITO [59]. Note that, since the effect of spatial dispersion is considered, the extraordinary dielectric function is not only a function of angular frequency ω like ordinary dielectric function. It is a function of wave vector component β as well. In the above equations, the dielectric function of ITO, $\varepsilon_{\mathrm{ITO}}$, is given by Drude model

$$\varepsilon_{\mathrm{ITO}} = \varepsilon_{\infty} - \frac{\omega_{\mathrm{p}}^2}{\omega^2 + i\omega\Gamma} \tag{3.10}$$

The values of ε_{∞} and Γ are 3.8 and 1.68* 10^{14} rad/s [59], respectively. The metallic nature of ITO results in a very small penetration depth for thermal radiation and therefore ITONWs can be considered as semi-infinite in this study.

Figures 3.7(a) and 3.7(b) are contour plots of $\xi(\omega,\beta)$ for p-polarized waves as a function of ω and β for different filling ratios during near-field radiative heat transfer

between two nanowire arrays separated by a 20 nm vacuum gap. The temperature of the emitter is set to 1500K while the receiver is set to 0 K. The enhancement of ITONW can be identified through looking into the property of ITONW. For f = 0.1, depending on the normalized β, ITONW behaves as type 1 HMM and effective dielectric at lower and higher frequency, respectively. Thus, the broad band enhancement in transmission coefficient at lower frequency is due to HMM behavior and the small enhancement around 1.5×10^{15} rad/s is due to ENP (epsilon-near-pole). For f = 0.5, the broad band enhancement at lower frequency is also caused by type 1 HMM, but the region of type 1 HMM shifts to higher frequency with increasing filling ratio. The strengthened enhancement around 1.5×10^{15} rad/s is in fact due to type 2 HMM which only occurs within a narrow band. Interestingly, the two enhancement bands form a single broadband enhancement region instead of two separate enhancement modes since the range of type 1 and type 2 HMM are right next to each other. This can be beneficial for some applications which requires continuous broadband enhancement in the field of energy conversion. In addition, the spectral location of ENP overlaps with that of type 2 HMM with f = 0.5, and therefore can't clearly be observed here since the enhancement strength of type 2 HMM mode is much stronger than that of ENP with p-polarized waves. Note that, since HMM behavior occurs under all filling ratios, the strong near infrared resonance for ITONWAs irrespective of the filling ratio make them suitable candidates as emitter for near-field thermophotovoltaic devices.

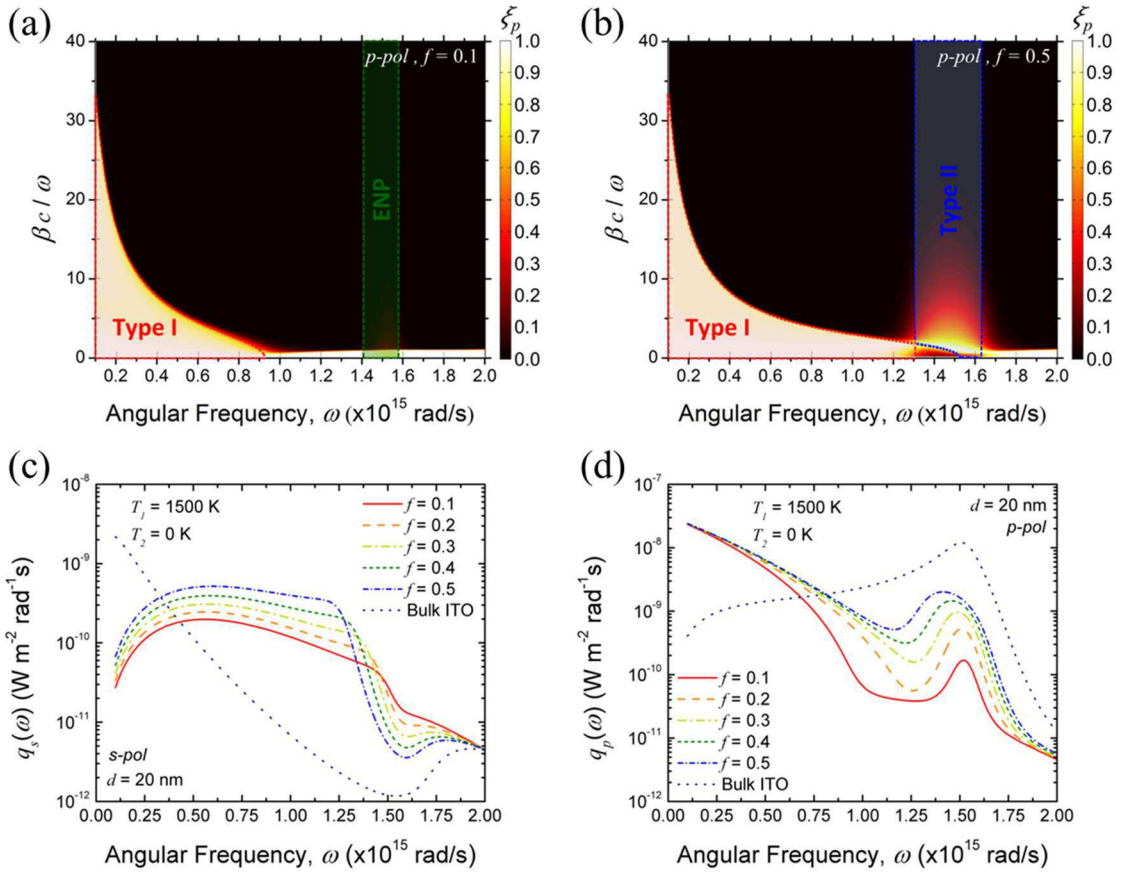

Fig. 3.7 Contour plots of ξ for different filling ratios: (a) 0.1, (b) 0.5; and spectral heat fluxes of (c) s-polarized and (d) p-polarized waves between ITONW arrays at different symmetric filling ratios separated by 20 nm gap.

The spectral heat fluxes between two ITONWAs of s and p polarized waves are shown in Figs. 8(c) and 6(d), respectively, for 20 nm vacuum gap. The spectral heat flux can be calculated by Eq. (3.1) without integrating over ω. For convenience, the spectral heat flux between two semi-infinite bulk ITOs is also plotted in the figures along with different filling ratios for ITONWs. As shown in Fig. 3.7(c), there is no enhancement between semi-infinite bulk ITOs on s-polarized waves at high frequency while the enhancement of ENP can clearly be seen for ITONWs. The shifting and strengthening of

ENP enhancement agrees with the material property (not shown here). On the other hand, for p-polarized waves as presented in Fig. 3.7(d), there is one enhancement peak which corresponds to the excitation of SPP for semi-infinite ITO [59]. For ITO nanowires, the peaks in spectral heat flux matches very well with the results from Figs. 3.4(a) and 3.4(b). In fact, both the shifting of type 1 HMM mode and the broadening and strengthening of type 2 HMM mode can be observed with increasing filling ratio which the drop of spectral heat flux between two HMM modes is also flattened. Note that, at this gap distance, the enhancement due to coupled SPP between two bulk ITOs is still stronger than that due to type 2 HMM and ENP.

Figure 3.8 plots the total near-field heat transfer as a function of the vacuum gap separating the ITONWs for different filling ratios. The expression for the total heat transfer is given in Eq. (3.1). The heat transfer for NWs is normalized with respect to that between two bulk ITOs. The main enhancement between two bulk ITOs is due to coupled SPP whose strength increases as the vacuum gap decreases. Therefore, at very small gap distance such as 10 nm, the heat flux between two ITONWAs is less than that between two bulk ITOs. However, with increasing vacuum gap to around 150 nm, the gap distance effect on HMM modes is less than that on the coupling strength of SPP since HMM modes are due to the material property. Therefore, the heat flux between ITONWAs becomes nearly 11 times higher than that between bulk ITOs at 150 nm vacuum gap. Although further increment of gap distance will result in less enhancement due to the fast weakening of type 2 enhancement mode (will be shown later by Fig. 7), the normalized heat flux still reaches about 7 at $d = 1$ μm. While Fig. 4 indicated that the near-field heat transfer at 20 nm should increase as the filling ratio increases, Fig. 5 shows the same behavior only when d is less

than 150 nm. Beyond 150 nm, the trend changed and the total heat transfer is maximum for $f = 0.3$ and minimum for $f = 0.1$. This is also due to the fast weakening of type 2 enhancement mode which will result in the drop of overall heat flux on $f = 0.4$ and 0.5 where type 2 HMM enhancement is stronger. Figure 5 therefore shows the effect of vacuum gap on both HMM behavior (ITONWAs for different filling ratios) and SPP resonance (bulk ITOs). Interestingly, the total heat transfer at 150 nm between ITONWAs with 0.5 filling ratio is more than one order of magnitude greater than that between semi-infinite ITO. On the other hand, for doped Si even for $f = 0.5$, the heat transfer is only 2.5 times higher than that of bulk media at 150 nm [26]. ITONWs therefore provide a definite advantage in terms of enhancement in total heat transfer and cost over as compared to doped semiconductors such as Si.

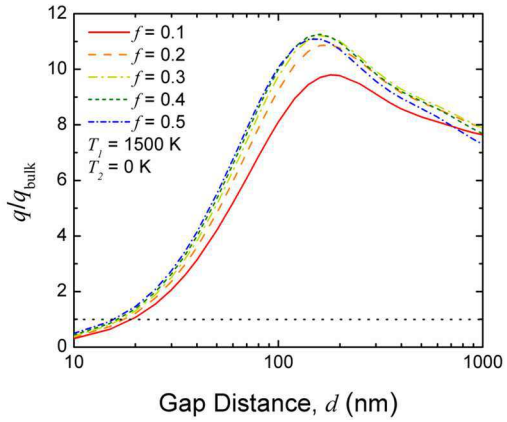

Fig. 3.8 Total heat flux between the ITONW arrays as a function of vacuum gap for different filling ratios. The heat flux is normalized with respect to that between two bulk ITOs.

CHAPTER 4 SYSTEMATIC ANALYSIS OF NANOWIRE BASED NEAR-FIELD THERMOPHOTOVOLTAIC SYSTEMS

This chapter studies the effect of a HMM emitter made of a tungsten nanowire array embedded in alumina (Al_2O_3) on the near-field TPV energy conversion. The influence of the volumetric filling ratio of the HMM emitter on near-field radiative transfer will be thoroughly investigated on the radiative transport, power generation and the conversion efficiency. Possible enhancement on the near-field radiation due to the ENP and hyperbolic modes of the HMM emitter will be explored. Moreover, the effect of a thin-film TPV cell with finite thicknesses will be studied aiming to further improve the conversion efficiency. Finally, the thickness effects of both a thin film TPV cell and a HMM emitter with vacuum substrate on both power output and conversion efficiency will be explored to optimize the cell performance.

4.1 Nanowire Based Thermophotovoltaic Emitter

Figure 4.1 shows the configuration of the near-field TPV system to be investigated, which consists of a HMM emitter (Layer 1) made of tungsten nanowire arrays embedded in the Al_2O_3 host, and a TPV receiver (Layer 3) made of $In_{0.2}Ga_{0.8}Sb$ [60] separated by a vacuum gap (Layer 2) with distance d. The HMM emitter and the TPV receiver are both considered to be semi-infinite in this section. The volumetric filling ratio of the nanowire array is $f = \pi D^2/(4a^2)$, where a is the period and D is the nanowire diameter, respectively. Here, the materials for the HMM emitter are chosen not only because of the high-temperature stability but also due to the possibility of fabrication for further experimental demonstration. The Al_2O_3 nanohole array can be first fabricated in large areas by anodic

aluminum oxide (AAO) with pore diameters down to 15 nm [61]. Tungsten nanowires can be then grown in the nanoholes by different electrodepositing methods depends on the geometric features [62]. Note that, though AAOs generally have hexagonal unit cells, while square ones can also be fabricated by pre-imprinting the aluminum [63].

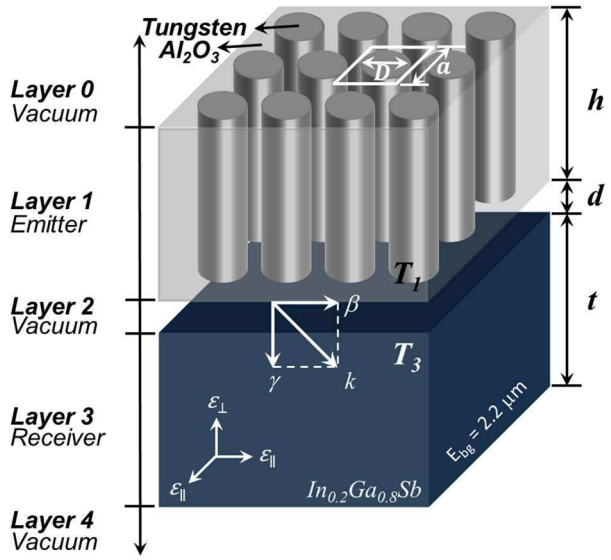

Fig. 4.1 Schematic of a near-field TPV system consisting of a tungsten nanowire based HMM emitter and a TPV cell with finite thicknesses in a 5-layer structure: vacuum substrate, emitter, vacuum gap, receiver, vacuum substrate.

Figure 4.2(a) shows the transmission coefficient $\xi(\omega,\beta)$ at s polarization with filling ratio $f = 0.5$ when the vacuum gap is fixed at $d = 20$ nm. By comparison, the transmission coefficients in the shaded region are enhanced with more channels of heat transfer (i.e., $\beta c/\omega$) within a narrow frequency band, which can be explained by the stronger ENP mode at the same frequency region (not shown here). Note that, only the parallel component of dielectric function of the HMM emitter $\varepsilon_{\parallel,\mathrm{eff}}$ is involved with s-polarized waves. When the filling ratio increases, higher absorption loss (or emission) takes place at the ENP mode for

$\varepsilon_{\parallel,\text{eff}}$, and results in larger radiative transfer or transmission coefficients from the emitter to the receiver. Figure 4.2(b) presents the transmission coefficient $\xi(\omega,\beta)$ at p polarization with f = 0.5. The shaded region with large transmission coefficient at low frequency matches well with the type I HMM region of the material property (not shown here). Therefore, the enhancement in $\xi(\omega,\beta)$ at low-frequency region is due to the HMM behavior of the tungsten nanowire emitter. The enhancement at higher frequencies is due to the effective dielectric behavior of the nanowire emitter, in which the absorption loss becomes greater with larger imaginary parts of both $\varepsilon_{\parallel,\text{eff}}$ and $\varepsilon_{\perp,\text{eff}}$.

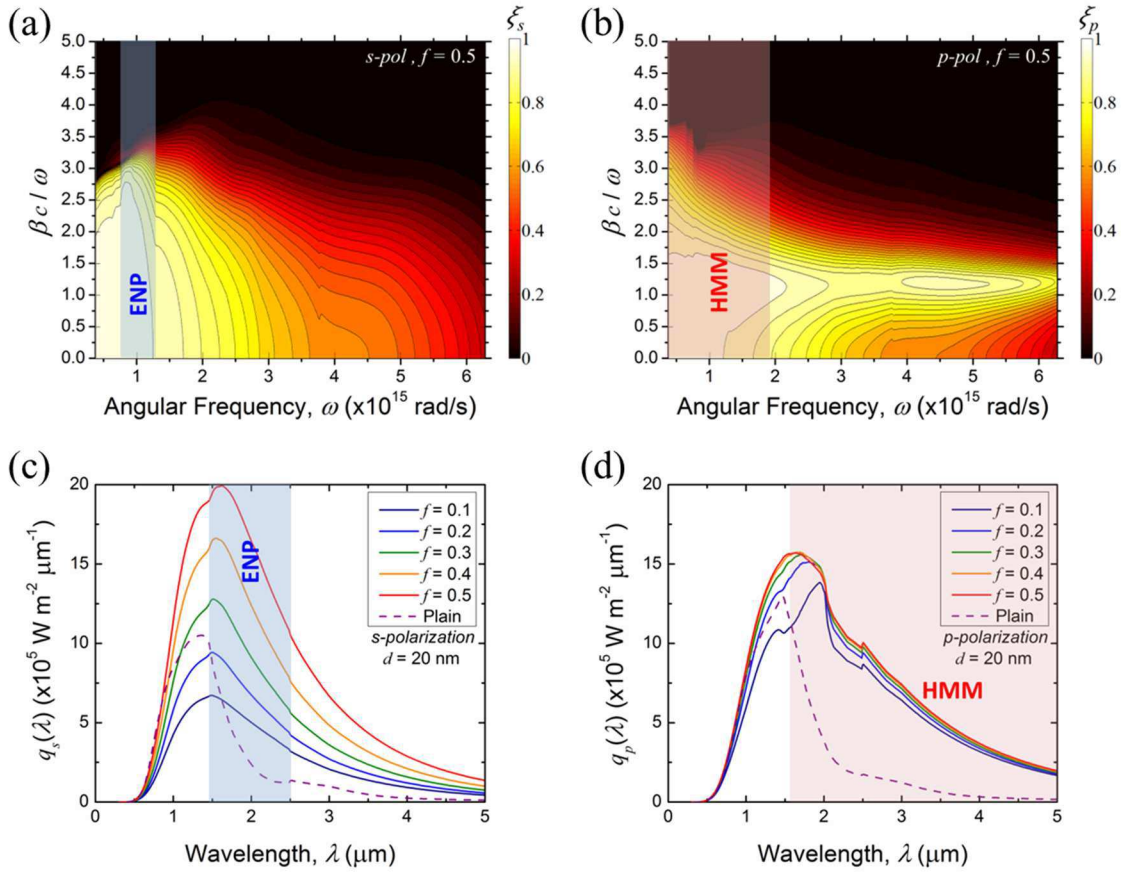

Fig. 4.2 The ξ function of a 3-layer near-field TPV device with the nanowire HMM emitter of 0.5 filling ratios for (a) s polarization and (b) p polarization. The spectral heat fluxes of the same device for (c) s polarization and (d) p polarization.

According to Eq. (3.1), the enhancement of transmission coefficients will result in the enhancement of spectral heat flux. Figures 4.2(c) and 4.2(d) show the spectral heat fluxes between the semi-infinite nanowire HMM emitter and semi-infinite TPV cell for s and p polarizations, respectively. At s polarization, a steady enhancement on the spectral heat flux appears with the increment of filling ratio. Furthermore, due to the narrow-band ENP enhancement on transmission coefficient $\xi(\omega,\beta)$ demonstrated by Fig. 4.2(a), an enhancement within the ENP region also takes place with larger filling ratios. Note that, even though the spectral heat flux for s polarization rises with f from 0.1 to 0.5, it does not necessarily indicate that the spectral heat flux for plain tungsten emitter (i.e., $f = 1$) will become larger than that with nanowire emitters, which in fact is lower than that of nanowires with filling ratio $f > 0.3$. This can be explained by the effective material property of nanowire emitters is not similar to plain tungsten for high filling ratios up to $f = 0.5$. Plain tungsten has negative real part of dielectric function at angular frequency $\omega < 2\times10^{15}$ rad/s, which indicates metallic behavior. On the other hand, tungsten nanowires possess positive real part of $\varepsilon_{\|,\mathrm{eff}}$ in the same frequency region, and behave as lossy dielectrics. As a result, the spectral heat flux from the nanowire emitters is higher than that from plain tungsten at longer wavelengths, as shown in Fig. 4.2(a). Note that, the spectral peak with plain tungsten at 1.4 μm is due to its intrinsic bandgap absorption.

As shown in Fig. 4.2(b) for p polarization, the spectral heat flux distribution with the HMM emitters exceeds that with plain tungsten at wavelengths $\lambda > 1.6$ μm or so for all filling ratios. The enhanced spectral heat flux region matches well with the type I HMM region. The spectral peak also shifts slightly towards lower wavelengths with larger filling ratios, which is due to the shifting of HMM mode region for p polarization at different f values. Therefore, the enhanced spectral flux with HMM emitters at longer wavelengths is due to the hyperbolic behavior in tungsten nanowires, which do not exist in plain tungsten. Among different filling ratios, the difference in spectral heat flux is not as apparent as that for s polarization. Furthermore, the spectral heat flux drops abruptly at the wavelength $\lambda \approx 2$ μm for all filling ratios, which does not appear for s polarization. The abrupt reduction in $q(\lambda)$ at p polarization can be explained by the sudden drop of the real part of $\varepsilon_{\perp,\text{eff}}$, or equivalently by the sharp increase of the imaginary part of $\varepsilon_{\perp,\text{eff}}$.

Photons with spectral energy above the cell bandgap, i.e., E_g = 0.56 eV (or equivalently 2.2 μm in wavelength) for $In_{0.2}Ga_{0.8}Sb$, will be absorbed by the TPV cell to generate electron-hole pairs. Electrical currents could be produced with external loads after the photon-generated charges are collected. However, the photons with lower energy cannot excite electron hole pairs and result in low conversion efficiency. The near-field radiative transfer and the charge transport inside the TPV cell is a coupled problem, which has been theoretically modeled for multilayer isotropic media by calculating the charge density distribution due to the number of photons absorbed at different cell location [22]. In fact, the quantum efficiency in response to the near-field thermal radiation is different from that to a far-field source because of the inherent difference between near-field and

far-field thermal radiation spectra. The small penetration depth of evanescent waves, especially at resonance modes, significantly affects the photon absorption at different depths away from the cell surface, which would lead to modified quantum efficiency at different frequencies in the near-field. However, due to the limitation of the present theoretical model, which cannot predict the spectral energy absorbed at different depths by treating the TPV cell as a multilayer, the quantum efficiency to the near-field thermal radiation between the uniaxial HMM emitter and the TPV cell cannot be thus obtained accurately. Instead of assuming a perfect TPV cell with 100% quantum efficiency, which will over predict the performance, we use the far-field internal quantum efficiency of $In_{0.2}Ga_{0.8}Sb$ [60] for evaluating the proposed near-field TPV system with a nanowire-based HMM emitter, aiming for more practical insights. We also neglected the thermal impact on the overall TPV performance by simply assuming the nanowire emitter and TPV at respective thermal equilibrium with uniform temperature distribution. For the sake of completeness, the methods for calculating the power generation and conversion efficiency are summarized here.

With the near-field spectral heat flux $q_\lambda(\lambda)$ calculated from Eq. (3.1) and the far-field internal quantum efficiency data $\eta_{\mathrm{q}}(\lambda)$, the short-circuit current can be obtained as [22]:

$$J_{\mathrm{ph}} = \frac{e}{hc}\int_0^\infty \eta_{\mathrm{q}}(\lambda) q_\lambda(\lambda)\lambda d\lambda \tag{4.1}$$

The dark current can be calculated by [22]:

$$J_0 = e\left(\frac{n_{in}^2 D_{\mathrm{h}}}{N_D\sqrt{\tau_{\mathrm{h}}}} + \frac{n_{in}^2 D_{\mathrm{e}}}{N_A\sqrt{\tau_{\mathrm{e}}}}\right) \tag{4.2}$$

Here, h is the Planck constant, n_{in} is the intrinsic carrier concentration, N_D, and N_A are the carrier concentration of donor and acceptor, respectively. D_h, D_e, τ_h and τ_e are the diffusion coefficient and relaxation time of holes and electrons, respectively. Moreover, the open-circuit voltage is given by:

$$V_{oc} = \left(k_B T / e\right) \ln(J_{ph} / J_0 + 1) \tag{4.3}$$

Therefore, the electrical power output can be expressed as [22]:

$$P_{El} = J_{ph} V_{oc} (1 - 1/y)[1 - \ln(y)/y] \tag{4.4}$$

where

$$y = \ln(J_{ph} / J_0) \tag{4.5}$$

Finally, by dividing the electrical power output with the total radiative power input, the conversion efficiency of the proposed near-field TPV system with a HMM emitter is [22]:

$$\eta = P_{El} / P_R \tag{4.6}$$

Figure 4.3(a) shows the normalized radiative power input and electrical power output of the TPV cell with HMM emitters at different filling ratios over that with plain tungsten at the vacuum gap d = 20 nm. Note that, the radiative heat flux and power generation with a plain tungsten emitter are 2.51 MW/m^2 and 0.58 MW/m^2 respectively, leading to a conversion efficiency of 23.1%. By replacing the plain tungsten emitter with tungsten nanowire HMMs, the electrical power output increases with larger filling ratios, and exceeds that with plain tungsten under all filling ratios. The enhancement in power output could reach about 2.15 times higher with f = 0.5. On the other hand, the total radiative heat flux from the emitters to the TPV cell is also amplified with nanowire HMMs, and increases with filling ratio. This is because the HMM emitter enhances the spectral energy not only above but also below the bandgap at longer wavelengths as the broadband

enhancement shown in Figs. 4.2(c) and 10(d). As a result, the conversion efficiency with nanowire HMM emitters is between 16.1% and 17.7% with different filling ratios, which is about 5.4% to 7% less compared with that (23.1%) from a plain tungsten emitter as shown in Fig. 4.3(b), though the electrical power output is enhanced more than 2 times.

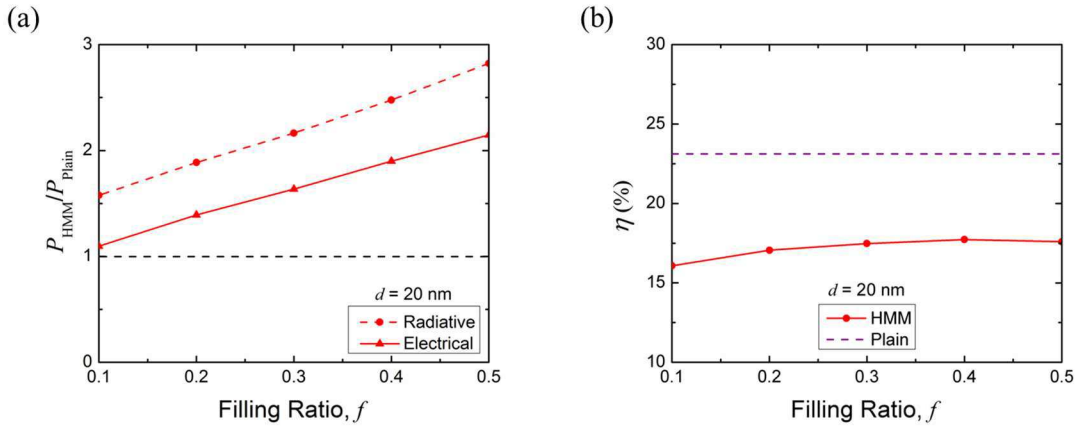

Fig. 4.3 (a) The electrical power output and the radiative power input of a 3-layer near-field TPV system with the nanowire HMM emitter (f = 0.5) normalized to those with plain tungsten emitter. (b) The conversion efficiency of a 3-layer near-field TPV system with the nanowire HMM emitter (f = 0.5) and a plain tungsten emitter. The vacuum gap distance is d = 20 nm.

The electrical power output and the TPV conversion efficiency are calculated at different vacuum gap distances for the nanowire HMM emitter with f = 0.5, as shown in Figs. 4.4(a) and 4.4(b), respectively. The power generation decreases monotonically when the HMM emitter and the TPV cell are further apart, due to the reduction of near-field radiative heat transfer. However, the conversion efficiency with the HMM emitter drops first from 19.1% to a minimum of 9.4% when the vacuum gap becomes larger from d = 10 nm to 400 nm or so, and then rises up to 15.3% at a 1-μm vacuum gap. The plain tungsten exhibits similar behaviors in both power output and conversion efficiency but with smaller P_{El} and a larger efficiency η by 4% or so. The different dependence on the vacuum gap

between the electrical power and conversion efficiency can be understood by the effect of vacuum gap on the spectral radiative heat flux, as only that above the cell bandgap would enhance the conversion efficiency. When the gap distance is smaller than 400 nm, small gap distances contribute more on the enhancement of heat flux above the bandgap rather than the waste energy. This can be confirmed by Fig. 4.4(a) that the power output increases rapidly with the reduction of gap distance when d is less than 400 nm. On the other hand, the heat flux enhancement due to small vacuum gap focused more on longer wavelengths (i.e., energy below the band gap) with gap distances larger than 400 nm as the electrical power input remains constant and the conversion efficiency drops. In order to make the nanowire HMM emitter more useful in enhancing the near-field TPV conversion efficiency over the plain tungsten, approaches other than reducing gap distance such as considering the TPV emitter and cell as thin films need to be further explored.

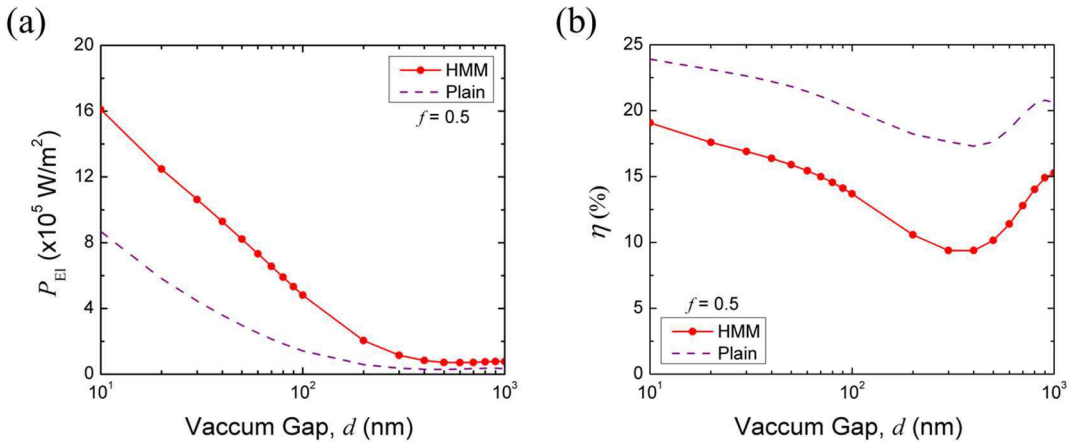

Fig. 4.4 The vacuum gap effect on: (a) power output; (b) conversion efficiency of a 3-layer near-field TPV system with the nanowire HMM emitter (f = 0.5) and a plain tungsten emitter.

4.2 Effects of Thin-Film Emitter and Thermophotovoltaic Cell

The key to enhance the TPV conversion efficiency is to reduce the spectral radiative energy below the bandgap that is not useful to generate electron-hole pairs in the cell [64]. Here, the semi-infinite TPV cell is first replaced by a free-standing thin layer with thickness t = 10 μm, while the nanowire HMM emitter is kept semi-infinite, forming a 4-layer near-field TPV system. The filling ratio of the HMM emitter is chosen to be the same as f = 0.5 for comparison with the previous results from the semi-infinite TPV cell.

Figure 4.5(a) shows the spectral radiative heat flux from the 4-layer TPV system with a cell thickness of t = 10 μm. It can clearly be observed that the spectral heat flux at wavelengths smaller than the cell bandgap is almost the same with that from a semi-infinite cell with relative difference less than 1%, indicating that the spectral radiative energy above the cell bandgap is totally absorbed within the 10-μm thick TPV cell. However, the spectral radiative energy below the bandgap is reduced to almost zero at longer wavelengths, which is actually due to the total internal reflection occurring at the bottom interface between the TPV cell and vacuum substrate (i.e., layer 3 and 4) because the electromagnetic waves are incident from a dense medium (i.e., TPV cell) with a larger refractive index into vacuum. In fact, only the waves with spectral energy below the bandgap could reach the bottom cell interface, while the energy associated with the evanescent waves will be reflected back since the total internal reflection occurs at $\beta c/\omega > 1$. The significantly reduced long-wavelength radiative energy absorbed by the TPV cell due to the total internal reflection could greatly enhance the TPV conversion efficiency.

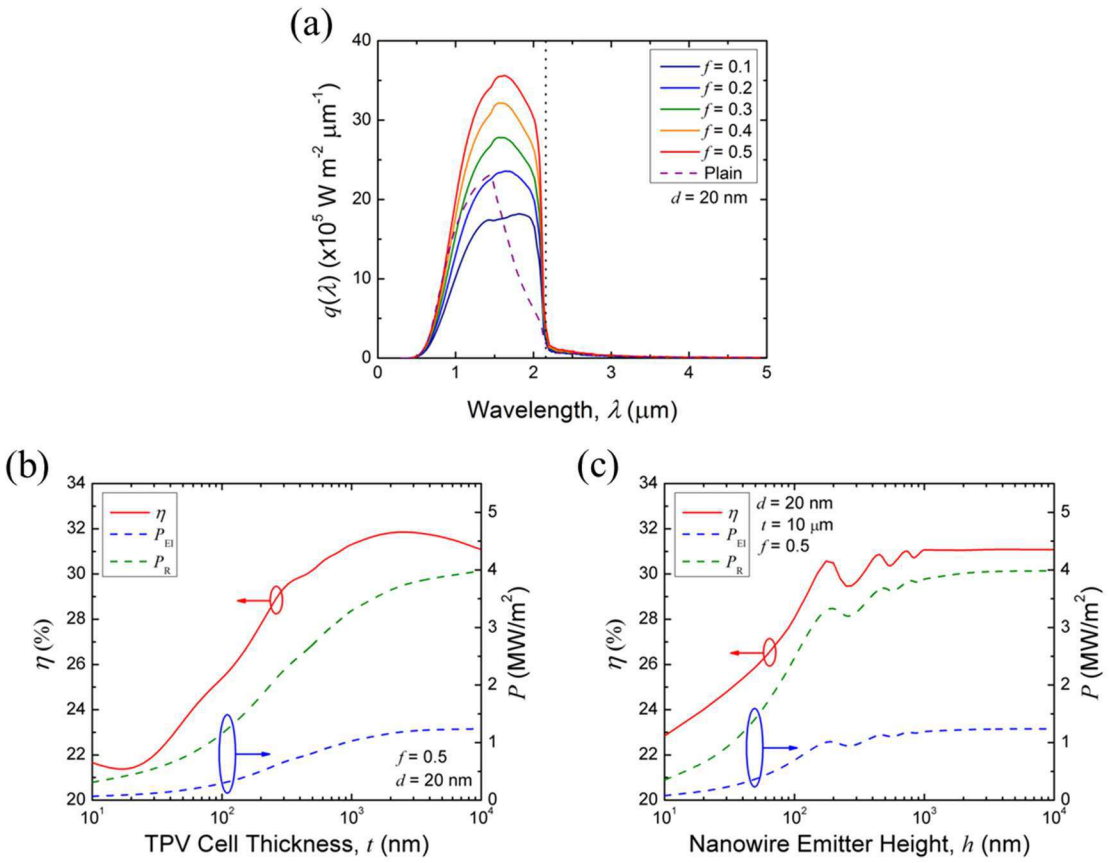

Fig. 4.5 (a) The spectral heat flux of a 4-layer near-field TPV system made of a semi-infinite nanowire HMM emitter with different filling ratios and a free-standing thin TPV cell with thickness t = 10 μm separated by a vacuum gap d = 20 nm. Conversion efficiency, radiative power, the electrical power density of a 5-layer near-field TPV system made of a thin nanowire HMM emitter and a thin TPV cell, both of which are on vacuum substrates as a function of (b) the cell thickness t with nanowire height h = 10 μm or (c) nanowire height h with cell thickness t = 10 μm. The filling ratio of the nanowire emitter is f = 0.5, while the vacuum gap is d = 20 nm.

Now, the HMM emitter and the TPV receiver are assumed to have a finite thickness h and t, respectively, and vacuum is assumed to be the substrates (Layer 0 and Layer 4). As the improved near-field TPV performance was demonstrated with a thin TPV cell of 10 μm in thickness, we now aim to gain a quantitative understanding in the cell thickness

effect on the TPV conversion efficiency and the power generation, which is shown in Fig. 4.5(b). The parameters such as vacuum gap d = 20 nm and emitter filling ratio f = 0.5 are kept the same. As the TPV cell thickness decreases from t = 10 μm, the power output drops monotonically. However, the conversion efficiency slightly rises up to a maximum of 31.8% around t = 3 μm. Within this thickness range, the TPV cell is still thick enough to absorb most of the spectral energy above the cell bandgap but absorbs less spectral energy below the bandgap due to smaller cell thickness (or less material). As a result, the conversion efficiency is slightly increased. When the TPV cell thickness t is further reduced to 10 nm, the conversion efficiency drops dramatically down to ~22%, which is apparently because the cell is not thick enough to absorb all the spectral energy above the bandgap. Therefore, the thickness effect indicates that, the TPV cell should be chosen to be thicker than 2 μm to achieve the optimal conversion efficiency.

It should be noted that the present conversion analysis on the cell thickness effect does not consider the influences from the electrical losses due to charge recombination and from the thermal losses due to non-uniform temperature distribution inside the TPV cell. In practice, different cell thickness would affect the charge transport as well as the thermal transport. In order to rigorously model both electrical and thermal losses, the spectral energy absorbed at different cell depth has to be calculated [22, 65]. However, because of the uniaxial nature of the nanowire emitter, the rigorous calculation requires a near-field radiative transfer model incorporated with multilayer uniaxial wave optics, which is yet to be developed. Therefore, the present study considers the TPV cell (i.e., $In_{0.2}Ga_{0.8}Sb$) with quantum efficiency from the far-field response and neglects the thickness effect on the

electrical and thermal losses, aiming to only focus on near-field radiative transfer with the nanowire HMM emitter in terms of the near-field TPV performance.

Finally, the thickness effect of the tungsten nanowire emitter on the near-field TPV performance is considered by treating the nanowire array with a finite height h on vacuum substrate, forming a 5-layer near-field TPV system with a thin TPV cell with thickness t = 10 μm. As shown in Fig. 4.5(c), the radiative and electrical power and the resulting conversion efficiency do not change much when the nanowire emitter thickness h reduces from 10 μm to 1 μm, suggesting that 1-μm-long nanowires are thick enough to be opaque. When further reducing the nanowire height down to 200 nm or so, oscillation occurs in both the radiative and electrical power plots as a function of emitter thickness h, due to the wave interference inside the thin-film emitter as the thermal wavelength is comparable with the nanowire thickness. As a result, the conversion efficiency also oscillates with a 1% fluctuation but does not change much. However, when the tungsten nanowire height is further reduced to be $h < 200$ nm, the radiative power drops dramatically with a much faster rate than the electricity power generation. This can be explained by the less emitting materials as the ENP and the HMM behavior are responsible for the near-field radiative heat transfer enhancement, both of which are simply associated with the effective material properties of the tungsten nanowire arrays. Therefore, the TPV conversion efficiency decreases significantly from 30.5% at h = 200 nm to 23% with a thin nanowire array of 10 nm in thickness.

CHAPTER 5 ARTIFICIAL "MAGNETIC" METAMATERIALS FOR NEAR-FIELD RADIATIVE TRANSFER

This chapter focuses on the theoretical analysis of near-field radiative heat transfer between two semi-infinite dual uniaxial electromagnetic metamaterials. The near-field radiative heat transfer is calculated by fluctuational electrodynamics incorporated with anisotropic wave optics by taking into account the electromagnetic responses to both s and p polarized waves.

5.1 Derivations for Dual Uniaxial Electromagnetic Metamaterials

5.1.1 Derivation of Fresnel reflection and transmission coefficients between two arbitrary dual uniaxial electromagnetic media

In order to account the magnetic response of metamaterials, permeability needs to be considered in the calculation and therefore the reflection coefficient and the wavevector z-component both need to be modified.For s-polarized waves, the permittivity and permeability tensors of an arbitrary dual uniaxial electromagnetic medium *i* can be defined as:

$$\hat{\varepsilon}_i = \begin{bmatrix} \varepsilon_{i\parallel} & 0 & 0 \\ 0 & \varepsilon_{i\parallel} & 0 \\ 0 & 0 & \varepsilon_{i\perp} \end{bmatrix} \text{ and } \hat{\mu}_i = \begin{bmatrix} \mu_{i\parallel} & 0 & 0 \\ 0 & \mu_{i\parallel} & 0 \\ 0 & 0 & \mu_{i\perp} \end{bmatrix} \tag{5.1}$$

Here, ﺝ and ﺽdenote the direction parallel (in x-y plane) and perpendicular (z direction) to the interface, respectively. The nonzero components of the electric and magnetic fields for s-polarized waves are [2]:

$$E_y = \begin{cases} \left(E_I e^{i\gamma_i^s z} + E_R e^{-i\gamma_i^s z}\right) e^{i\beta x} & for \;\; z < 0 \\ E_T e^{-i\gamma_j^s z} e^{i\beta x} & for \;\; z > 0 \end{cases} \tag{5.2}$$

and

$$H_x = \begin{cases} -\dfrac{\gamma_i^s}{\omega\mu_0\mu_{i\|}}\left(E_I e^{i\gamma_i^s z} - E_R e^{-i\gamma_i^s z}\right) e^{i\beta x} & for \;\; z < 0 \\ \dfrac{\gamma_j^s}{\omega\mu_0\mu_{j\|}} E_T e^{i\gamma_j^s z} e^{i\beta x} & for \;\; z > 0 \end{cases} \tag{5.3}$$

Since both E_y and H_x should be continuous at the boundary $z = 0$, Eq. (5.2) and Eq. (5.3) yield:

$$\left(E_I + E_R\right) e^{i\beta x} = E_T e^{i\beta x} \tag{5.4}$$

and

$$-\frac{\gamma_i^s}{\omega\mu_0\mu_{i\|}}\left(E_I - E_R\right) e^{i\beta x} = \frac{\gamma_j^s}{\omega\mu_0\mu_{j\|}} E_T e^{i\beta x} \tag{5.5}$$

Therefore, with the definition of Fresnel reflection and transmission coefficients for s-polarized waves where $r_{ij}^s = E_R / E_I$ and $t_{ij}^s = E_T / E_I$, the expression of the two coefficients can then be derived from Eq. (5.4) and Eq. (5.5):

$$r_{ij}^s = \frac{\mu_{j\|}\gamma_i^s - \mu_{i\|}\gamma_j^s}{\mu_{j\|}\gamma_i^s + \mu_{i\|}\gamma_j^s} \tag{5.6}$$

and

$$t_{ij}^s = \frac{2\mu_{j\|}\gamma_i^s}{\mu_{j\|}\gamma_i^s + \mu_i\gamma_j^s} \tag{5.7}$$

For p-polarized waves, similar to the process of s-polarized, the nonzero components of the electric and magnetic fields for p-polarized waves are [2]:

$$E_x = \begin{cases} -\dfrac{\gamma_i^p}{\omega\varepsilon_0\varepsilon_{i\|}}\left(H_I e^{i\gamma_i^p z} - H_R e^{-i\gamma_i^p z}\right)e^{i\beta x} & for\ \ z<0 \\ \dfrac{\gamma_j^p}{\omega\varepsilon_0\varepsilon_{j\|}} H_T e^{i\gamma_j^p z} e^{i\beta x} & for\ \ z>0 \end{cases} \tag{5.8}$$

and

$$H_y = \begin{cases} \left(H_I e^{i\gamma_i^p z} + H_R e^{-i\gamma_i^p z}\right)e^{i\beta x} & for\ \ z<0 \\ H_T e^{-i\gamma_j^p z} e^{i\beta x} & for\ \ z>0 \end{cases} \tag{5.9}$$

Since both E_x and H_y should be continuous at the boundary $z = 0$, Eq. (5.8) and Eq. (5.9) yield:

$$-\frac{\gamma_i^p}{\omega\varepsilon_0\varepsilon_{i\|}}\left(H_I - H_R\right)e^{i\beta x} = \frac{\gamma_j^p}{\omega\varepsilon_0\varepsilon_{j\|}} H_T e^{i\beta x} \tag{5.10}$$

and

$$\left(H_I + H_R\right)e^{i\beta x} = H_T e^{i\beta x} \tag{5.11}$$

Therefore, with the definition of Fresnel reflection and transmission coefficients for p-polarized waves where $r_{ij}^p = H_R / H_I$ and $t_{ij}^p = H_T / H_I$, the expression of the two coefficients can then be derived from Eq. (5.10) and Eq. (5.11):

$$r_{ij}^p = \frac{\varepsilon_{j\|}\gamma_i^p - \varepsilon_{i\|}\gamma_j^p}{\varepsilon_{j\|}\gamma_i^p + \varepsilon_{i\|}\gamma_j^p} \tag{5.12}$$

and

$$t_{ij}^p = \frac{2\varepsilon_{j\|}\gamma_i^p}{\varepsilon_{j\|}\gamma_i^p + \varepsilon_i\gamma_j^p} \tag{5.13}$$

The Fresnel reflection and transmission coefficients at the interface between vacuum and a dual uniaxial electromagnetic medium can now be obtained. Let's assume medium 0 is vacuum and medium 2 is a dual uniaxial electromagnetic medium, Eq. (5.6) and Eq. (5.7) can be simplified by $\mu_{0\|} = \mu_{0\perp} = \mu_0 = 1$ and $\gamma_0^s = \gamma_0$ for s-polarized waves:

$$r_{02}^{s}=\frac{\mu_{2\|}\gamma_0-\mu_0\gamma_2^{s}}{\mu_{2\|}\gamma_0+\mu_0\gamma_2^{s}}=\frac{\mu_{2\|}\gamma_0-\gamma_2^{s}}{\mu_{2\|}\gamma_0+\gamma_2^{s}} \tag{5.14}$$

and

$$t_{02}^{s}=\frac{2\mu_{2\|}\gamma_0}{\mu_{2\|}\gamma_0^{s}+\mu_0\gamma_2^{s}}=\frac{2\mu_{2\|}\gamma_0}{\mu_{2\|}\gamma_0^{s}+\gamma_2^{s}} \tag{5.15}$$

For p-polarized waves where $\varepsilon_{0\|}=\varepsilon_{0\perp}=\varepsilon_0=1$ and $\gamma_0^{p}=\gamma_0$, Eq. (5.12) and Eq. (5.13) yield:

$$r_{02}^{p}=\frac{\varepsilon_{2\|}\gamma_0-\varepsilon_0\gamma_2^{p}}{\varepsilon_{2\|}\gamma_0+\varepsilon_0\gamma_2^{p}}=\frac{\varepsilon_{2\|}\gamma_0-\gamma_2^{p}}{\varepsilon_{2\|}\gamma_0+\gamma_2^{p}} \tag{5.16}$$

and

$$t_{02}^{p}=\frac{2\varepsilon_{2\|}\gamma_0}{\varepsilon_{2\|}\gamma_0+\varepsilon_0\gamma_2^{p}}=\frac{2\varepsilon_{2\|}\gamma_0}{\varepsilon_{2\|}\gamma_0+\gamma_2^{p}} \tag{5.17}$$

5.1.2 Derivation of component of the wavevector vertical to the interface in an arbitrary dual uniaxial electromagnetic medium

The wavevector *k* can be separated into two components: component parallel to the interface β and component vertical to the interface γ. Therefore, the relationship between wavevector and the two components of medium *i* can be expressed as $\beta_i^{2}+\gamma_i^{2}=\left|k_i\right|^{2}=n_i^{2}\omega^{2}/c_0^{2}$. According to Ref. [66]:

$$\frac{\beta_i^{2}\varepsilon_{i\|}\mu_{i\|}}{n_i^{2}-\varepsilon_{i\|}\mu_{i\|}}+\frac{\gamma_i^{2}\varepsilon_{i\perp}\mu_{i\perp}}{n_i^{2}-\varepsilon_{i\perp}\mu_{i\perp}}=0 \tag{5.17}$$

By combining the two equations, Eq. (5.17) yields:

$$n_i^{2}\beta_i^{2}\varepsilon_{i\|}\mu_{i\|}+n_i^{2}\gamma_i^{2}\varepsilon_{i\perp}\mu_{i\perp}=\varepsilon_{i\perp}\mu_{i\perp}\varepsilon_{i\|}\mu_{i\|}\left(\beta_i^{2}+\gamma_i^{2}\right)=\varepsilon_{i\perp}\mu_{i\perp}\varepsilon_{i\|}\mu_{i\|}\left(\frac{n_i^{2}\omega^{2}}{c_0^{2}}\right) \tag{5.18}$$

Then Eq. (5.18) yields the general equation of the wavevector component vertical to the interface:

$$\gamma_i = \sqrt{\varepsilon_{i\|}\mu_{i\|}\left(\frac{\omega^2}{c_0^2}\right) - \frac{\varepsilon_{i\|}\mu_{i\|}}{\varepsilon_{i\perp}\mu_{i\perp}}\beta_i^2} \tag{5.19}$$

For s-polarized waves, medium *i* can be considered as isotropic for electric field. Therefore, the two components of permittivity tensor are the same ($\varepsilon_{\|} = \varepsilon_{\perp}$) and Eq. (5.19) yields the vertical component of wavevector for s-polarized waves:

$$\gamma_i^s = \sqrt{\varepsilon_{i\|}\mu_{i\|}\frac{\omega^2}{c_0^2} - \frac{\mu_{i\|}}{\mu_{i\perp}}\beta_i^2} \tag{5.20}$$

Similarly for p-polarized waves, medium *i* can be considered as isotropic for magnetic field with p-polarized waves. Therefore, with $\mu_{\|} = \mu_{\perp}$, Eq. (5.19) yields the vertical component of wavevector for p-polarized waves:

$$\gamma_i^p = \sqrt{\varepsilon_{i\|}\mu_{i\|}\frac{\omega^2}{c_0^2} - \frac{\varepsilon_{i\|}}{\varepsilon_{i\perp}}\beta_i^2} \tag{5.21}$$

5.1.3 Derivation of single interface SPP condition for dual uniaxial electromagnetic media

For the interface between air and a dual uniaxial electromagnetic metamaterial, the dispersion curve of single interface m-SPP can be calculated by:

$$\mu_{1\|}\gamma_0 + \gamma_1^s = 0 \tag{5.22}$$

where

$$\gamma_0^s = \sqrt{\omega^2 / c^2 - \beta^2} \tag{5.23}$$

and $$\gamma_1^{\,s} = \sqrt{\varepsilon_{1||}\mu_{1||}\omega^2 / c^2 - \frac{\mu_{1||}}{\mu_{1\perp}}\beta^2} \tag{5.24}$$

Therefore, Eq. (5.22) yields:

$$\mu_{1||}\sqrt{\omega^2 / c^2 - \beta^2} + \sqrt{\varepsilon_{1||}\mu_{1||}\omega^2 / c^2 - \frac{\mu_{1||}}{\mu_{1\perp}}\beta^2} = 0 \tag{5.25}$$

By assuming $\beta \approx \omega/c$, Eq. C4 yields $\gamma_1\gamma_0 = 1$. Similarly, the dispersion curve of single interface e-SPP between air and a dual uniaxial electromagnetic metamaterial can be obtained by:

$$\varepsilon_{1||}\gamma_0 + \gamma_1^{\,p} = 0 \tag{5.26}$$

By plugging in the equations of γ_0 and $\gamma_1{}^p$ along with the assumption of $\beta \approx \omega/c$, the condition $\varepsilon_1\varepsilon_0 = 1$ can be derived for e-SPP.

5.2 Homogeneous Anisotropic Metamaterials with Magnetic Responses

This study focuses on the theoretical analysis of near-field radiative heat transfer between two semi-infinite dual uniaxial electromagnetic metamaterials. In order to reveal the possible additional modes for enhancing near-field thermal radiation, two homogeneous media with two different material property sets will be investigated. The near-field radiative heat transfer is calculated by fluctuational electrodynamics incorporated with anisotropic wave optics by taking into account the electromagnetic responses to both s and p polarized waves. Enhancement modes along with the associated mechanisms will be understood by the energy transmission coefficients and spectral heat

fluxes for different material property sets. Furthermore, the effect of vacuum gap distance on the total heat flux will be discussed at different wave polarizations.

Figure 5.1 depicts near-field radiative heat transfer between two semi-infinite homogeneous metamaterials separated by a vacuum gap *d* to be analyzed in this study. The emitter (Layer 1) is kept at 400 K and the receiver (Layer 2) is at 300 K. The electromagnetic metamaterials are considered to be identical for simplicity, while both respond to electrical and magnetic fields with permittivity ε and permeability μ respectively expressed by Drude and Lorentz models [67, 68]: The electromagnetic metamaterials are considered identical for simplicity, while both respond to electrical and magnetic fields with permittivity ε and permeability μ that are expressed by the Drude and Lorentz models [67, 68]:

$$\varepsilon = 1 - \frac{\omega_p^2}{\omega^2 + i\omega\gamma_e} \tag{5.27}$$

and

$$\mu = 1 - \frac{F\omega^2}{\omega^2 - \omega_0^2 + i\omega\gamma_m} \tag{5.28}$$

where $F = 0.56$ is the split ring filling ratio factor, $\omega_p = 10^{14}$ rad/s is the equivalent plasma frequency, $\omega_0 = 0.4\omega_p$ is the effective resonance frequency, and $\gamma_e = \gamma_m = 0.01\omega_p$ are the electrical and magnetic scattering rates, respectively [67]. Figure 2 plots the real parts of the electrical permittivity ε and magnetic permeability μ respectively expressed by Drude and Lorentz models. Clearly, the electromagnetic metamaterial exhibits metallic behavior, i.e., $\mathrm{Re}(\varepsilon) < 0$, only at lower frequencies $\omega < \omega_p$. On the other hand, it shows negative magnetic response with $\mathrm{Re}(\mu) < 0$ within a narrow frequency band of

$\omega_0 < \omega < \omega_0/\sqrt{1-F}$ when $\gamma_m \ll \omega$. Note that, when the uniaxial material properties are described by effective medium theory, the vacuum gap should be larger than the unit size of the metamaterial [69].

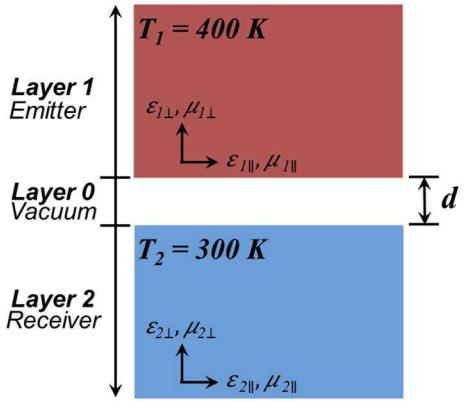

Fig. 5.1 The schematic of two homogeneous semi-infinite magnetically anisotropic metamaterials at different temperatures separated by a nanometer vacuum gap *d*.

In order to study the effect of anisotropic material properties on the near-field radiative transfer, both media are assumed to be uniaxial with ordinary permittivity and permeability components following the Drude an Lorentz models, i.e., $\varepsilon_{\parallel} = \varepsilon$ and $\mu_{\parallel} = \mu$, while the extraordinary permittivity and permeability components being either 1 or –1, i.e., $\varepsilon_{\perp} = \mu_{\perp} = 1 \text{ or } -1$. These two different property sets of homogenous uniaxial electromagnetic metamaterials, also listed in Table 5.1, are considered here to study possible near-field enhancement mechanisms because of the responses to both electrical and magnetic fields.

Table. 5.1 Two different property sets of homogeneous uniaxial electromagnetic metamaterials to be studied for near-field radiative heat transfer.

Property Sets	$\varepsilon_{\parallel}$	$\varepsilon_{\perp}$	$\mu_{\parallel}$	$\mu_{\perp}$
I	ε	1	μ	1
II	ε	−1	μ	−1

In order to analyze the possible enhancement mechanisms between uniaxial electromagnetic metamaterials, the transmission coefficients ξ as a function of both angular frequency (ω) and normalized parallel wavevector component ($\beta c/\omega$) are first investigated. Figures 5.2(a) and 5.2(b) show the transmission coefficients $\xi(\omega,\beta)$ of property sets I and II under s-polarized waves. Note that, under s polarization, only $\varepsilon_{\parallel}$, which follows the Drude behavior, is involved for the electrical response, while both $\mu_{\parallel}$ and $\mu_{\perp}$ have to be considered for the magnetic response.

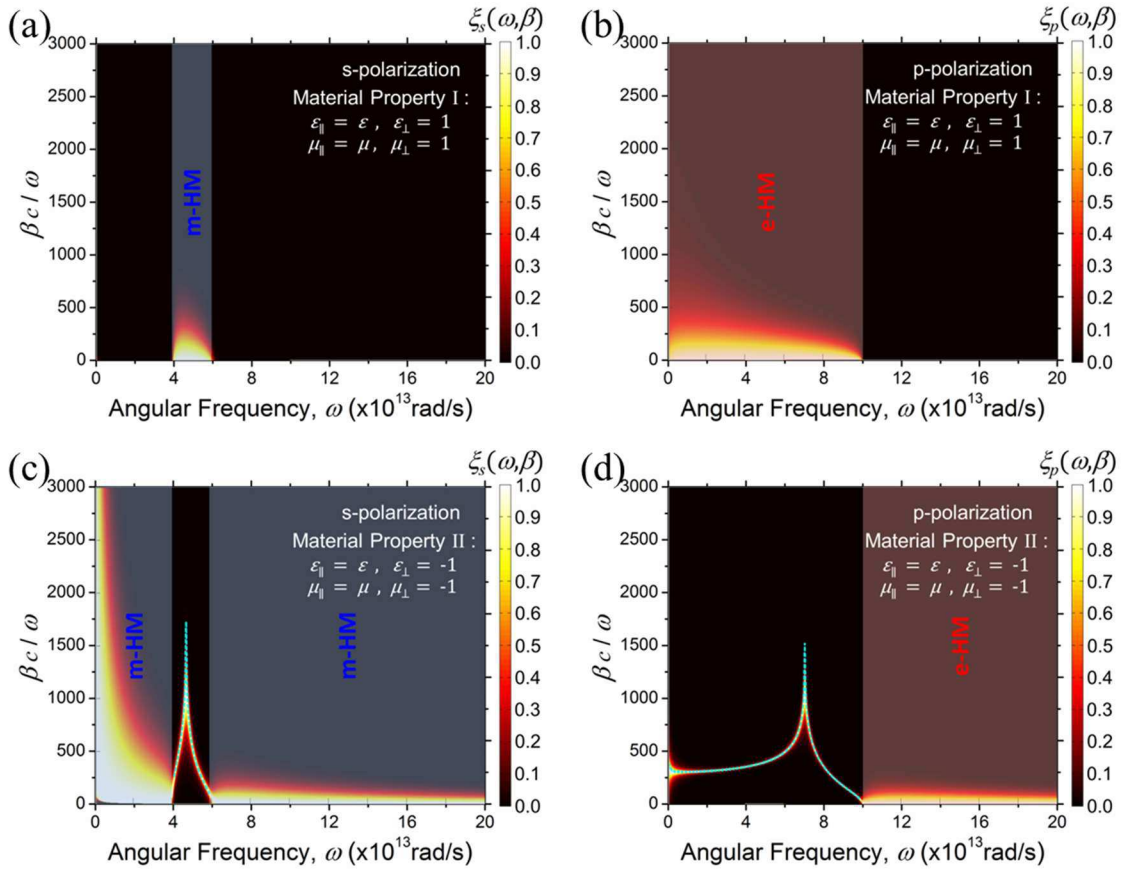

Fig. 5.2 The transmission coefficient of the near-field radiative heat transfer between two semi-infinite magnetically anisotropic metamaterials for s-polarized waves with material property sets of: (a) I; (b) II and for p-polarized waves with material property sets of: (c) I; (d) II. The vacuum gap distance is d = 20 nm.

In Fig. 5.2(a) for the property set I, near-field energy transmission enhancement is observed under the shaded region within the frequency range between 4×10^{13} rad/s < ω < 6×10^{13} rad/s, which is corresponding to the Re($\mu_{\parallel} = \mu$) < 0 region (i.e., $\omega_0 < \omega < \omega_0/\sqrt{1-F}$). Apparently, as $\mu_{\perp} = 1$ or as long as $\mu_{\perp}$ is positive, the near-field enhancement within this narrow spectral band is due to the type 2 (i.e., $\mu_{\parallel} < 0$, $\mu_{\perp} > 0$) magnetic hyperbolic mode (m-HM). Outside of the shaded m-HM region, both $\mu_{\perp}$ °AS $\mu_{\parallel}$

are positive. Therefore, no other enhancement modes are supported and the energy transmission is weak as observed.

For the property set II with $\mu_{\perp}= -1$ instead of 1, as shown in Fig. 5.2(b), two broad enhancement bands are observed at frequencies $\omega < 4\times10^{13}$ rad/s and $\omega > 6\times10^{13}$ rad/s, in which Re($\mu_{\parallel}$) is positive. Therefore, the broadband near-field enhancements at $\omega < \omega_0$ and $\omega > \omega_0/\sqrt{1-F}$ are due to the type 1 m-HM mode as long as $\mu_{\parallel} > 0$ and $\mu_{\perp} < 0$). Besides, within the negative magnetic response region Re($\mu_{\parallel}$) < 0, there exist additional enhancement modes that strongly depend on both frequency ω and wavevector β. By plotting the analytical dispersion relation of coupled magnetic SPP (m-SPP) between the uniaxial metamaterials (blue dashed line in the figure), which is obtained through zeroing the denominator of the transmission coefficient for s-polarized waves, i.e., $1-r_{01}^{s}r_{02}^{s}e^{i2\gamma_0 d}=0$, the perfect agreement with the enhancement bands from the energy transmission coefficient contour undoubtedly confirms the physical mechanism as coupled m-SPP mode. The low and high frequency coupled m-SPP branches merge at the asymptotic frequency where $\mu_{\parallel}\mu_{\perp}= 1$, which is exactly the resonance frequency of m-SPP at a single interface between the uniaxial metamaterial and vacuum (See section 5.1.3 for detailed derivations).

Figures 5.2(c) and 5.2(d) show the transmission coefficients for both material property sets I and II but under p-polarized waves, where only $\varepsilon_{\parallel}$, $\varepsilon_{\perp}$ and $\mu_{\parallel}$ are involved for the electrical and magnetic field responses. For the property set I with $\varepsilon_{\perp}= 1$, a broad enhancement band exists in the energy transmission coefficient contour at low frequencies $\omega < \omega_p = 1\times10^{14}$ rad/s, where $\varepsilon_{\parallel} < 0$ and $\varepsilon_{\perp} > 0$, indicating the type 2 electrical hyperbolic

mode (e-HM). Likewise, there is no near-field enhancement at high frequency range due to the dielectric behavior of the property set I with both positive Re(ε_t) and 2•(ε_n). Note that, enhancements due to the frustrated total internal reflection [70] still exist when the materials express dielectric behavior, but this effect cannot be seen here since it supports wavevector only at $\beta < \sqrt{\varepsilon_{i,\perp}\mu_{i,\parallel}}\omega/c$ according to Eq. (5.20).

As shown in Fig. 5.2(d) for the property set II with $\varepsilon_n = -1$ under p-polarized waves, there exists broadband enhancement at high frequencies $\omega > \omega_p = 1\times10^{14}$ rad/s due to type 1 e-HM mode with $\varepsilon_t > 0$ and $\varepsilon_n < 0$, as well as coupled electrical SPP (e-SPP) mode at low frequency region $\omega < \omega_p$, in comparison to the narrow m-SPP mode excited by s-polarized waves in Fig. 5.2(b). The dispersion curves of coupled e-SPP modes are also shown by solving $1 - r_{01}^{p} r_{02}^{p} e^{i2\gamma_0 d} = 0$. Similarly, the two branches of coupled e-SPP modes merges at the asymptotic frequency for that at a single interface where $\varepsilon_t\varepsilon_n = 1$ (See section 5.1.3 for detailed derivation).

Note that the enhancement bands associated with m-HM at s polarization and e-HM modes at p polarization are complimentary and cover the entire frequency spectra for both property sets I and II. Furthermore, SPP modes would never occur for the property set I with $\mu_n = \varepsilon_n = 1$ at either s or p polarizations as positive μ_n and ε_n cannot satisfy the m-SPP or e-SPP excitation conditions. On the other hand, for the property set II with $\mu_n = \varepsilon_n = -1$, both m-SPP and e-SPP modes can be excited respectively under s and p-polarized waves. Note that, the conditions provided here are only for coupled SPP modes between the same materials where the asymptotic frequencies are the same as those at the single interface SPP modes given by $\mu_t\mu_n = 1$ for m-SPP and $\varepsilon_t\varepsilon_n = 1$ for e-SPP between dual

uniaxial metamaterials and vacuum. Both conditions are derived through the assumption of $\beta \gg \omega/c$, which turns out to be respectively regardless of ε_r and μ_r (See section 5.1.3).

The spectral heat fluxes $q(\omega)$ can be obtained by integrating the transmission coefficient over β. Figures 5.3(a) and 5.3(b) present the spectral heat fluxes $q(\omega)$ with different property sets under s and p polarizations, respectively. The green shaded areas indicate the regions where $\mathrm{Re}(\mu_r = \mu) < 0$ at s polarization and $\mathrm{Re}(\varepsilon_r = \varepsilon) < 0$ at p polarization. For the property set I, the spectral heat flux is significantly enhanced only within the shaded regions because of the type 2 m-HM and e-HM modes respectively at each s and p polarization. As no coupled SPP modes exist, the spectral heat flux abruptly decreases at frequencies outside of the negative μ_r and ε_r regions. On the other hand, for the property set II, the spectral heat flux exhibits strong enhancement within the shaded regions due to coupled m-SPP and e-SPP modes which agrees with the negative μ_r and ε_r regions. More importantly, the type 1 m-HM and e-HM modes elsewhere exhibit at least 4 orders of magnitude enhancement under both s and p polarizations in comparison with the property set I. Note that, the coupled SPP modes result in narrow-band spectral heat flux peaks within the negative μ_r and ε_r regions, whose magnitude is even about one order greater than that associated with the broadband type 2 hyperbolic modes with the property set I.

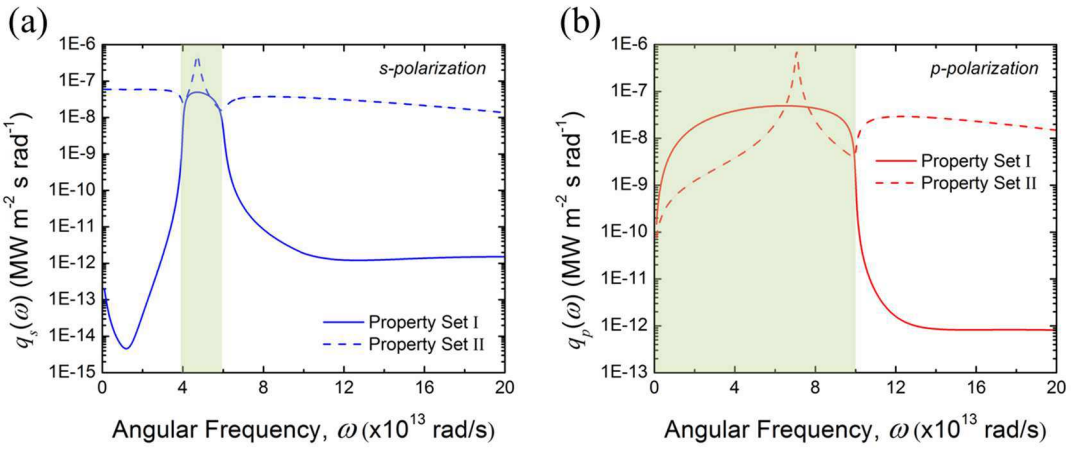

Fig. 5.3 Spectral heat flux between two semi-infinite uniaxial electromagnetic metamaterials with material property sets of I and II separated by a vacuum gap d = 20 nm for (a) s-polarized waves; (b) p-polarized waves.

Clearly, these two property sets with either positive or negative $\mu_{\text{ضد}}$ and $\varepsilon_{\text{ضد}}$ could lead to significantly different spectral heat flux distributions, which would be favored for different applications. For example, the broadband flux enhancement associated with type 2 hyperbolic modes provided by the material property set I or with type 1 hyperbolic modes from the set II, could be useful for augmentation or suppression of radiative heat transfer within the spectral range of interests. The narrow-band flux enhancement or wavelength-selective control of near-field radiative transfer due to coupled SPP modes are highly desired for enhancing thermal energy harvesting and conversion applications like thermophotovoltaics. Moreover, the flux enhancement over the entire spectrum by taking advantage of both HM and SPP modes is of great benefit for thermal management and heat dissipation. Besides, by suitably selecting the materials with either Drude or Lorentz behaviors respectively for the electrical permittivity ε or magnetic permeability μ, these

heat flux enhancement or the HM and SPP modes can be activated selectively for either s or p polarization, which would facilitate polarization-sensitive applications.

Finally, the effect of vacuum gap distance d on the total heat flux is investigated for the two property sets of dual uniaxial metamaterials in comparison with those for two isotropic cases, one of which possesses the electrical permittivity $\varepsilon_z = \varepsilon_x = \varepsilon$ described by the Drude model in Eq. (5.27) and magnetic permeability $\mu_z = \mu_x = 1$ (i.e., nonmagnetic) and the other isotropic metamaterial has $\mu_z = \mu_x = \mu$ given by the Lorentz model in Eq. (5.28). Figure 5.4(a) shows the total heat fluxes of four different materials for s-polarized waves as a function of d. As the vacuum gap distances decrease from 10 μm to 10 nm, the near-field heat fluxes under s polarization for all three metamaterials with magnetic responses increase monotonically and could exceed the far-field blackbody limit by more than 3 orders except for non-magnetic isotropic material (ε, $\mu = 1$). It is well known that the near-field heat flux at s-polarized waves between non-magnetic isotropic metals is small due to weak coupling of evanescent waves [25, 29] and in this case, the flux is about one order of magnitude smaller than the blackbody limit and little changes with gap distances. For the isotropic metamaterial (ε, μ) with magnetic responses, the s-polarized total heat flux q is much enhanced with d^{-2} dependence due to the excitation of coupled m-SPP modes whose strengths increases significantly at smaller vacuum gaps, as studied in Ref. [67]. However, for the dual uniaxial metamaterials with the property set I, the total heat flux is slightly lower than that for isotropic metamaterials, mainly because only m-HM within the limited $\mathrm{Re}(\mu_z = \mu) < 0$ region but no m-SPP modes exist, as shown in Figs. 5.2(a) and 5.3(a). Moreover, as the dual uniaxial metamaterials with the property set II

could excite both m-SPP and type 2 m-HM modes within a broad spectral region, the total heat flux under s polarization can be enhanced to be more than 4 orders greater than the blackbody limit, which is about 1 order more than that for isotropic metamaterials.

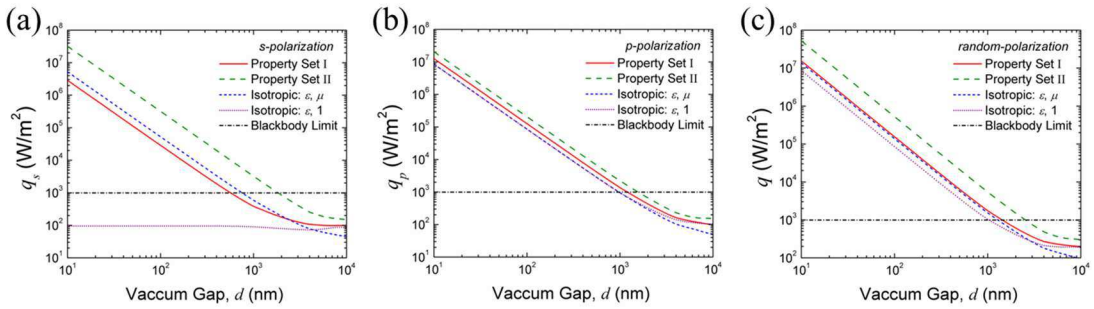

Fig. 5.4 Normalized total heat fluxes between two semi-infinite uniaxial electromagnetic metamaterials with different sets of material properties with respect to different vacuum gap d for (a) s-polarized waves; (b) p-polarized waves; (c) randomly polarized waves.

Figure 5.4(b) presents the gap distance effect on the total heat flux for p-polarized waves; while the fluxes for all four materials exhibit d^{-2} dependence as the vacuum gap becomes smaller, exceeding the blackbody limit up to 4 orders of magnitudes. The two isotropic materials (ε, μ = 1) and (ε, μ) have almost the same heat fluxes since for p polarization, the identical electrical permittivity ε results in the same coupled-SPP resonant modes for near-field heat enhancement, regardless of magnetic response. The total heat flux is further enhanced with dual uniaxial electromagnetic metamaterials. As discussed previously in Figs. 5.2(c) and 5.2(d) for p polarization, the uniaxial metamaterial with property set I has broadband type 2 e-HM mode at frequencies $\omega < \omega_p$, while the uniaxial metamaterial with property set II exhibits broadband type 1 e-HM mode at high frequencies $\omega > \omega_p$ and strong coupled e-SPP modes at low frequencies $\omega < \omega_p$. As a result, the uniaxial metamaterial with property set II could achieve the highest total heat flux by 2.5 times

more than that with the isotropic materials. Figure 5(c) shows the overall total heat flux for randomly polarized waves by adding those from s and p polarizations. Clearly, the contribution from s-polarized waves are significant and thus not negligible compared with that from p-polarized waves for all three metamaterials but not the non-magnetic isotropic material ($\varepsilon, \mu = 1$). In fact, the combined total heat flux under randomly polarized waves for the dual uniaxial metamaterials with the property set II is about 4 times higher than that with the property set I, which is slightly greater than the flux for the isotropic magnetic metamaterials.

5.3 Inhomogeneous Nanowire Magnetic Metamaterials

This section aims to theoretically analyse the near-field radiative heat transfer between two semi-infinite dual uniaxial electromagnetic metamaterials made of nanowire arrays. The inhomogeneous properties of the nanowire based metamaterial are homogenized by Maxwell-Garnett EMT. Furthermore, the effects of material properties such as filling ratio, magnetic scattering rate, and electrical scattering rate will all be demonstrated by the energy transmission coefficients and spectral heat fluxes as well as the effect of vacuum gap distance.

A configuration of the near-field radiative heat transfer between two semi-infinite nanowire array based inhomogeneous media separated by a vacuum gap d analyzed in this study is shown in Fig. 5.5. The nanowires are considered to be dual uniaxial electromagnetic metamaterials which possess permeability μ and permittivity ε modeled by Eqs. (5.27) and (5.28) to account the responses to both magnetic and electrical fields. The emitter (Layer 1) is kept at 400 K and the receiver (Layer 2) is at 300K.

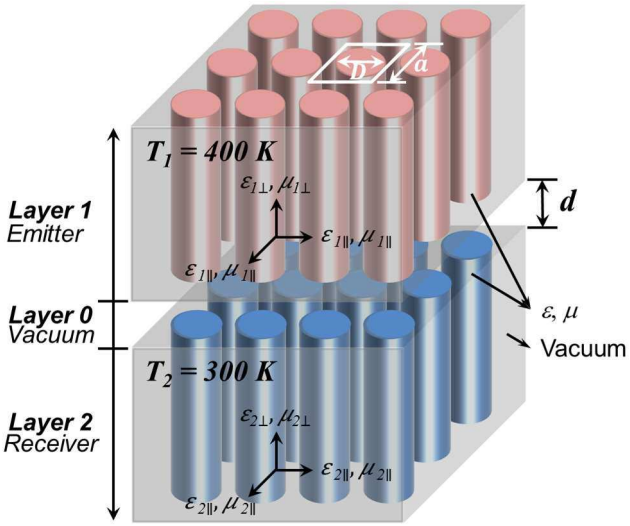

Fig. 5.5 The schematic of two nanowire based inhomogeneous semi-infinite magnetically anisotropic metamaterials at different temperatures separated by nanometer vacuum gap d.

Clearly, the effective permittivity and permeability are both highly dependent of filling ratio f and scattering rates γ_e and γ_m. The effect of these parameters will be thoroughly investigated in chapter 3. Note that, the Maxwell-Garnett EMT assumes that the nanowires are not interacting with each other. Therefore, only small filling ratios ($f <$ 0.5) are investigated in this study [23]. Furthermore, the EMT used here is valid only for nanowires with high aspect ratios ($h/D > 20$) [71] and when the feature size of the nanowire array is much smaller than the vacuum gap and thermal wavelength to ignore the effect of spatial dispersion ($a < \pi d$ and a ≪ $\lambda_{\text{th}} = \hbar c/k_{\text{B}}T$) [13]. Thus, the case between two semi-infinite media is studied with a vacuum gap of 100 nm ($a <$ 314 nm and $\lambda_{\text{th}} = 5.72$ μm for $T = 400$ K) where the period is achievable by feasible fabrication techniques such as electron beam lithography and anodic aluminum oxide.

Figures 5.6(a) and 5.6(b) respectively show the real parts of effective uniaxial permeabilities and permittivities under different filling ratios. Overall the material

properties can both be tuned by different filling ratios; but by comparison, the effect of filling ratio is more distinct on permittivity than permeability. For permeability as shown in Fig. 5.6(a), both $f = 0.1$ and 0.3 show positive effective permeability components outside the two narrow bands of magnetic hyperbolic mode (m-HM) which can be identified with different signs of $\mu_{\parallel}$ and $\mu_{\perp}$. However, when it comes to higher filling ratio such as $f = 0.5$, there exists a small frequency band of negative magnetic response region between the two m-HM bands where both Re($\mu_{\parallel}$) and Re($\mu_{\perp}$) are less than zero. As for permittivity, figure 5.6(b) demonstrates that different filling ratios provide more tunability on the distribution of effective permittivity components. Similarly, the frequency bands of electrical hyperbolic mode (e-HM) at both high and low frequencies can again be determined by opposite signs of Re($\varepsilon_{\parallel}$) and $2 \bullet (\varepsilon_{\perp})$. On the other hand, due to the effects of increasing filling ratio on the Drude nature of $\varepsilon_{\perp}$ and the Lorentz behavior of $\varepsilon_{\parallel}$, effective metallic behavior takes place at high filling ratios between the two e-HM bands. Note that, compared with permeability where poles are presented due to Lorentz mode, the Drude nature of ε is displayed on $\varepsilon_{\perp}$ which can potentially provide broadband hyperbolic enhancement modes for p-polarized waves.

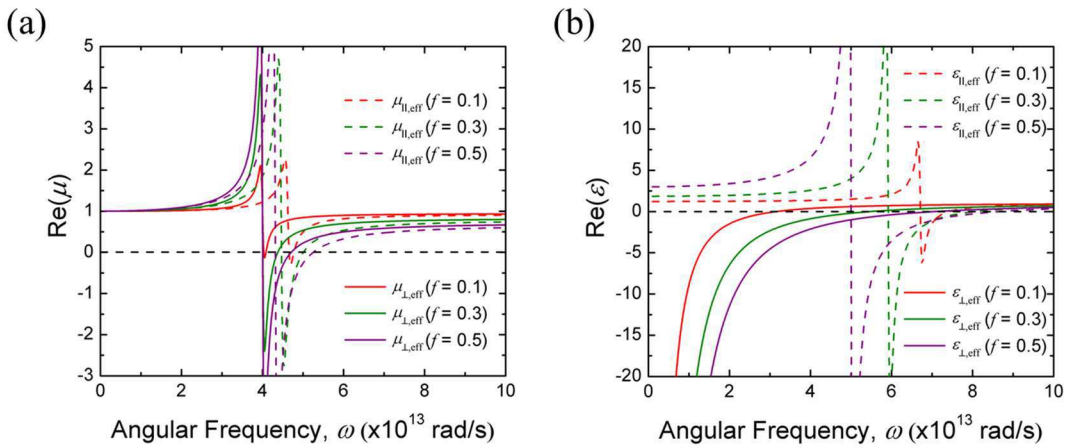

Fig. 5.6 The effect of filling ratio on material properties of the nanowire based electromagnetic metamaterial: real part of (a) effective permeability and (b) effective permittivity.

Figure 5.7 presents the distribution of transmission coefficients in both frequency and normalized wave vector domains corresponding to different filling ratios and wave polarizations. As shown in Figs. 5.7(a-c) for s-polarized waves, the enhancement and shifting of transmission coefficients match the frequency bands of m-HM modes (shaded regions) identified through Fig. 5.6(a) perfectly. Other than the m-HM modes, the effects of epsilon-near-pole (ENP) mode (i.e., the dark blue dashed lines) can also be seen in Figs. 5.7(a) and 5.7(b) which corresponds to the frequencies of the pole shapes of ε_x illustrated in Fig. 5.6(b). This is because for s-polarized waves, the material can be considered as an electrical isotropic medium with the permittivity of ε_x. Furthermore, as shown by Fig. 5.7(c) with filling ratio of 0.5, the negative magnetic response region supports a strong resonance enhancement which indicates more channels for energy transport in the near-field (reaches larger wavevector β). This resonance mode is identified as magnetic surface plasmon polariton (m-SPP) mode through comparing with the analytical dispersion relation of coupled m-SPP (i.e., the light blue dashed line) between uniaxial media. The dispersion curve is obtained by zeroing the denominator of the transmission coefficient for s-polarized waves, i.e., $1 - r_{01}^{s} r_{02}^{s} e^{i2\gamma_0 d} = 0$.

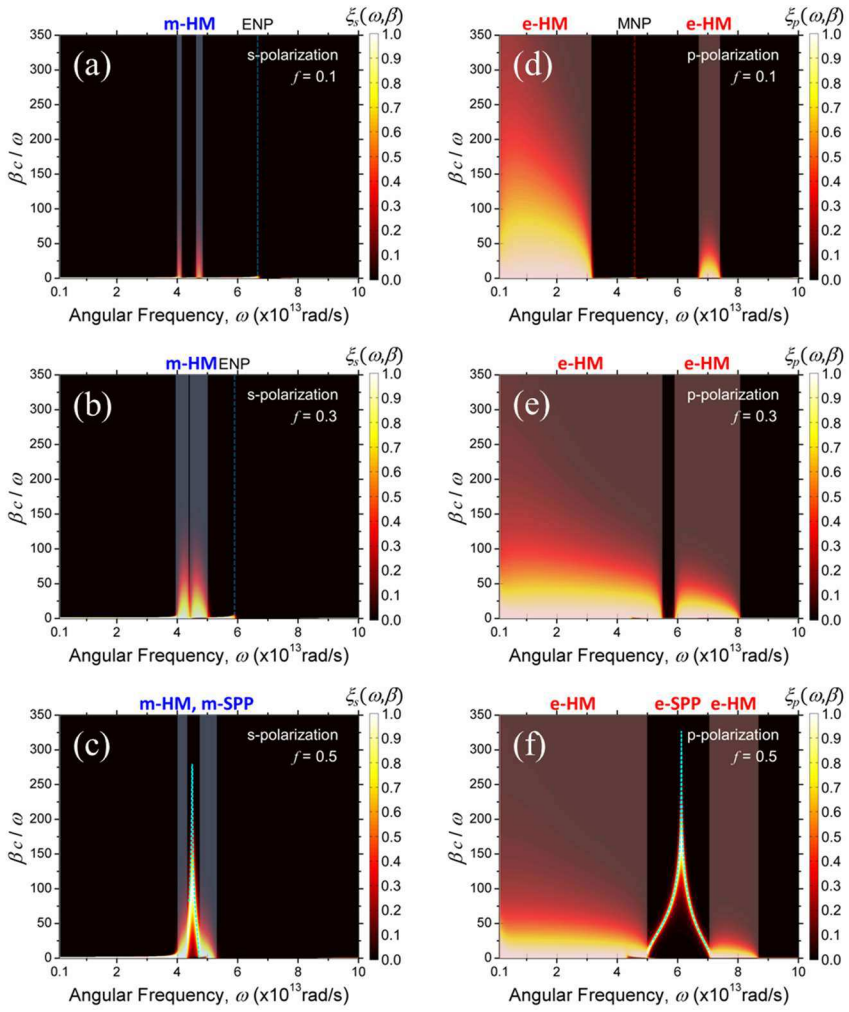

Fig. 5.7 Transmission coefficient ξ of the near-field radiative heat transfer from two semi-infinite free standing nanowire arrays for s-polarized waves with filling ratio of: (a) 0.1; (b) 0.3; (c) 0.5; and for p-polarized waves with filling ratios of: (d) 0.1; (e) 0.3; (f) 0.5. The vacuum gap distance is d = 100 nm and both the electrical and magnetic scattering rates are set to be 0.01 ω_p.

Figures 5.7(d-f) show the distribution of transmission coefficient for p-polarized waves. Likewise, the shifting of the two e-HM enhancement modes agrees with the effect of filling ratio on effective permittivity components. Moreover, the effective metallic behavior occurs at the frequency band where the two e-HM modes overlap due to

increasing filling ratio. The electrical surface plasmon polariton (e-SPP) mode is excited in this region which is again confirmed by the analytical dispersion curve of e-SPP mode ($1-r_{01}^{p}r_{02}^{p}e^{i2\gamma_0 d}=0$). In addition, though not as distinct as HM or SPP modes, mu-near-pole (MNP) can still be observed here while μ_{ξ} presents a pole shape for p-polarized waves [72]. Similarly, this is contributed by the pole shape of Re(μ_{ξ}) that leads to a spike of Im(μ_{ξ}) which represents the loss inside the medium. However, MNP mode can only be seen in Fig. 5.7(d) when filling ratio is 0.1 because the frequency of the mode overlaps with the broadband e-HM mode at high filling ratios as shown in Fig. 5.6(a). Note that, the enhancement of both ENP and MNP modes can also be seen by transmission coefficient but are supported by less channels of heat transfer (i.e., $\beta<10$) and therefore cannot clearly be seen in Figs. 5.7(a), 5.7(b), and 5.7(d) compared with other modes.

The effect of filling ratio on spectral heat fluxes between two inhomogeneous uniaxial electromagnetic metamaterials is demonstrated by Figs. 5.8(a) and 5.8(b) with different wave polarizations. As shown in Fig. 5.8(a), the two m-HM enhancement bands (type I on the left and type II on the right) broaden and shift toward each other with increasing filling ratio, which eventually results in a sharp m-SPP mode around 4.5* 10^{13} rad/s between the two modes at high filling ratios (i.e., $f^{\downarrow}$ 0.4) when the two bands overlap with each other. The m-SPP resonance can clearly be identified by the strong and sharp enhancement peaks on spectral heat flux with more than one order of magnitude stronger than the m-HM modes. In addition, other than the enhancements of m-HM and m-SPP modes, there exists resonance peaks at higher frequency range with smaller filling ratios (i.e., $f^{\uparrow}$ 0.4) which is due to the enhancement of ENP modes. For comparison, the positions of the poles presented by ε_{ξ} are also plotted in the figure with colored semi-transparent

horizontal lines which match the enhancement peak perfectly. On the other hand for ENP modes supported by filling ratio of 0.5; however, cannot be observed in the figure since it is overlapping with other modes. Similar behavior is also demonstrated by Fig. 5.8(b) with p-polarized waves while the difference of enhancement strength between e-HM and e-SPP modes can reach about two orders of magnitude. However, since increasing filling ratio results in the red shift of MNP frequency while it also expands the broadband e-HM mode at low frequency towards higher frequency range, the effect of MNP mode can only be seen at $f = 0.1$.

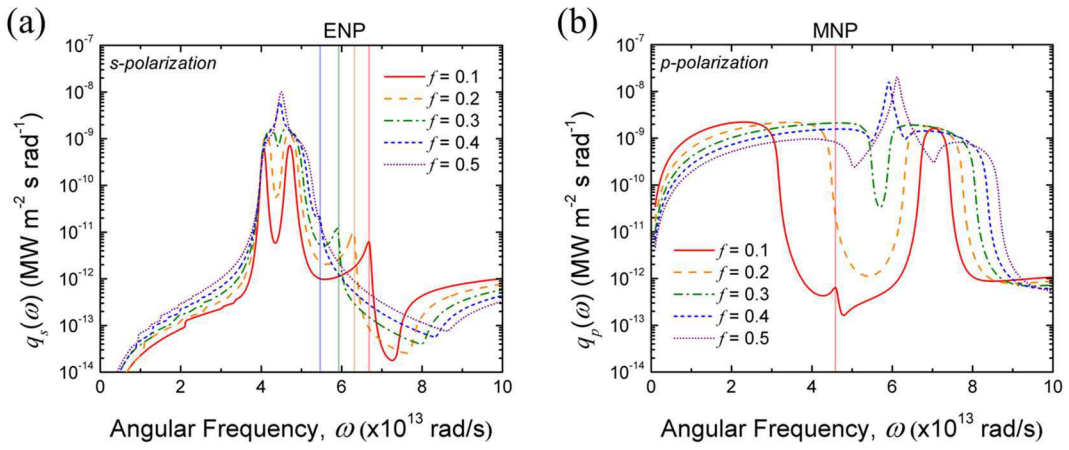

Fig. 5.8 Spectral heat flux from two semi-infinite free standing nanowire arrays with different filling ratios separated by a vacuum gap $d = 100$ nm: (a) s-polarized waves; (b) p-polarized waves. Both the electrical and magnetic scattering rates are set to be $0.01\,\omega_p$.

The effects of magnetic and electrical scattering rates (i.e., γ_m and γ_e respectively) are also investigated in this study by altering the magnitude from $0.01\,\omega_p$ to $0.5\,\omega_p$ rad/s. In order to simplify the effect, the scattering rates of the emitter and receiver are again chosen to be the same at $d = 100$ nm. The filling ratios of emitter and receiver are both fixed at 0.5 in order to clearly observe the effects of the two main enhancement modes: HM and SPP modes. Figure 5.9(a) reveals the effect of magnetic scattering rate on the uniaxial

permeability which the two pole peaks weaken and broaden by increasing scattering rate. On the other hand for permittivity as shown in Fig. 5.9(b), resembling phenomena occurs for $\varepsilon_{\parallel}$ but not for $\varepsilon_{\perp}$. The vertical component of permittivity deviates only at lower frequencies and barely changed at higher frequencies.

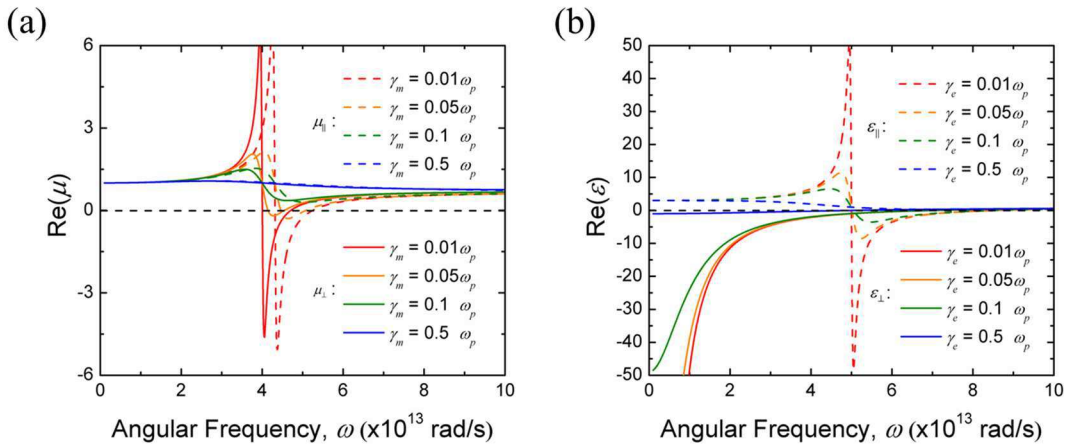

Fig. 5.9 The effect of electrical and magnetic scattering rates on material properties of the nanowire based electromagnetic metamaterial considering f = 0.5: (a) effective permeability and (b) effective permittivity.

As shown by Fig. 5.10, different scattering rates result in different enhancements on transmission coefficients. For s-polarized waves as revealed by Figs. 5.10(a-c) while electrical scattering rate γ_e is fixed at $0.01\,\omega_p$, the two m-HM modes are both first slightly enhanced while the frequency bands almost remain the same with increasing magnetic scattering rate and then vanished since the two components of the permeability no longer have different signs. Interestingly while the two m-HM modes disappeared, the enhancement due to ENP mode takes over and dominates when γ_m reaches $0.5\,\omega_p$. As for the m-SPP mode between the two m-HM modes; however, is significantly weakened based on the dispersion curve obtained and vanishes along with the two m-HM modes. Similar

to the effect of γ_e, it is also discovered from Figs. 5.10(d-f) that the e-HM and e-SPP modes are weakened and eventually vanished with increasing γ_e for p-polarized waves when the magnetic scattering rate γ_m is fixed at $0.01\,\omega_p$. However, since the effect of γ_e on ε_{eff} is not as distinct at the point ε_{eff} passes zero, the broadband e-HM mode at low frequency range remains almost unaffected.

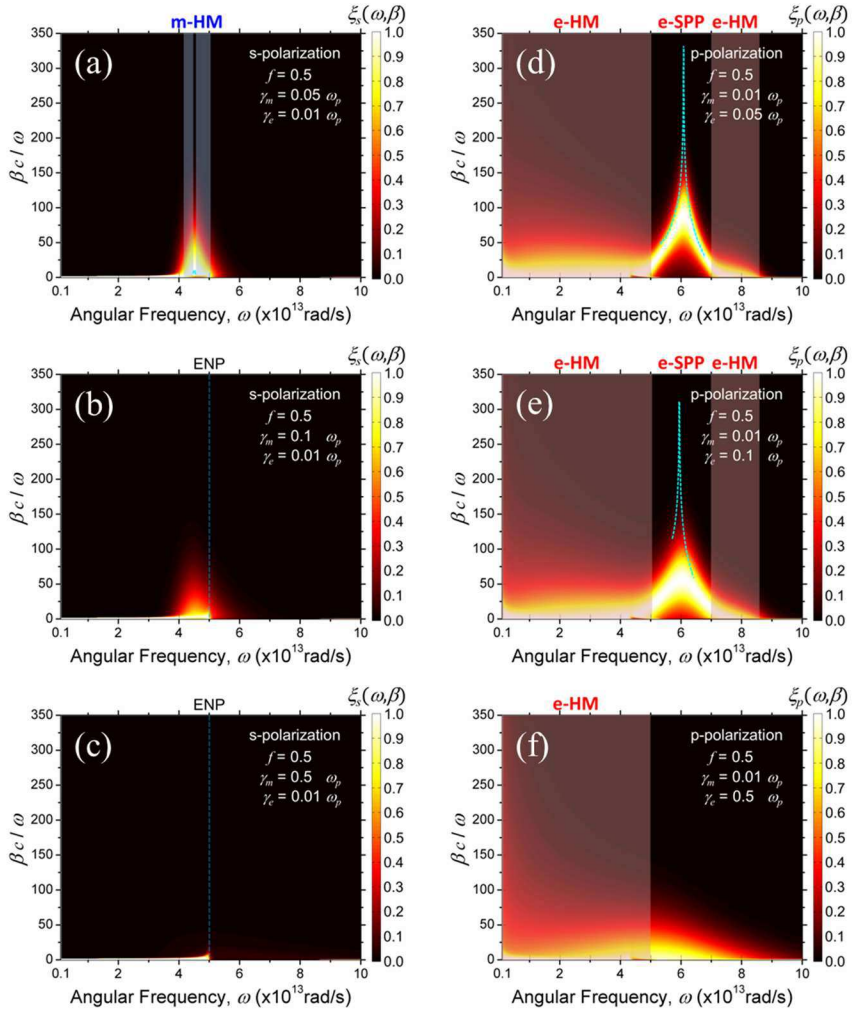

Fig. 5.10 Transmission coefficient ξ of the near-field radiative heat transfer from two semi-infinite free standing nanowire arrays for s-polarized waves with magnetic scattering rate of: (a) $0.05\,\omega_p$; (b) $0.1\,\omega_p$; (c) $0.5\,\omega_p$; and for p-polarized waves with electrical scattering rate of: (d) $0.05\,\omega_p$; (e) $0.1\,\omega_p$; (f) $0.5\,\omega_p$. The vacuum gap distance is d = 100 nm and the

filling ratio is $f = 0.5$.

The spectral heat fluxes associated with different scattering rates and wave polarizations are plotted in Fig. 5.11 to compare the effect of scattering rates on the enhancement modes. Figure 5.11(a) demonstrates the effect of magnetic scattering rate γ_m on spectral heat flux with s-polarized waves which clearly shows that increasing magnetic scattering rate will first slightly enhance the two m-HM modes but weakens m-SPP mode and then level off both modes except the small spike due to ENP. On the other hand, the distribution of spectral heat flux flattens and results in more broad and even distribution over the spectrum with increasing magnetic scattering rate at frequency range outside the enhancement modes. This is due to the fact that the imaginary parts of the effective uniaxial permeabilities at the frequency range are magnified with larger magnetic scattering rate (not shown here) which represents higher absorption loss when both the real parts of $\mu_{\perp}$ and $\mu_{\parallel}$ are positive. As for electrical scattering rate γ_e presented in Fig. 5.11(b), the enhancements of e-HM modes at both higher and lower frequencies are not significantly affected before vanishing. This is due to the fact that the Drude behavior of $\varepsilon_{\parallel}$ is almost independent of electrical scattering rate and therefore the effect cannot be seen at frequency range away from the pole of $\varepsilon_{\perp}$ where supports only the e-SPP mode. In addition, the enhancement at frequency band higher than the type II e-HM mode is also due to the high imaginary parts of $\varepsilon_{\perp}$ and $\varepsilon_{\parallel}$ with larger electrical scattering rate while the metamaterial presents effective dielectric behavior (i.e., both the real part of $\varepsilon_{\perp}$ and $\varepsilon_{\parallel}$ are positive).

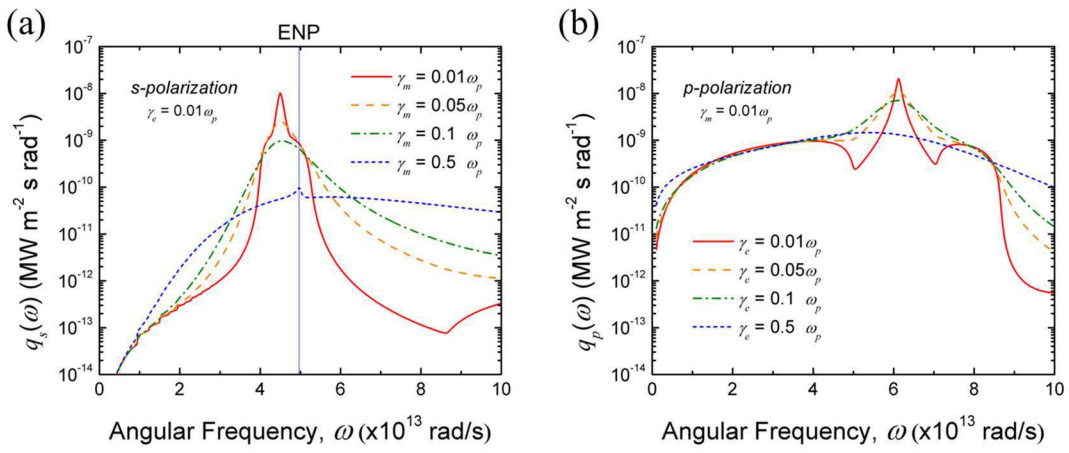

Fig. 5.11 Spectral heat flux from two semi-infinite free standing nanowire arrays with different scattering rates separated by a vacuum gap d = 100 nm: (a) s-polarized waves; (b) p-polarized waves. The filling ratio is f = 0.5.

Note that, for frequency ranges less than 1* 10^{13} and 4* 10^{13} rad/s respectively for s and p polarized waves, the spectral heat fluxes remain almost unaffected by scattering rates. This is because the frequency range is far away enough from the poles of $\mu_{ج}$, $\mu_{جـ}$ and $\varepsilon_{ج}$ where the changes of scattering rates contribute the most. As a result, the effective uniaxial permittivities and permeabilities are not even influenced and thus the spectral heat fluxes are independent of γ_m and γ_e except the deviation of $\varepsilon_{جـ}$ at frequencies less than 2* 10^{13} rad/s. Note that, since the resonance modes are orders of magnitude stronger than the effect of high absorption loss, this effect cannot be seen at resonance bands in either Fig. 5.11(a) or 5.11(b).

Since the effective properties of artificial metamaterials are usually dependent on geometric parameters, specific properties of the inhomogeneous electromagnetic metamaterials are selected here to demonstrate the possibility of high and sharp enhancement peak at certain frequency. Therefore, as SPP modes are mostly strong within

a narrow band while HM modes usually result in broadband enhancements, filling ratio of 0.5 and scattering rates of $0.01\omega_p$ are chosen where the SPP modes are distinct based on previous sections. The effective resonance frequency ω_0 is set to be $0.545\omega_p$ for μ in order to match the two SP modes at different wave polarizations. More importantly, the effect of gap distance will also be analyzed based on the parameters chosen here.

Figure 5.12(a) presents the spectral heat fluxes at different vacuum gap distances with s-polarized waves. Clearly both the two HM modes and the m-SPP mode in between are highly enhanced (about four orders of magnitude enhancement) when reducing the gap distance. The enhancement of ENP mode at small vacuum gap; however, is not as much (enhanced about 10 times). As for the gap distance effect on spectral heat fluxes with p-polarized waves revealed by Fig. 5.12(b), similar phenomena and enhancement strength (also about four orders of magnitude) can also be obtained on both e-HM and e-SPP modes. Note that, since the material property will not change with decreasing gap distance, the enhancement bands of HM, SPP, and NP modes will not be shifted but the enhancement strength will be enhanced by more channels of energy transport. Figure 5.12(c) shows the overall spectral heat flux obtained from the sum of that to two different wave polarizations based on Eq. (3.1). It can clearly be seen that an enhancement peak over two orders of magnitude larger than others is achieved by matching the m-SPP and e-SPP modes at same frequency. Note that even though the contribution of s-polarized spectral heat flux is not that significant compared with that of p-polarized waves; it can still enhance the amount of near-field radiative heat transfer by about 1.5 times.

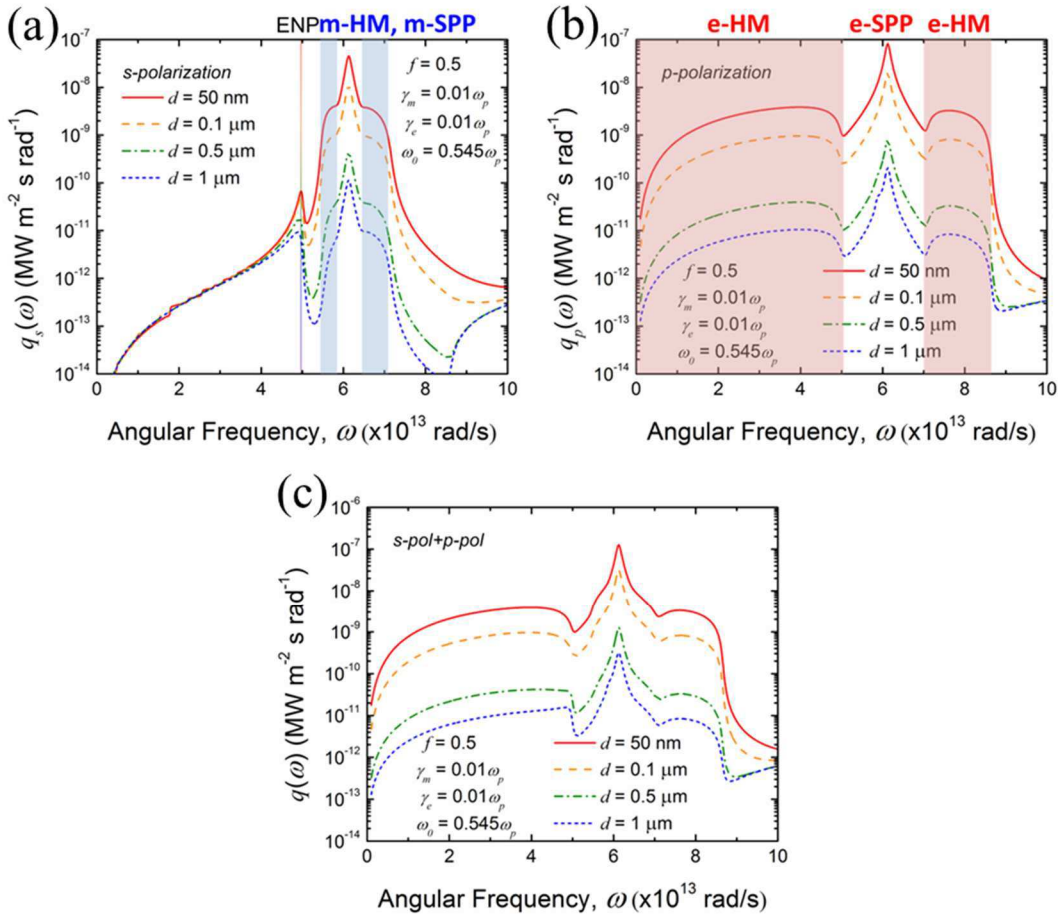

Fig. 5.12 Spectral heat flux from two semi-infinite free standing nanowire arrays with different vacuum gap distances when the filling ratio is $f = 0.5$ and both the electrical and magnetic scattering rates are set to be $0.01\,\omega_p$: (a) s-polarized waves; (b) p-polarized waves; (c) overall summarized from both polarized waves.

Figure 5.13 shows the effect of gap distance on total heat flux under different wave polarizations. It is clear that the total heat flux contributed by s-polarized waves is about 1/3 of that by p-polarized waves at small vacuum gaps (<300 nm). This means that 25% of the overall total heat flux comes from the magnetic response of the metamaterial. With increasing vacuum gap distances, the contribution of s-polarized waves becomes larger and reaches 33% of the overall total heat flux at 10 μm. Although the dominate role of electrical

response is still intact at all gap distances, this proves the concept that the artificial magnetic response in inhomogeneous media should not be excluded in calculations. Note that, compared with the far-field black body limit (blue dotted line), the overall total heat flux surpasses the limit around 1.44 μm which is much larger compared with that of p-polarized waves (1.07 μm). This is showing that the artificial magnetic response of inhomogeneous metamaterials is advantageous for near-filed experiments since the near-field effect kicks in earlier.

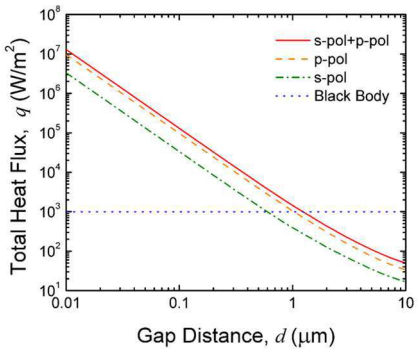

Fig. 5.13 Total heat fluxes of different wave polarizations from two semi-infinite free standing nanowire arrays with different vacuum gap distances when the filling ratio is f = 0.5 and both the electrical and magnetic scattering rates are set to be 0.01 ω_p.

5.4 Parameter Retrieval of Nanowire Magnetic Metamaterials made of Real Nonmagnetic Materials

5.4.1 Background theory of parameter retrieval

The retrieval of homogenized parameters depends on the reflection and transmission coefficients (r and t, respectively) of a metamaterial slab [73] as shown in Fig. 5.14. These coefficients can be obtained by either experimental measurements or rigorous simulation methods such as FDTD. The coefficients will then be used to obtain the incident

angle dependent wave properties [74] through γ and ξ. γ is the ضcomponent of wave vector inside the sample which can be defined as [74]:

$$\gamma^{s/p} d = \pm \cos^{-1} \left\{ \frac{k_s \left[1 - \left(r^{s/p} \right)^2 \right] + k_c \left(t^{s/p} / A^{s/p} \right)^2}{\left(t^{s/p} / A^{s/p} \right) \left[k_s \left(1 - r^{s/p} \right) + k_c \left(1 + r^{s/p} \right) \right]} \right\} + 2m\pi \tag{5.29}$$

where the superscripts s and p respectively represent the polarization of incident wave. The subscripts c and s denote the medium above the metamaterial (cladding) and the substrate underneath as shown in Fig. 5.14, respectively. Therefore, k_c and k_s which are the vertical wave vector components in the respective media, can be defined for different wave polarizations [73]:

$$k_c^{s/p} = \begin{cases} 1/\mu_c \sqrt{\varepsilon_c \mu_c \omega^2 / c^2 - \beta^2} & \text{(s-polarized waves)} \\ 1/\varepsilon_c \sqrt{\varepsilon_c \mu_c \omega^2 / c^2 - \beta^2} & \text{(p-polarized waves)} \end{cases} \tag{5.30}$$

$$k_s^{s/p} = \begin{cases} 1/\mu_s \sqrt{\varepsilon_s \mu_s \omega^2 / c^2 - \beta^2} & \text{(s-polarized waves)} \\ 1/\varepsilon_s \sqrt{\varepsilon_s \mu_s \omega^2 / c^2 - \beta^2} & \text{(p-polarized waves)} \end{cases} \tag{5.31}$$

where ε is the permittivity, μ is the permeability, ω is the angular frequency, c is the speed of light in vacuum, and $\beta = \sqrt{\varepsilon_c \mu_c} \sin\theta_{in} \omega^2 / c^2$ is the wave vector component on ؾ direction conserved within the system across all media. The wave polarization dependent function A in Eq. (5.29) is defined as $A = 1$ for s-polarized waves and $A = \sqrt{\varepsilon_s \mu_c / \varepsilon_c \mu_s}$ for p-polarized waves. The uncertain term m in Eq. (5.29) is an integer which should be chosen to ensure the continuity of γ. That is, the continuity will be checked by the m value while the base value is m = 0. The sign of the first part of γ needs to be changed accordingly for positive imaginary component of γ throughout the whole spectrum. After γ is obtained, the

generalized impedance ξ can also be calculated by [74]:

$$\xi^{s/p} = \pm\sqrt{\frac{\left(k_s^{s/p} r^{s/p} - k_s^{s/p}\right)^2 - \left(k_c^{s/p} t^{s/p} / A^{s/p}\right)^2}{\left(r^{s/p}+1\right)^2 - \left(t^{s/p} / A^{s/p}\right)^2}} \tag{5.32}$$

Here, the sign is determined by the real part of ξ which should always remain positive. $\mu^{s/p}$ and $\varepsilon^{s/p}$ can then be obtained by [74]:

$$\mu^{s/p} = \gamma^{s/p} / \xi^{s/p} \tag{5.33}$$

and

$$\varepsilon^{s/p} = \frac{\beta^2 + \left(\gamma^{s/p}\right)^2}{\mu^{s/p}} \times \frac{c^2}{\omega^2} \tag{5.34}$$

Note that, both $\mu^{s/p}$ and $\varepsilon^{s/p}$ are still angular dependent wave parameters at this stage, not fundamental material properties. However, since an uniaxial homogeneous slab is considered as isotropic at normal incidence without wave polarization dependency (for 2D symmetrical structures only), the fundamental material properties at $\hat{\xi}$ direction can be found by $\mu_{\|,\text{eff}} = \mu^{s/p}(\theta_{\text{in}} = 0)$ and $\varepsilon_{\|,\text{eff}} = \varepsilon^{s/p}(\theta_{\text{in}} = 0)$.

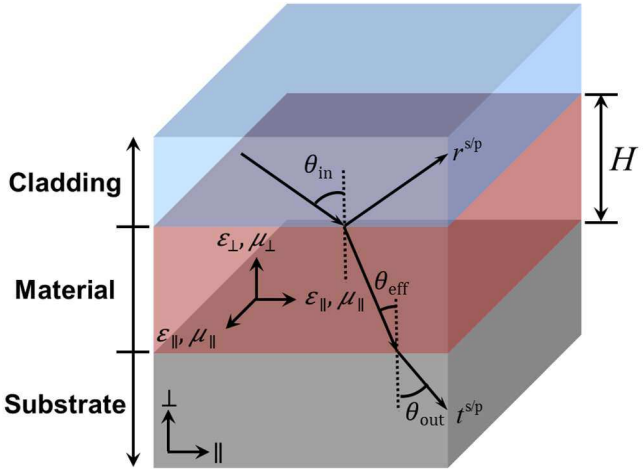

Fig. 5.14 Schematic of a sample (metamaterial) between two semi-infinite media: cladding (upper medium) and substrate (lower medium).

Angular independent $\mu_{\perp,\text{eff}}$ and $\varepsilon_{\perp,\text{eff}}$ can be calculated by solving the two following equations at a certain incident angle [74]:

$$\frac{\beta^2}{\varepsilon_{\parallel,\text{eff}}\mu_{\perp,\text{eff}}}+\frac{\left(\gamma^{\text{s}}\right)^2}{\varepsilon_{\parallel,\text{eff}}\mu_{\parallel,\text{eff}}}=\frac{\omega^2}{c^2} \tag{5.35}$$

$$\frac{\beta^2}{\varepsilon_{\perp,\text{eff}}\mu_{\parallel,\text{eff}}}+\frac{\left(\gamma^{\text{p}}\right)^2}{\varepsilon_{\parallel,\text{eff}}\mu_{\parallel,\text{eff}}}=\frac{\omega^2}{c^2} \tag{5.36}$$

Note that, even though β and γ are still angular dependent, the material properties $\mu_{\perp,\text{eff}}$ and $\varepsilon_{\perp,\text{eff}}$ obtained through Eqs. (5.35) and (5.36) are no longer incident angle dependent. Here, the vertical wave vector component γ must be selected according to the wave polarization where Eq. (5.35) is for TE waves and Eq. (5.36) is for TM waves. From Eqs. (5.35) and (5.36), one can obtain the equations for angular independent $\mu_{\perp,\text{eff}}$ and $\varepsilon_{\perp,\text{eff}}$:

$$\frac{1}{\varepsilon_{\text{eff}}^{\text{s}}\mu_{\text{eff}}^{\text{s}}}=\frac{\sin^2\theta_{\text{eff}}^{\text{s}}}{\varepsilon_{\parallel,\text{eff}}\mu_{\perp,\text{eff}}}+\frac{\cos^2\theta_{\text{eff}}^{\text{s}}}{\varepsilon_{\parallel,\text{eff}}\mu_{\parallel,\text{eff}}} \tag{5.37}$$

$$\frac{1}{\varepsilon_{\text{eff}}^{\text{p}}\mu_{\text{eff}}^{\text{p}}}=\frac{\sin^2\theta_{\text{eff}}^{\text{p}}}{\varepsilon_{\perp,\text{eff}}\mu_{\parallel,\text{eff}}}+\frac{\cos^2\theta_{\text{eff}}^{\text{p}}}{\varepsilon_{\parallel,\text{eff}}\mu_{\parallel,\text{eff}}} \tag{5.38}$$

where
$$\sin^2\theta_{\text{eff}}^{\text{s}}=\left(\frac{\sin\theta_{\text{in}}}{n_{\text{eff}}^{\text{s}}}\right)^2,\ \sin^2\theta_{\text{eff}}^{\text{p}}=\left(\frac{\sin\theta_{\text{in}}}{n_{\text{eff}}^{\text{p}}}\right)^2 \tag{5.39}$$

$$\cos^2\theta_{\text{eff}}^{\text{s}}=\left(\frac{\gamma^{\text{s}}c}{n_{\text{eff}}^{\text{s}}\omega}\right)^2,\ \cos^2\theta_{\text{eff}}^{\text{p}}=\left(\frac{\gamma^{\text{p}}c}{n_{\text{eff}}^{\text{p}}\omega}\right)^2 \tag{5.40}$$

$$\left(n_{\text{eff}}^{\text{s}}\right)^2=\varepsilon_{\text{eff}}^{\text{s}}\mu_{\text{eff}}^{\text{s}},\ \left(n_{\text{eff}}^{\text{p}}\right)^2=\varepsilon_{\text{eff}}^{\text{p}}\mu_{\text{eff}}^{\text{p}} \tag{5.41}$$

For calculation purpose, Eqs. (5.37) and (5.38) can be rewrite as:

$$\mu_{\perp,\mathrm{eff}} = \frac{\sin^2\theta_{\mathrm{eff}}^{\mathrm{s}}}{\dfrac{\varepsilon_{\parallel,\mathrm{eff}}}{\varepsilon_{\mathrm{eff}}^{\mathrm{s}}\mu_{\mathrm{eff}}^{\mathrm{s}}} - \dfrac{\cos^2\theta_{\mathrm{eff}}^{\mathrm{s}}}{\mu_{\parallel,\mathrm{eff}}}} \tag{5.42}$$

$$\varepsilon_{\perp,\mathrm{eff}} = \frac{\sin^2\theta_{\mathrm{eff}}^{\mathrm{p}}}{\dfrac{\mu_{\parallel,\mathrm{eff}}}{\varepsilon_{\mathrm{eff}}^{\mathrm{p}}\mu_{\mathrm{eff}}^{\mathrm{p}}} - \dfrac{\cos^2\theta_{\mathrm{eff}}^{\mathrm{p}}}{\varepsilon_{\parallel,\mathrm{eff}}}} \tag{5.43}$$

5.4.1 Parameter retrieval of nanowire based metamaterials

The targeted structure for parameter retrieval is a freestanding Ag nanowire array as shown Fig. 5.15. The diameter of the nanowires D is chosen to be 200 nm while the period P is 400 nm and the height H is 1000 nm. The host material selected here is air for simplicity.

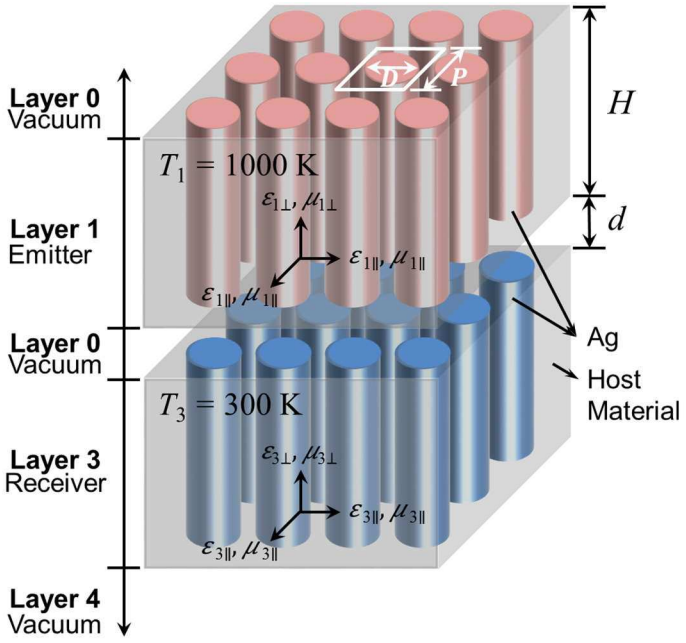

Fig. 5.15 Schematic of a 5-layer near-field radiative heat transfer model between two identical freestanding Ag nanowire arrays with different temperatures.

The reflection and transmission coefficients, r and t respectively, are obtained under

different incident angles (0ص and 45ص) for the retrieval of uniaxial material properties as shown in Fig. 5.16. For normal incidence case as shown in Figs. 5.16(a) and 5.16(b), both coefficients show several peaks and deeps indicating high possibility of enhancement mechanism excitation. The continuity and convergence of both coefficients are also checked here to prevent discontinuity of retrieved properties. Note that, since nanowire arrays are symmetric in both in-plan directions (i.e., ڃ direction), the coefficients obtained at normal incidence are not polarization angle dependent. Figures 5.16(c) and 5.16(d) presents both coefficients at 45ص incident angle under different wave polarizations for retrieving both permittivity and permeability on ض direction. Note that, as shown in Fig. 5.16(d), the transmission coefficient of p-polarized waves is not a lot different compared with the normal incident case shown in Fig. 5.16(b). This is because the geometry is chosen specifically for exciting MP between nanowires as illustrated in chapter 2. That is, the incident angle independency of MP results in the similarity of transmission coefficients at different incident angles.

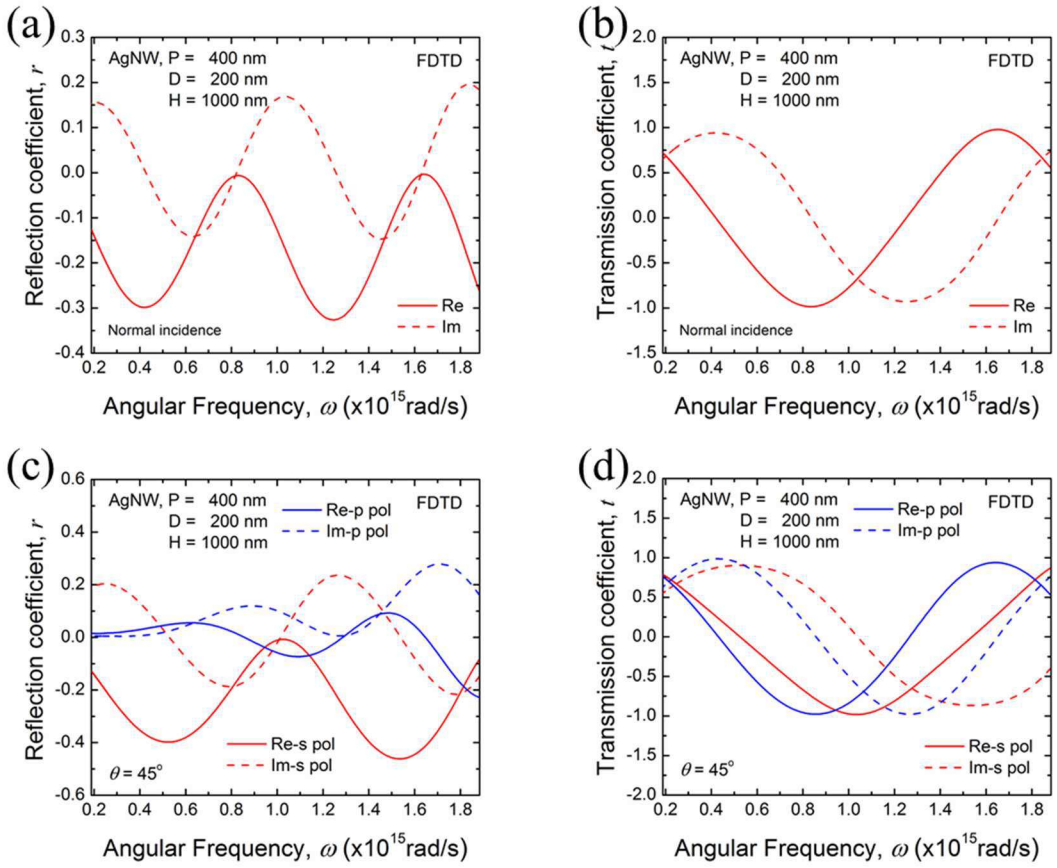

Fig. 5.16 (a) reflection and (b) transmission coefficients obtained by FDTD simulations at normal incident and (c) reflection and (d) transmission coefficients at 45ن incident angle.

Figure 5.17 shows the retrieved angular independent uniaxial material properties. As shown in Fig. 5.17(a), since field averaging by EMT requires non-unity permeability in the first place to present magnetic effective material permeability, the results from EMT remains 1 throughout the investigated spectrum as such material does not naturally exist. The retrieved properties on the other hand however, presents two Lorentz-like mu-near-pole (MNP) behavior at two different frequencies, 8.30* 10^{14} and 1.65* 10^{15} rad/s. These two peaks are in fact correlated to the excitation of MP as it matches the LC circuit model MP peaks prediction. The model used here is a simplified model from Eq. (2.3) while there

are no substrate effect between freestanding nanowires. The non-uniform charge distribution factor c_1 is set to be 0.222 as this is a typical number (usually between 0.2 and 0.3) for models between two parallel plates [42, 75].The predicted MP frequencies are $8.30^{*}\ 10^{14}$ rad/s for MP1 and for $1.66^{*}\ 10^{15}$ rad/s MP2 which matches the MNP peaks perfectly. That is, the retrieved material properties presents the effect of MP by MNP effect. Physically, these two mechanisms are of course not the same, one is artificial resonance effect and the other is the effect of material property. However, since the goal of parameter retrieval is to homogenize the material properties of metamaterials while reflecting the artificial responses, it is actually a reasonable outcome since both mechanisms are narrow band enhancement and have very weak incident angle dependency.

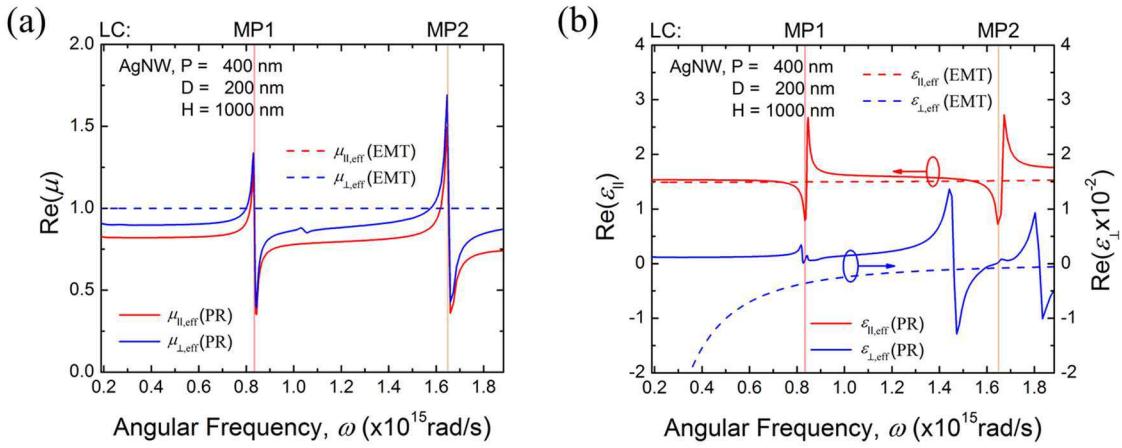

Fig. 5.17 Uniaxial (a) permeability and (b) permittivity retrieved by parameter retrieval compared with EMT and LC circuit model MP peak predictions when the nanowire diameter is 200 nm.

Similarly for permittivity as shown in Fig. 5.17(b), several peaks occur within the frequency range. For the $\varepsilon_{\parallel}$ component, two ENP shapes shows up at the MP frequencies but with anti-symmetric pole shapes compared with MNP. This is in fact due to the inverse

proportional relationship between the effective in-plan permittivity and permeability as presented by Eq. (5.34) since the metamaterial is considered as isotropic with ڰ properties for normal incidence. Therefore, whenever the effective permeability component presents a MNP mode due to the excitation of MP, an anti-ENP mode shows up as a response to the artificial magnetic response. This also reflects on the imaginary part of permittivity while anti-ENP modes also have negative spikes at the resonance frequency. On the other hand for ڧcomponent, it is not as clear to see similar effect. This is due to the fact that instead of applying Eq. (5.34) directly, the ڧcomponents are obtained through Eqs. (5.42) and (5.43) while the components are no longer directly inverse proportional to each other. As a result, the anti-ENP modes can still be seen for ڧcomponents but is much weaker. Other than the anti-ENP modes, there also exists some ENP modes on the ڧcomponent. These are the electrical responses of the metamaterial while the imaginary parts show positive spikes. Note that even though the imaginary part of the ڰ permittivity component has some negative spikes due to anti-ENP modes, the metamaterial is still a positive medium since the imaginary part of effective refractive indexes remains positive that satisfies Kramers-Kronig relation [74].

As for the comparison of EMT and parameter retrieval in Fig. 5.17(b), since EMT cannot predict the MP peaks by effective permeability, the corresponding anti-ENP peaks cannot be seen on the ڰ component as well. For the ڧcomponent, field-averaging EMT obviously gives out a diluted metallic Drude-like behavior along the metallic nanowire direction as usual. Parameter retrieval however, almost did not present any metallic behavior within the range (i.e., real part of permittivity is mostly positive). This can be explained by decreasing the nanowire diameter to 100 nm as shown in Fig. 5.18 while the

LC circuit model still predicts the correct trend of the MP resonance frequency. When the diameter decreases, the EMT predicted permittivity on ضdirection becomes more diluted (but still metallic) while the retrieved property behaves more metallic at higher frequency range in this case. This is because Maxwell-Garnett EMT assumes the fillers are not interacting with each other. In other words, when MP is excited within the frequency range which represents the nanowires are interacting with each other, the prediction of EMT is not accurate even for the electrical response of metamaterials. Therefore, the retrieved permittivity on ضdirection is more metallic as EMT predicted when the nanowire diameter is smaller because the effect of MP weakens with larger distance between nanowires. Note that, even though MP resonance peaks still exist for the 100nm-diameter case, it is much weaker compared to the 200nm-diameter case.

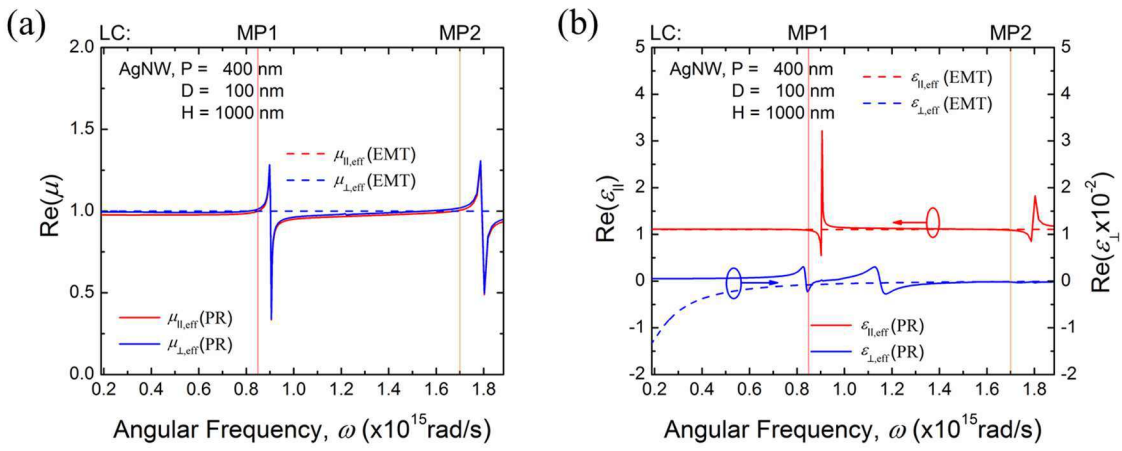

Fig. 5.18 Uniaxial (a) permeability and (b) permittivity retrieved by parameter retrieval compared with EMT and LC circuit model MP peak predictions when the nanowire diameter is 100 nm.

5.5 Near-Field Radiative Transfer by Retrieved Properties

Figure 5.19 shows the spectral heat fluxes for different wave polarizations at different vacuum gap distances with same geometry used in Fig. 5.17 (configuration is presented by Fig. 5.15). For s-polarized waves as shown in Fig. 5.19(a), the two MNP modes due to MP excitation causes narrow band and strong spectral enhancements at both resonance frequencies. In fact, the spectral heat flux is enhanced for more than two orders of magnitude at both resonance frequencies. Furthermore, the spectral heat flux between two Ag plates is also plotted at 100 nm vacuum gap for comparison. It is clear that the spectral heat flux between Ag nanowire arrays is higher at higher frequency range where MNP modes are excited. As for p-polarized waves presented in Fig. 5.19(b), the anti-ENP modes actually suppress the spectral heat flux due to the negative imaginary part. Therefore, two deeps occur at the resonance frequencies at all gap distances. On the other hand, there also exists a small enhancement band around $1.5^{*}\ 10^{15}$ rad/s. This is due to the m-HM mode as can be seen in Fig. 5.17(b) where the ڍ component is positive and the ضcomponent is negative. Note that, the effect of MNP is still gap distance dependent (about two orders of magnitude difference at the MNP peaks between 0.1μm and 1 μm gap distances) as it is for m-HM mode because both the emitter and the receiver share the same material properties which can further enhance the coupling of modes at the same frequency.

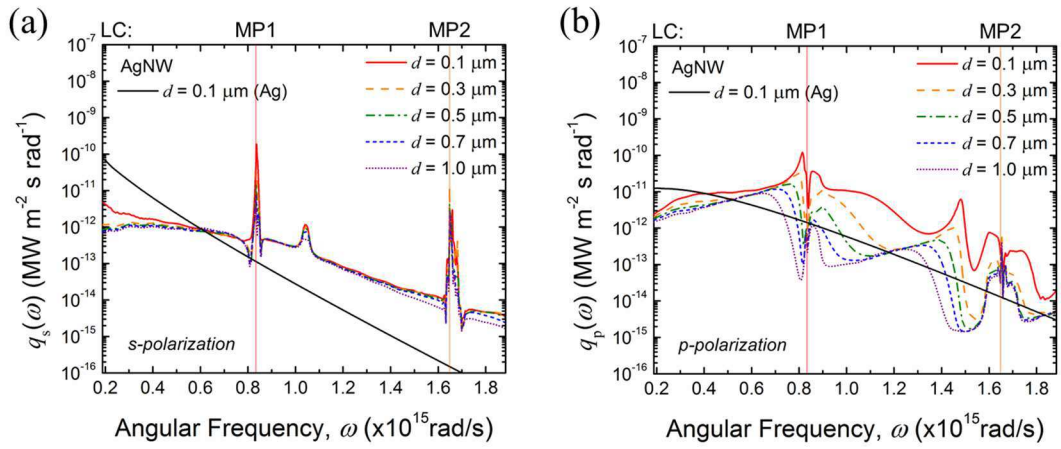

Fig. 5.19 Spectral heat fluxes for (a) s and (b) p wave polarizations at different vacuum gap distances by retrieved properties.

In the cases studied previously, the geometry and the host material (air) are chosen for simplicity so that the MP peaks are distinct for understanding the underlying physics. Now, what if one requires multiple enhancement peaks within a frequency range? Figure 5.20 shows the retrieved material properties and spectral heat flux between two Al_2O_3 hosted Ag nanowire arrays. In order to push the higher harmonic terms of MP closer to each other, the geometry is chosen with only 20 nm distance between nanowires and the period is 200 nm. The height (sample thickness) of the nanowires is still 1 μm. As shown in Figs. 5.20(a) and 5.20(b), MP harmonic terms cause four MNP and anti-ENP peaks to μ_x, μ_z and ε_x, respectively. As explained previously for ε_z no metallic behavior as EMT prediction can be seen here due to the massive interactions between nanowires. As for the corresponding spectral heat flux, several enhancement peaks and deeps show up as expected in Figs. 5.20(c) and 5.20(d). These spectral heat flux peaks are in general about one order of magnitude higher than that away from the resonance frequencies. Furthermore,

the spectral heat flux between metamaterials is stronger than that between two plane Ag plates and two Al_2O_3 plates throughout the investigated spectrum.

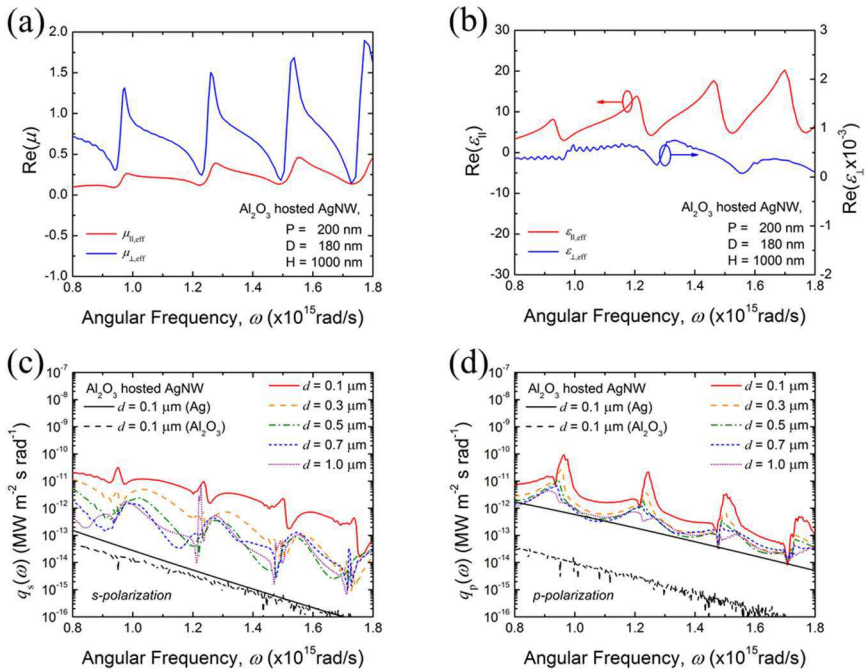

Fig. 5.20 Uniaxial (a) permeability and (b) permittivity retrieved by parameter retrieval and the spectral heat fluxes for (c) s and (d) p wave polarizations at different vacuum gap distances by retrieved properties.

CHAPTER 6 CONCLUSIONS AND RECOMMENDATIONS

6.1 Conclusions

In summary, this PhD dissertation investigated the radiative heat transfer between nanowire/nanohole structures in both far-field and near-field in terms of their electrical and magnetic responses. The underlying mechanisms, physical meanings, theoretical models, and experimental results are organized in each chapter.

In chapter 2, we have designed and studied nanowire based metamaterials as broadband selective absorbers for solar energy harvesting systems. With FDTD simulation, the radiative properties of selective absorber were investigated. In comparison with the FDTD results, the EMT fails to predict the MP resonance and the absorption peaks accurately. The selective absorption is realized by the excitation of multiple harmonic MP modes between nanowires. The underlying physical mechanism has been explained by the LC circuit and EM field distribution. By tuning the geometric parameters, the MP resonance could occur at desired wavelengths for different purposes. On the other hand, the incident angle independency of the selective solar absorber is also demonstrated. In addition, the performance analysis also shows the conversion efficiency of the nanowire based absorber exceeds that of bare tungsten and blackbody absorbers under most conditions and can reach at most 83.58% when the concentration factor reaches 100. The results would facilitate the design of novel low-cost and high-efficiency materials for enhancing the solar energy harvesting and conversion.

In chapter 3, two sets of configurations are theoretically studied for the electrical responses of nanowire/nanohole arrays in the near-field. The near-field radiative flux between the doped SiNH and graphene-covered silicon plate is first theoretically studied.

The enhanced energy transfer is analyzed in detail as due to surface plasmon coupling between the uniaxial metallic metamaterial emitter and graphene-covered receiver. With the help of fluctuational electrodynamics, it is shown that two coupled surface plasmon modes, which are respectively dominated by the SiNH-vacuum and the vacuum-graphene-silicon interfaces, will shift and interact with each other under different doping levels (N_1 and N_2), and graphene chemical potential μ. The different coupling strength between the surface plasmon modes could lead to either enhancement or suppression of near-field radiative heat transfer between the dissimilar materials considered here. With proper tuning of N_1, N_2, and μ values, the near-field heat flux reaches up to 500 times higher than that between two black bodies at vacuum gap d = 20 nm. The results and understanding gained here will facilitate the exploration and application of novel metamaterials for energy conversion and thermal management by means of near-field energy transfer.

Second, we have also calculated the near-field heat transfer between ITO nanowires at different filling ratios using spatial dispersion dependent effective medium theory coupled with fluctuation electrodynamics. The different type of HMM mode contributions at different filling ratios have been clearly illustrated in this study. Interestingly, there exists a critical vacuum gap (150 nm) below which the heat transfer between nanowires increases as filling ratio decreases. For distances greater than the critical gap, the trend of total heat transfer changes due to the drastically drop of type 2 HMM enhancement. The results and understanding gained here will facilitate the exploration and application of novel metamaterials for energy conversion, optoelectronics, and thermal management by means of near-field energy transfer. Results obtained from this study will facilitate the application of nanowires in optoelectronics and energy conversion systems.

In chapter 4, the performance of a near-field TPV system with HMM emitter made of tungsten nanowire embedded in Al_2O_3 host has been thoroughly investigated. The filling ratio effect on the material properties of near-field radiative heat transfer was analyzed. The results show that a semi-infinite HMM emitter with $f = 0.5$ can achieve 2.15 times (1.25 MW/m^2) of enhancement in electrical power output from semi-infinite TPV cell made of $In_{0.2}Ga_{0.8}Sb$ comparing to that with plain tungsten emitter. The mechanisms for radiative heat transfer enhancement have been illustrated as ENP for s polarization and hyperbolic modes for p polarization. However, it turned out that the conversion efficiency becomes lower because the spectral radiative energy below the cell bandgap is also enhanced with the HMM emitter. In order to improve the conversion efficiency, a thin-film TPV cell with $t = 10$ μm is considered. Total internal reflection occurs at the bottom interface of TPV cell and thus minimizes the energy absorption below band gap. As a result, the conversion efficiency has been enhanced from 17.7% to 31.1% with the same amount of power output, compared with 26.7% with a plain tungsten emitter. Furthermore, with a TPV cell thickness of $t = 3$ μm, the conversion efficiency can be further improved to 31.8% where less energy below the bandgap is absorbed, while the nanowire emitter is desired to be opaque. Note that the current theoretical model only considers the near-field radiative transport between the uniaxial nanowire HMM emitter and the TPV cell. In order to accurately predict the near-field quantum efficiency and fully understand the thermal impact on the overall near-field TPV systems enhanced by nanowire HMMs, a rigorous and complete model for near-field radiative transport with multilayer uniaxial media coupled with charge transport and thermal transport is yet to be developed. The results

gained here would facilitate the practical design and demonstration of near-field TPV devices enhanced by novel metamaterial emitters.

In chapter 5, near-field radiative heat transfer between two homogeneous uniaxial electromagnetic metamaterials has first been theoretically investigated. Besides magnetic response, both electrical permittivity and magnetic permeability were considered to be uniaxial. By studying uniaxial metamaterials with two different material property sets, the results showed that, besides the e-HM and coupled e-SPP modes for p polarized waves, m-HM and coupled m-SPP modes also exist for s polarized waves responsible for the near-field spectral heat flux enhancements. Analytical dispersion relations were used to confirm both coupled m-SPP and e-SPP modes at different polarizations. Furthermore, the near-field total heat flux for s polarized waves, which is comparable to that for p polarized waves and thus cannot be neglected for uniaxial electromagnetic metamaterials, can reach at most 6 times higher than that for isotropic magnetic materials at vacuum gaps less than 1 μm.

The mechanisms of near-field radiative heat transfer between two nanowire based uniaxial electromagnetic metamaterials have also been theoretically studied in chapter 5 by both effective medium theory and parameter retrieval. First, instead of the non-magnetic assumption, this study includes the artificial magnetic response associated with s polarized waves which also contributes in spectral heat flux enhancement by applying arbitrary permeability and effective medium theory to obtain uniaxial permeability. The results show that other than the normal e-HM, e-SPP, and MNP modes for p polarized waves, m-HM, m-SPP, and ENP modes are confirmed to exist for s polarized waves. Furthermore, the filling ratio and electrical and magnetic scattering rate effects on the near-field radiative heat transfer were also studied. By tuning these properties, the enhancement bands of

modes can be shifted, broadened, or strengthened depends on the given condition. Moreover, the possibility of achieving ultra-high enhancement by tuning material properties is also investigated as well as the effect of gap distance. As a result, the overall spectral heat flux can reach about two orders of magnitude compared with others by tuning material properties and the contribution of s-polarization should not be excluded at all gap distances since it stands about 25% in total heat flux at all vacuum gap distances.

Next, this study takes the effective medium assumption to a more realistic state. Instead of assuming arbitrary permeability in the optical frequency range which does not naturally exist, applying parameter retrieval gives the homogenized uniaxial material properties base on the actual response of the metamaterial (reflection and transmission coefficients). The results show that when MP is excited between nanowires, the retrieved uniaxial permeability imitates the enhancement by MNPs on both directions which make sense in terms of the incident angle independent and narrow band effect characteristics of MP. Furthermore, the retrieved properties are then imported into near-field calculations to show that the enhancement contributed by artificial magnetic responses does take place and stands an important term in both spectral heat flux and total heat flux. The insights gained here present the possibility of achieving artificial dual uniaxial metamaterials in reality for near-field radiative transfer applications which provides extra tunability on manipulating radiative heat transfer as well as better accuracy on simulations since both electric and magnetic responses are included.

6.2 Recommendations

In order to verify the effect of near-field radiative heat transfer predicted by fluctuational electrodynamics, this section is focused on a sphere-to-plate near-field radiative heat transfer experiment. This is one of the state of the art methods to measure near-field radiative transport at nanometer vacuum gaps. A homemade self-designed AFM staged is used to develop a probe-based metrology for near-field radiation experiments in vacuum. In fact, this metrology is also a foundation of future research since it can be further modified for applications such as near-field scanning optical microscope, near-field infrared spectroscopy, near-field imaging and manufacturing, etc.

6.2.1 Experimental setup and procedure

As depicted in Fig. 6.1, a near-field experiment will be conducted by a self-made AFM. First, the lock-in amplifier will send out a sine wave to the laser controller to modulate the laser signal. Signal modulation can greatly enhance the signal to noise ratio to more accurately measure the temperature by thermoreflectance technique. The modulated laser (Thorlabs, CPS 532) which is collimated by the laser module will pass through an iris to reduce the beam size of the laser. A 50:50 beam splitter is placed after the iris to guide the reflected laser to either a CCD camera (AmScope, MU035) or a position sensitive detector (PSD, On-Trak, PSM with OT-301). The CCD camera (for alignment) and the PSD (for measurement) are both mounted on top of a rail so that the positions are interchangeable as shown in Fig. 6.1(b). A 20X objective will focus the collimated beam to a small spot on the backside of the colloidal AFM probe. The PSD will read the reflected signal (both sum signal and signal difference) and send the signal back to the lock-in amplifier to filtrate the noise. The output of the lock-in amplifier will be

directed to the computer for data acquisition and further analysis. The motorized scanning stage is controlled by the computer to align the sample and the microsphere.

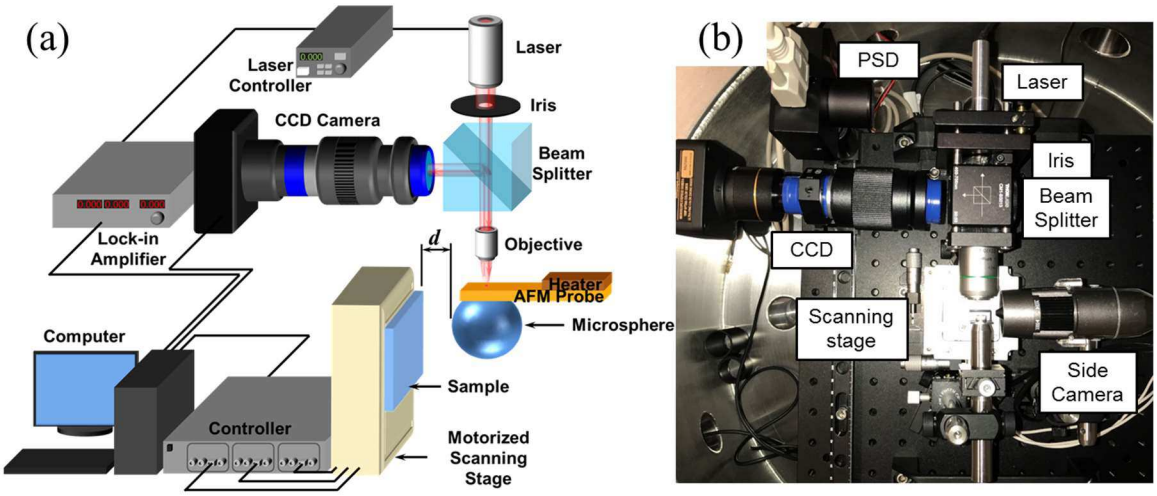

Fig. 6.1 (a) Schematic of near-field radiative heat transfer measurement. (b) Setup of the AFM stage.

Here, other than using the PSD with a bi-material probe to measure the temperature of the AFM probe through monitoring the probe bending position (signal difference), we chose to apply the thermoreflectance technique by monitoring the sum signal. This is because the attachment of microspheres will not be at the same position every time. Therefore, bi-material probe temperature measurements require temperature calibration ahead of all experiments. The thermoreflectance coefficient of the probe will first be obtained through a calibration experiment, which linearizes the relationship between the change of probe temperature and the reflected signal strength [76, 77]. In this way, the temperature of the AFM probe that will be assumed the same as the microsphere can be accurately measured. Meanwhile, the bending of the AFM probe can be used as a reference to double check the accuracy of temperature measurement. The sample will be placed on top of a motorized scanning stage to control the position of the sample through a computer.

Note that the whole setup will be placed in a vacuum chamber to illuminate the effectss of convection and sample contamination. Figure 6.2 shows the instruments for the AFM setup including the laser controller, lock-in amplifier, bell jar vacuum chamber, etc. All the instruments are linked into the vacuum chamber through five KF-40 feedthroughs. A vacuum pump is connected to the bottom of the vacuum chamber by a KF-50 feedthrough. The KF-50 feedthrough at the bottom is the largest feedthrough on the vacuum chamber. It is chosen here so that the pump can work more efficiently when the molecular pump kicks in.

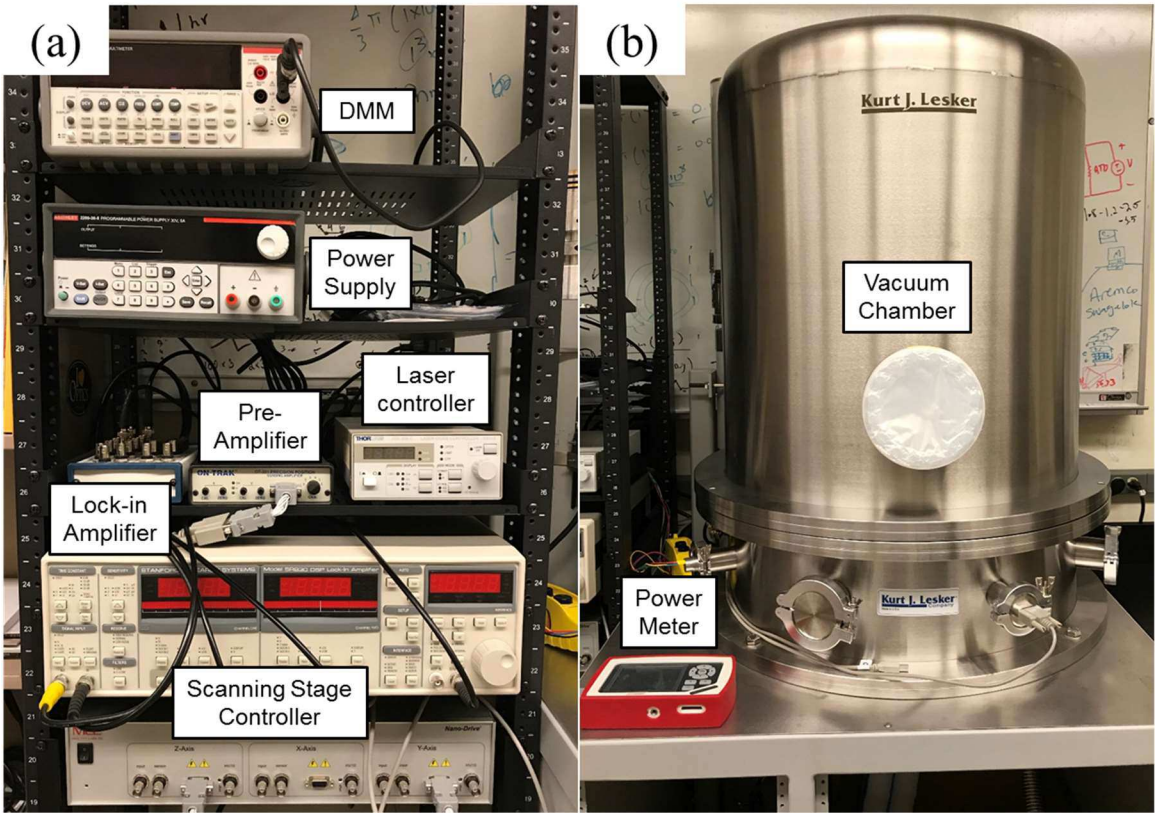

Fig. 6.2 (a) Instruments used for AFM setup. (b) Vacuum chamber for the AFM stage.

The experiment will be conducted by the following procedure:

1) Assemble a colloidal AFM probe by attach a microsphere (100 μm in diameter) to the front side of a tip-less AFM probe.

2) The colloidal probe will be fixed on the probe holder with a heater attached to the backside of the AFM chip (not the probe) to heat up the microsphere.
3) Calibration of both temperature measurements (thermoreflectance and bi-material bending) by sticking an RTD sensor to the front side of the AFM chip.
4) Align the microsphere with the sample by the CCD camera.
5) Slide the PSD in to receive the reflected laser beam for near-field experiment.
6) The scanning stage will bring the sample up to the sphere. After the temperatures of the sphere and the sample reach steady state due to far-field radiation, the temperatures will not change with gap distance except when the effect of near-field radiative heat transfer kicks in [78, 79].
7) By moving the sample closer to the sphere, the temperature will remain constant until a certain point when the temperature of the sphere drops which is caused by near-field radiative heat transfer.
8) A sudden drop of temperature due to conduction as well as a sudden bending of the probe will confirm contact of the sample and the sphere.
9) The gap distance between the sphere and the sample can then be obtained by backward calculation of the position of scanning stage from the contact point.

6.2.2 Colloidal AFM probe assembly

The colloidal AFM probe was first fabricated through Pyro-duct by a simple attaching process [80] as shown in Fig. 6.3. A tipless AFM probe (Nanoandmore, PNP-TR-TL) was controlled by a motion stage to touch a small drop of Pyro-duct, and then pick up a SiO_2 microsphere of 100 μm in diameter (Corpuscular Inc., 140280-10) by capillary adhesion. Pyro-duct can cure under room temperature within about 4 hours.

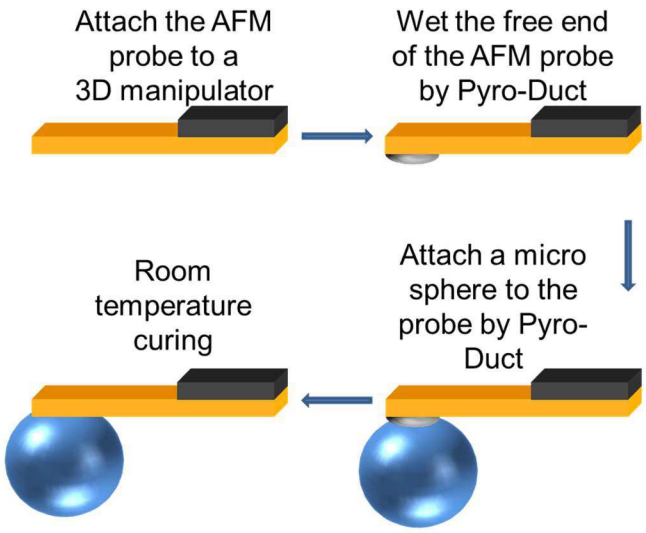

Fig. 6.3 Fabrication steps of the colloidal AFM probe.

As shown in the Fig. 6.4(a), the tipless AFM probe is first attached to a probe holder. A small drop of Pyro-duct will then be dripped on the holder and placed under the probe holder along with a digital USB microscope on top as shown in Figs. 6.4(b) and 6.4(c).

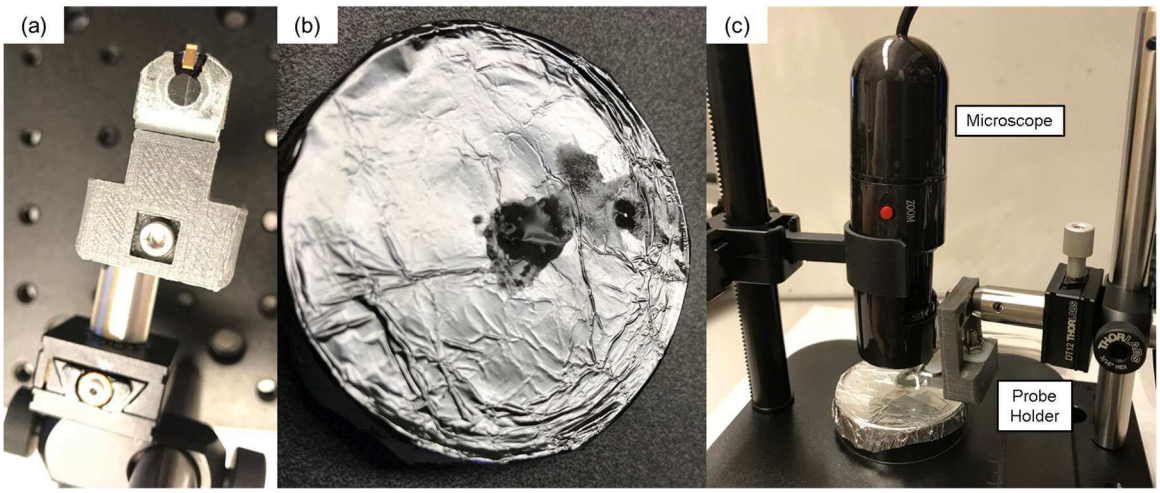

Fig. 6.4 An (a) AFM probe holder and (b) Pyro-duct used on the (c) colloidal AFM probe fabrication stage.

Through focusing the microscope, one can clearly see that the AFM probe is closing the Pyro-duct and eventually dipped in as shown in Fig. 6.5. The microscope is first focused

on the AFM probe to make sure the probe is in sight as shown in Fig 6.5(a). Next, the microscope is focused to the Pyro-duct surface and then start to lower the AFM probe as shown in Figs. 6.5(b) and 6.5(c). With further lowering the AFM probe, one can determine whether if the probe is in contact with Pyro-duct by the light reflection near by the probe due to the change of Pyro-duct surface level as shown in Fig. 6.5(d).

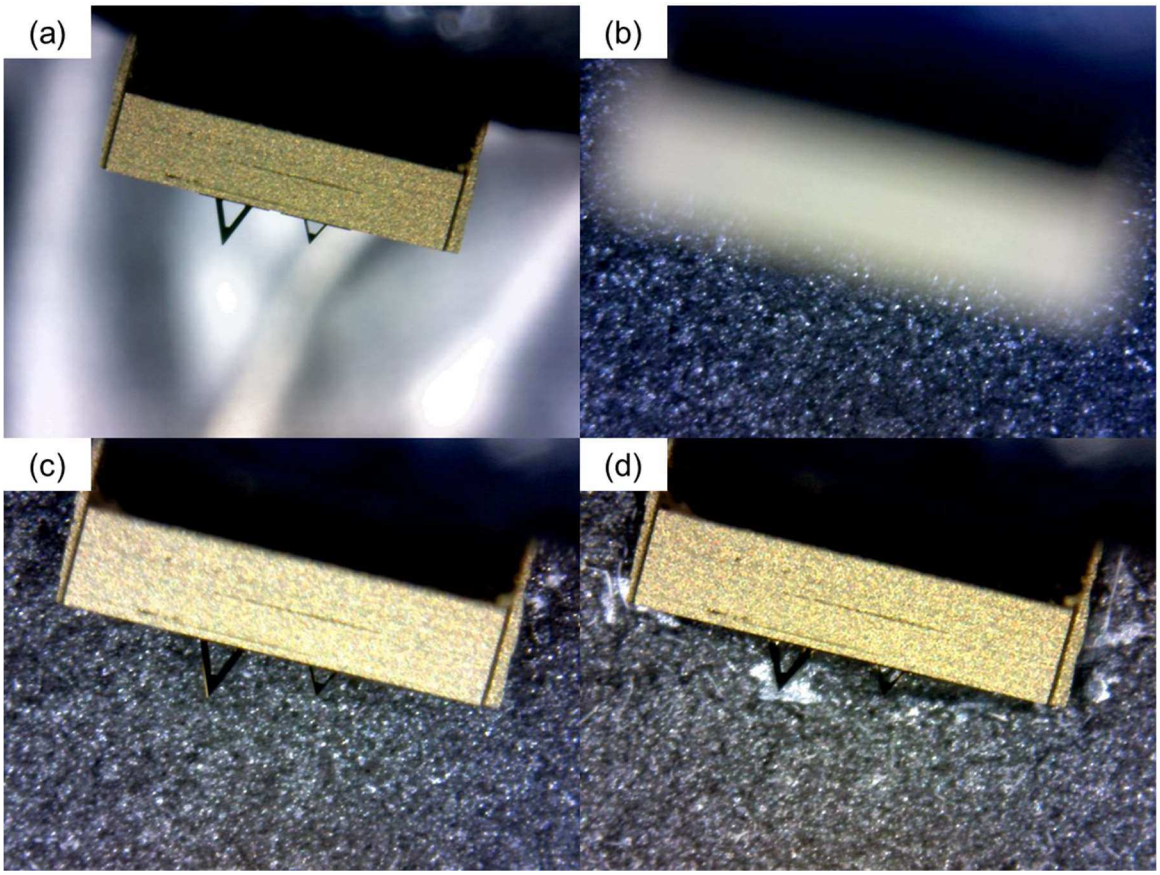

Fig. 6.5 The top views of (a) AFM probe and (b) Pyro-duct; and when the two are (c) approaching and (d) in contact with each other.

After Pyro-duct is pasted onto the bottom of the AFM probe, the probe will be moved away and then SiO_2 microspheres will be placed under the probe. Figure 6.6(a) shows when the microscope is focused on the microspheres. This step is to find a single microsphere and align it with the probe position in case of extra spheres in contact of the

probe as shown in Fig. 6.6(b). Similar to the previous procedure, the probe will then be lowered to make contact with the microsphere. The probe and the microsphere is in contact when the Van der Waals force pull the probe down and light reflection takes place on top to the probe as shown in Fig. 6.6(c). The probe must be further lowered until the reflection is gone to make sure a better contact between the probe and the sphere during curing process as they are under the same height. Note that, the angle of the probe can be checked by comparing the light reflection on the small probe on the right.

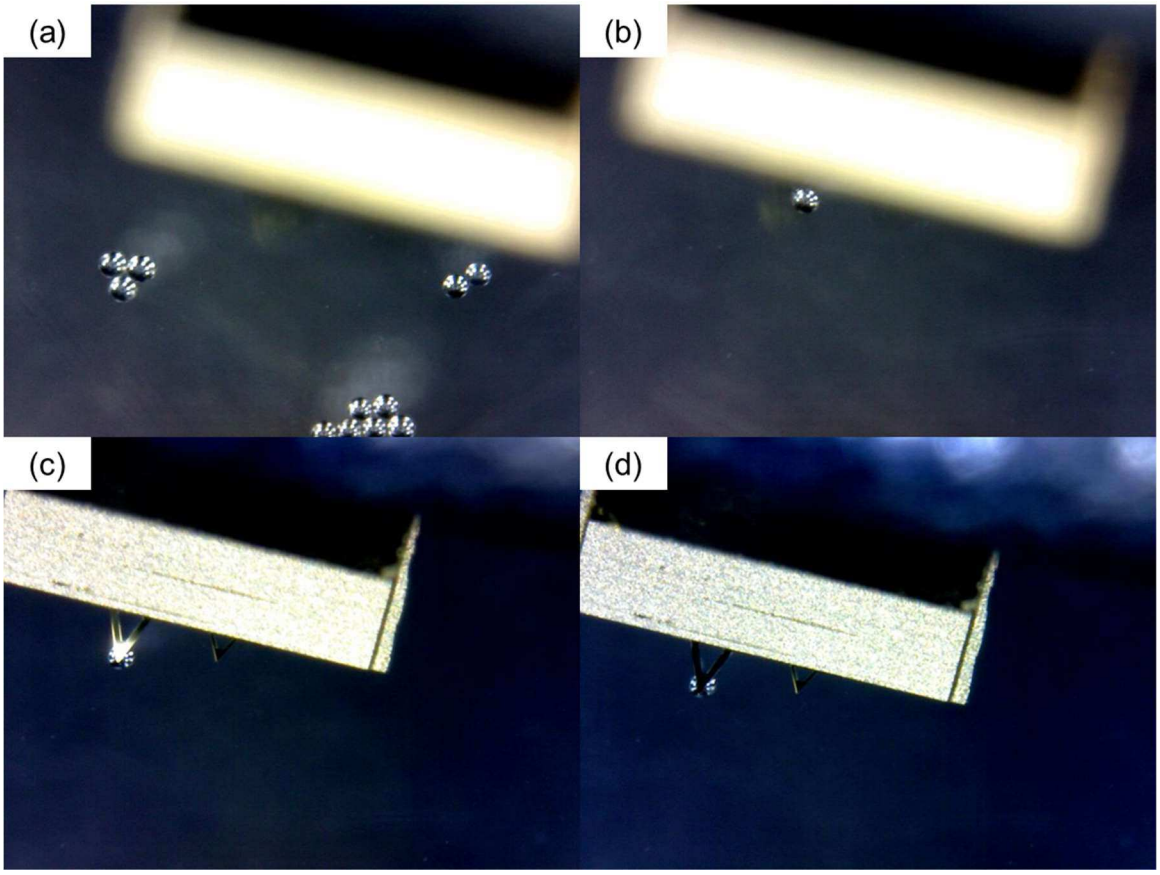

Fig. 6.6 The pictures of (a) multiple microspheres and (b) a single microsphere; and when the probe is (c) in contact and (d) at the same level with the microsphere.

The microsphere attachment by Pyro-duct works but it turns out the probe and the microsphere is not strongly attached. With some vibration such as lifting or lowering the

bell jar, the sphere will break off easily. Therefore, another approach is presented here. Instead of using Pyro-duct where Pyro-duct particles will precipitate to the bottom and touching the Pyro-duct surface iss not very affective, we chose to use thermal compound (Arctic silver, Ceramique 2). Due to the high viscosity of thermal compound which will easily break the probe, isopropyl alcohol (IPA) was used to mix and to liquefy the compound so that it can be easier to use. IPA will evaporate within few minutes after applied to the AFM tip. To overcome the precipitation issue, a needle was used to apply thermal compound. As shown in Figs. 6.7(a) and 6.7(b), thermal compound was first applied to the tip of a needle and then use the needle to paste thermal compound to the AFM probe. The microsphere attachment is same as the Pyro-duct procedure as shown in Fig. 6.7(c).

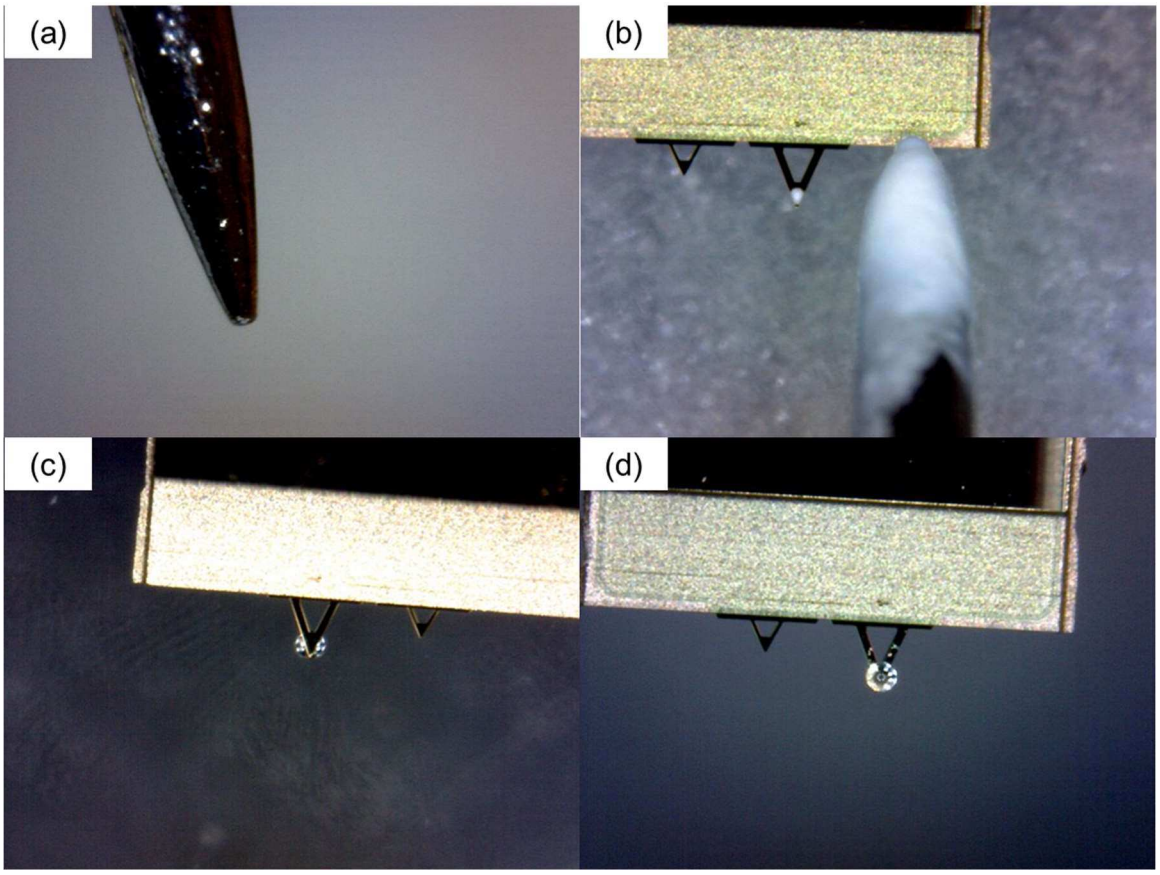

Fig. 6.7 The picutres of (a) needle tip, (b) thermal compound on needle tip, (c) top view of microsphere attached probe, and (d) bottom view of microsphere attached probe.

6.2.3 Temperature measurement calibration.

As shown in Fig. 6.8(a), a flexible heater (Heat Scientific LLC, HS-PS017012) is attached to the probe holder so that the AFM chip can be heated by the heater. Even though the heater is much larger than the AFM chip that results in low heating efficiency, heating is still efficient since the targeted temperature difference is only about 10 ∽ at this point. A RTD will be stuck to the bottom of the AFM chip to measure the temperature of the chip during heating as shown in Figs. 6.8(b) and 6.8(c). The white part on the RTD in Fig. 6.8 (b) is where thermal compound was applied to reduce thermal contact resistance. The calibration will be conducted through the following procedure:

1) Align the probe and the laser; focus the laser spot to the back side of the probe.
2) Turn on the power supply of the flexible heater and set the current as 0.05A.
3) Wait until the temperature of the probe reaches steady state and record the sum signal and the signal difference read from the PSD along with the temperature reading of the probe.
4) Repeat the experiment by different current input with an interval of 0.05A until the current reaches 0.5A or the probe reaches 40∽.
5) Use the obtained temperature and sum signal relationship to obtain the thermoreflectance coefficient of gold. (Green laser is chosen here to aim for a larger coefficient which gives better temperature measurement resolution)

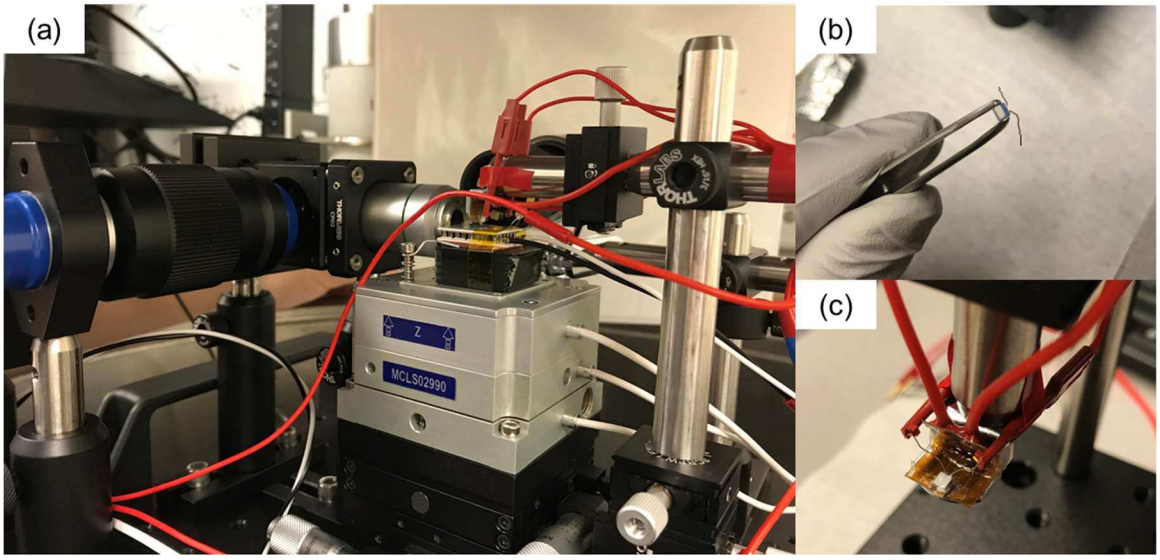

Fig. 6.8 Pictures of (a) heater installed on the AFM stage, (b) RTD sensor with Pyro-duct on top, and (c) RTD attached to the bottom of the AFM chip.

As shown in Figs. 6.9(a-c), green laser (I_{in} = 128 mA) can be aligned with the probe. However, the focus of the laser and the optical microscope is not the same. Therefore, when the optical microscope is focused as shown in Fig. 6.9(a), the laser spot is actually much bigger than that in Figs. 6.9(b) and 6.9(c) when laser is focused. After a microsphere is attached to the probe for near-field experiments as shown in Fig. 6.9(d), laser spot is aligned and focused to the backside of the probe. Note that, the laser current input during the actual experiment is 140 mA as stronger signal gives better temperature resolution. However, even though the current input limit is 220 mA for the laser module, 140 mA is still chosen for higher signal stability. In other words, since water-cooling costs vibration and no cooling results in high laser temperature that affects the laser power output, 140 mA is the highest current input that does not require cooling to stabilize power output.

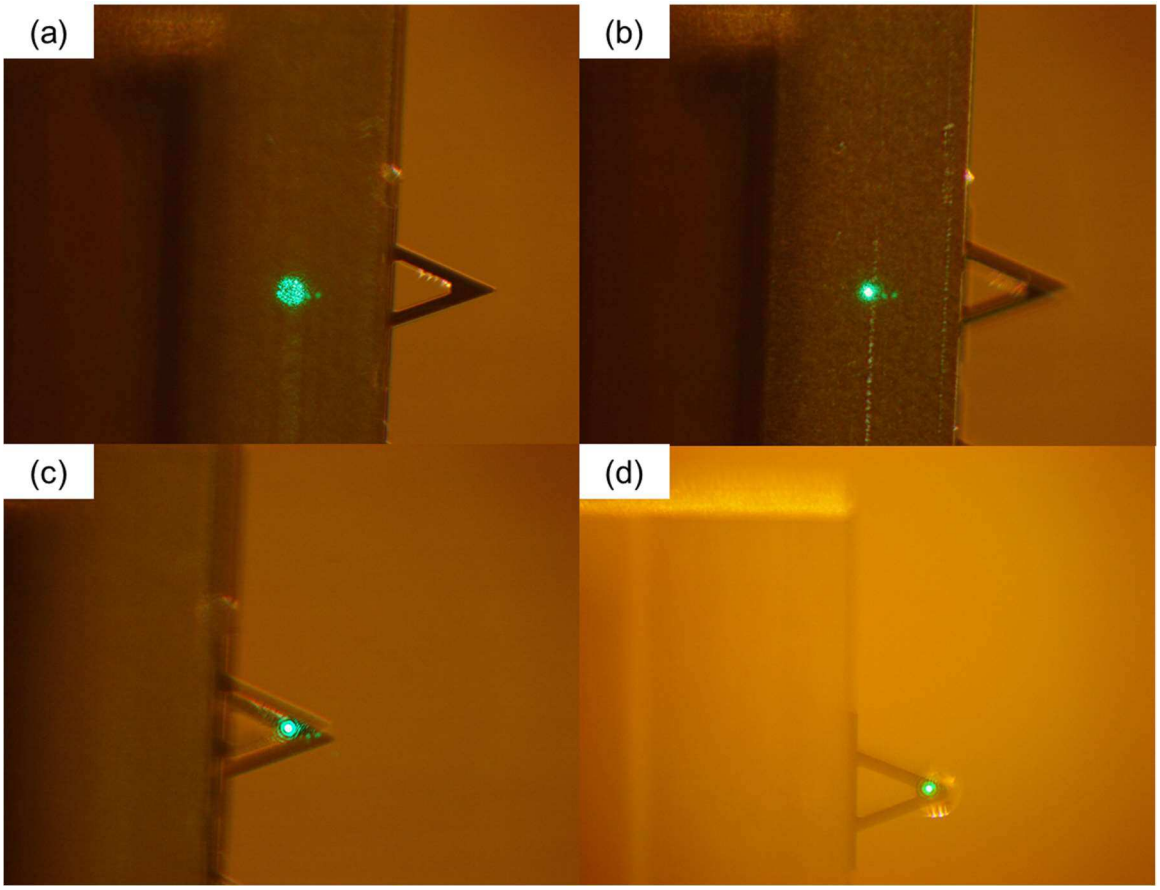

Fig. 6.9 Top views of (a) AFM probe, (b) focused laser spot, (c) focused laser spot on the back side of the probe, and (d) laser focused on a microsphere attached probe.

The near-field experiment will be conducted right after the temperature calibration so that the laser focus and setup are all remained the same. The experiment is not performed by heating up the AFM probe and thereby the microsphere here; it is designed by cooling down the glass receiver. This is because heating the probe to a higher temperature usually requires larger input heat flow because of the thermal conductivity of gold and chromium, which might overcomes the near-field heat flux and result in nearly no change of probe temperature. Therefore, as shown in Fig. 6.8(a), a thermoelectric (TE) cooler (Thorlabs, TEC3-6) is placed under a glass receiver. The copper plate under the hot side of the TE cooler is for spreading the heat and the glass holder at the bottom is to prevent heating up

the motorized stage, as it is temperature sensitive. There is no heat sink included here so that the vibration of water cooler can be avoided. Again, as the temperature difference between the emitter and receiver is at the range of about 10ب, the heat sink is not required. When the temperature of the cold side reaches around 5ب, the hot side reaches about 35ب without a heat sink witch is still acceptable for the setup. An alternative way is to use a sheet of aluminum foil to link the vacuum chamber (can be used as heat sink) and the hot side of the TE cooler to dissipate heat. Note that the probe was initially placed within 100 μm of the glass receiver since the working distance of the motorized stage is around 110 μm. However, due to the parts that are used on the AFM stage being not fully vacuum compatible, the outgassing of these equipment stops the pumping at $1^{*}\ 10^{-2}$ torr. In fact, the pressure goes back to 2.5 torr after it reaches the minimum value. The experiment can be continued by replacing the non-vacuum compatible parts such as all manual control stages, etc.

REFERENCES

[1] Wang, H. and L. Wang, *Tailoring thermal radiative properties with film-coupled concave grating metamaterials.* Journal of Quantitative Spectroscopy and Radiative Transfer, 2015. **158**: p. 127-135.

[2] Zhang, Z.M., *Nano/microscale heat transfer*. 2007: McGraw-Hill New York.

[3] Vasilantonakis, N., et al., *Bulk plasmon-polaritons in hyperbolic nanorod metamaterial waveguides.* Laser & Photonics Reviews, 2015. **9**(3): p. 345-353.

[4] Gorkunov, M.V., et al., *Implications of the causality principle for ultra chiral metamaterials.* Scientific Reports, 2015. **5**: p. 9273.

[5] Liu, X., R.Z. Zhang, and Z. Zhang, *Near-Perfect Photon Tunneling by Hybridizing Graphene Plasmons and Hyperbolic Modes.* ACS Photonics, 2014. **1**(9): p. 785-789.

[6] Molesky, S., C.J. Dewalt, and Z. Jacob, *High temperature epsilon-near-zero and epsilon-near-pole metamaterial emitters for thermophotovoltaics.* Optics Express, 2013. **21**(S1): p. A96-A110.

[7] Wang, H. and L. Wang, *Perfect selective metamaterial solar absorbers.* Optics Express, 2013. **21**(S6): p. A1078-A1093.

[8] Wang, H., K. O'Dea, and L. Wang, *Selective absorption of visible light in film-coupled nanoparticles by exciting magnetic resonance.* Optics Letters, 2014. **39**(6): p. 1457-1460.

[9] Johnson, J.C., et al., *Near-Field Imaging of Nonlinear Optical Mixing in Single Zinc Oxide Nanowires.* Nano Letters, 2002. **2**(4): p. 279-283.

[10] Sacchetto, D., et al., *New Insight on Bio-sensing by Nano-fabricated Memristors.* BioNanoScience, 2011. **1**(1-2): p. 1-3.

[11] Wang, H., Y. Yang, and L. Wang, *Switchable wavelength-selective and diffuse metamaterial absorber/emitter with a phase transition spacer layer.* Applied Physics Letters, 2014. **105**(7): p. 071907.

[12] Bright, T.J., X.L. Liu, and Z.M. Zhang, *Energy streamlines in near-field radiative heat transfer between hyperbolic metamaterials.* Optics Express, 2014. **22**(S4): p. A1112-A1127.

[13] Biehs, S.A., et al., *Nanoscale heat flux between nanoporous materials.* Optics Express, 2011. **19**(S5): p. A1088-A1103.

[14] Liu, B. and S. Shen, *Broadband near-field radiative thermal emitter/absorber based on hyperbolic metamaterials: Direct numerical simulation by the Wiener chaos expansion method.* Physical Review B, 2013. **87**(11): p. 115403.

[15] Liu, X.L., L.P. Wang, and Z.M. Zhang, *Wideband Tunable Omnidirectional Infrared Absorbers Based on Doped-Silicon Nanowire Arrays.* Journal of Heat Transfer, 2013. **135**(6): p. 061602-061602.

[16] Liu, X.L. and Z.M. Zhang, *Metal-free low-loss negative refraction in the mid-infrared region.* Applied Physics Letters, 2013. **103**(10): p. -.

[17] Wang, L.P. and Z.M. Zhang, *Measurement of Coherent Thermal Emission Due to Magnetic Polaritons in Subwavelength Microstructures.* Journal of Heat Transfer, 2013. **135**(9): p. 091505-091505.

[18] Sakurai, A., B. Zhao, and Z.M. Zhang, *Resonant frequency and bandwidth of metamaterial emitters and absorbers predicted by an RLC circuit model.* Journal of Quantitative Spectroscopy and Radiative Transfer, 2014. **149**: p. 33-40.

[19] Zhao, B., J.M. Zhao, and Z.M. Zhang, *Enhancement of near-infrared absorption in graphene with metal gratings.* Applied Physics Letters, 2014. **105**(3): p. 031905.

[20] Wang, L. and Z.M. Zhang, *Effect of magnetic polaritons on the radiative properties of double-layer nanoslit arrays.* Journal of the Optical Society of America B, 2010. **27**(12): p. 2595-2604.

[21] Wang, L., A. Haider, and Z. Zhang, *Effect of magnetic polaritons on the radiative properties of inclined plate arrays.* Journal of Quantitative Spectroscopy and Radiative Transfer, 2014. **132**: p. 52-60.

[22] Park, K., et al., *Performance analysis of near-field thermophotovoltaic devices considering absorption distribution.* Journal of Quantitative Spectroscopy and Radiative Transfer, 2008. **109**(2): p. 305-316.

[23] Chang, J.-Y., Y. Yang, and L. Wang, *Tungsten nanowire based hyperbolic metamaterial emitters for near-field thermophotovoltaic applications.* International Journal of Heat and Mass Transfer, 2015. **87**: p. 237-247.

[24] Yang, Y., S. Basu, and L. Wang, *Radiation-based near-field thermal rectification with phase transition materials.* Applied Physics Letters, 2013. **103**(16): p. -.

[25] Yang, Y., S. Basu, and L. Wang, *Vacuum thermal switch made of phase transition materials considering thin film and substrate effects.* Journal of Quantitative Spectroscopy and Radiative Transfer, 2015. **158**: p. 69-77.

[26] Basu, S. and L.P. Wang, *Near-field radiative heat transfer between doped silicon nanowire arrays.* Applied Physics Letters, 2013. **102**(5): p. 4.

[27] Liu, X., L. Wang, and Z.M. Zhang, *Near-Field Thermal Radiation: Recent Progress and Outlook.* Nanoscale and Microscale Thermophysical Engineering, 2015. **19**(2): p. 98-126.

[28] Park, K. and Z. Zhang, *FUNDAMENTALS AND APPLICATIONS OF NEAR-FIELD RADIATIVE ENERGY TRANSFER.* Frontiers in Heat and Mass Transfer (FHMT), 2013. **4**(1).

[29] Basu, S., Z.M. Zhang, and C.J. Fu, *Review of near-field thermal radiation and its application to energy conversion.* International Journal of Energy Research, 2009. **33**(13): p. 1203-1232.

[30] Shen, S., A. Narayanaswamy, and G. Chen, *Surface Phonon Polaritons Mediated Energy Transfer between Nanoscale Gaps.* Nano Letters, 2009. **9**(8): p. 2909-2913.

[31] van Zwol, P., et al., *Phonon polaritons enhance near-field thermal transfer across the phase transition of VO2.* Physical Review B, 2011. **84**(16): p. 161413.

[32] Guo, Y., et al., *Broadband super-Planckian thermal emission from hyperbolic metamaterials.* Applied Physics Letters, 2012. **101**(13): p. -.

[33] Guo, Y., et al., *Applications of Hyperbolic Metamaterial Substrates.* Advances in OptoElectronics, 2012. **2012**: p. 9.

[34] Jacob, Z., *Quantum plasmonics.* MRS Bulletin, 2012. **37**(08): p. 761-767.

[35] Cortes, C.L., et al., *Quantum nanophotonics using hyperbolic metamaterials.* Journal of Optics, 2012. **14**(6): p. 063001.

[36] Wang, L. and Z. Zhang, *Resonance transmission or absorption in deep gratings explained by magnetic polaritons.* Applied Physics Letters, 2009. **95**(11): p. 111904-111904-3.

[37] Wang, L.P. and Z.M. Zhang, *Wavelength-selective and diffuse emitter enhanced by magnetic polaritons for thermophotovoltaics.* Applied Physics Letters, 2012. **100**(6): p. 063902.

[38] Smith, D., et al., *Handbook of Optical constants of Solids.* Palik (Ed.)(Academic, Orlando 1985) p, 1985. **398**: p. 74.

[39] Wang, H., et al., *Anisotropic optical properties of silicon nanowire arrays based on the effective medium approximation.* International Journal of Thermal Sciences, 2013. **65**(0): p. 62-69.

[40] Choy, T.C., *Effective medium theory: principles and applications*. Vol. 102. 1999: Oxford University Press.

[41] Hassel, A.W., A.J. Smith, and S. Milenkovic, *Nanostructures from directionally solidified NiAl–W eutectic alloys.* Electrochimica Acta, 2006. **52**(4): p. 1799-1804.

[42] Lee, B., L. Wang, and Z. Zhang, *Coherent thermal emission by excitation of magnetic polaritons between periodic strips and a metallic film.* Optics Express, 2008. **16**(15): p. 11328-11336.

[43] Zhao, B. and Z.M. Zhang, *Study of magnetic polaritons in deep gratings for thermal emission control.* Journal of Quantitative Spectroscopy and Radiative Transfer, 2014. **135**: p. 81-89.

[44] Wang, L.P. and Z.M. Zhang, *Phonon-mediated magnetic polaritons in the infrared region.* Optics Express, 2011. **19**(S2): p. A126-A135.

[45] Rytov, S.M.K.s.o.I.U.r.A.T.V.I., *Principles of statistical radiophysics. 2, 2*. 1988, Berlin; New York: Springer-Verlag.

[46] Basu, S. and M. Francoeur, *Maximum near-field radiative heat transfer between thin films.* Applied Physics Letters, 2011. **98**(24): p. -.

[47] Francoeur, M., M.P. Mengüç, and R. Vaillon, *Spectral tuning of near-field radiative heat flux between two thin silicon carbide films.* Journal of Physics D: Applied Physics, 2010. **43**(7): p. 075501.

[48] Liu, X.L., R.Z. Zhang, and Z.M. Zhang, *Near-field thermal radiation between hyperbolic metamaterials: Graphite and carbon nanotubes.* Applied Physics Letters, 2013. **103**(21): p. -.

[49] Basu, S., B.J. Lee, and Z.M. Zhang, *Infrared Radiative Properties of Heavily Doped Silicon at Room Temperature.* Journal of Heat Transfer, 2009. **132**(2): p. 023301-023301.

[50] Lim, M., S.S. Lee, and B.J. Lee, *Near-field thermal radiation between graphene-covered doped silicon plates.* Optics Express, 2013. **21**(19): p. 22173-22185.

[51] Falkovsky, L.A., *Optical properties of graphene.* Journal of Physics: Conference Series, 2008. **129**(1): p. 012004.

[52] Messina, R., et al., *Tuning the electromagnetic local density of states in graphene-covered systems via strong coupling with graphene plasmons.* Physical Review B, 2013. **87**(8): p. 085421.

[53] Liu, X.L. and Z.M. Zhang, *Graphene-assisted near-field radiative heat transfer between corrugated polar materials.* Applied Physics Letters, 2014. **104**(25): p. -.

[54] Basu, S., B.J. Lee, and Z.M. Zhang, *Near-Field Radiation Calculated With an Improved Dielectric Function Model for Doped Silicon.* Journal of Heat Transfer, 2009. **132**(2): p. 023302-023302.

[55] Belov, P., et al., *Strong spatial dispersion in wire media in the very large wavelength limit.* Physical Review B, 2003. **67**(11): p. 113103.

[56] Mirmoosa, M.S., et al., *Effective-medium model of wire metamaterials in the problems of radiative heat transfer.* Journal of Applied Physics, 2014. **115**(23): p. -.

[57] Silveirinha, M., *Nonlocal homogenization model for a periodic array of ϵ-negative rods.* Physical Review E, 2006. **73**(4): p. 046612.

[58] Simovski, C., et al., *Optimization of radiative heat transfer in hyperbolic metamaterials for thermophotovoltaic applications.* Optics Express, 2013. **21**(12): p. 14988-15013.

[59] Rhodes, C., et al., *Dependence of plasmon polaritons on the thickness of indium tin oxide thin films.* Journal of Applied Physics, 2008. **103**(9): p. -.

[60] Basu, S., Y.B. Chen, and Z.M. Zhang, *Microscale radiation in thermophotovoltaic devices—A review.* International Journal of Energy Research, 2007. **31**(6-7): p. 689-716.

[61] Asoh, H., et al., *Fabrication of ideally ordered anodic porous alumina with 63 nm hole periodicity using sulfuric acid.* Journal of Vacuum Science & Technology B, 2001. **19**(2): p. 569-572.

[62] Kartopu, G. and O. Yalçın, *Fabrication and Applications of Metal Nanowire Arrays Electrodeposited in Ordered Porous Templates*. Electrodeposited Nanowires and their Applications. 2010.

[63] Lee, W., et al., *Wafer-Scale Ni Imprint Stamps for Porous Alumina Membranes Based on Interference Lithography.* Small, 2006. **2**(8-9): p. 978-982.

[64] Bright, T.J., L.P. Wang, and Z.M. Zhang, *Performance of Near-Field Thermophotovoltaic Cells Enhanced With a Backside Reflector.* Journal of Heat Transfer, 2014. **136**(6): p. 062701-062701.

[65] Francoeur, M., R. Vaillon, and M. Menguc, *Thermal impacts on the performance of nanoscale-gap thermophotovoltaic power generators.* Energy Conversion, IEEE Transactions on, 2011. **26**(2): p. 686-698.

[66] Davis, C.C., *Lasers and electro-optics: fundamentals and engineering*. 2014: Cambridge University Press.

[67] Basu, S. and M. Francoeur, *Near-field radiative heat transfer between metamaterial thin films.* Optics Letters, 2014. **39**(5): p. 1266-1269.

[68] Pendry, J.B., et al., *Magnetism from conductors and enhanced nonlinear phenomena.* Microwave Theory and Techniques, IEEE Transactions on, 1999. **47**(11): p. 2075-2084.

[69] Liu, X.L., T.J. Bright, and Z.M. Zhang, *Application Conditions of Effective Medium Theory in Near-Field Radiative Heat Transfer Between Multilayered Metamaterials.* Journal of Heat Transfer, 2014. **136**(9): p. 092703-092703.

[70] Biehs, S.-A., M. Tschikin, and P. Ben-Abdallah, *Hyperbolic Metamaterials as an Analog of a Blackbody in the Near Field.* Physical Review Letters, 2012. **109**.

[71] Wang, X.J., et al., *Angle-resolved reflectance of obliquely aligned silver nanorods.* Applied Optics, 2012. **51**(10): p. 1521-1531.

[72] Orlov, A.A., et al. *Retrieving constitutive parameters of plasmonic multilayers from reflection and transmission coefficients*. in *2014 8th International Congress on Advanced Electromagnetic Materials in Microwaves and Optics*. 2014.

[73] Menzel, C., et al., *Retrieving effective parameters for metamaterials at oblique incidence.* Physical Review B, 2008. **77**(19): p. 195328.

[74] Papadakis, G.T., P. Yeh, and H.A. Atwater, *Retrieval of material parameters for uniaxial metamaterials.* Physical Review B, 2015. **91**(15): p. 155406.

[75] Zhou, J., et al., *Unifying approach to left-handed material design.* Optics Letters, 2006. **31**(24): p. 3620-3622.

[76] Kim, J., et al., *Temperature measurements of heated microcantilevers using scanning thermoreflectance microscopy.* Review of Scientific Instruments, 2013. **84**(3): p. 034903.

[77] Park, H., B.J. Lee, and J. Lee, *Note: Simultaneous determination of local temperature and thickness of heated cantilevers using two-wavelength thermoreflectance.* Review of Scientific Instruments, 2014. **85**(3): p. 036109.

[78] Narayanaswamy, A., S. Shen, and G. Chen, *Near-field radiative heat transfer between a sphere and a substrate.* Physical Review B, 2008. **78**(11): p. 115303.

[79] Shi, J., et al., *Near-Field Energy Extraction with Hyperbolic Metamaterials.* Nano Letters, 2015. **15**(2): p. 1217-1221.

[80] Gan, Y., *Invited Review Article: A review of techniques for attaching micro- and nanoparticles to a probe's tip for surface force and near-field optical measurements.* Review of Scientific Instruments, 2007. **78**(8): p. 081101.

APPENDIX A

DISSERTATION RELATED JOURNAL PUBLICATION LIST

1. **Chang, J.-Y.** and Wang, L.P., 2017, "Near-Field Radiative Heat Transfer between a Plate and a Sphere by Thermoreflectance Technique," in preparation.
2. **Chang, J.-Y.**, Sabbaghi P., and Wang, L.P., 2017, "Parameter Retrieval of Uniaxial Permittivity and Permeability for the Study of Near-field Radiative Transport between Nanowire-based Magneto-dielectric Metamaterials," to be submitted.
3. **Chang, J.-Y.**, Taylor S., and Wang, L.P., 2017, "Selective Solar Absorber Made of Silicon-cored Tungsten Nanowires," to be submitted.
4. **Chang, J.-Y.**, Sabbaghi P., and Wang, L.P., 2017, "Near-Field Thermal Radiation between Nanowire Based Dual Uniaxial Electromagnetic Metamaterials," *Optics Communications*, Submitted.
5. **Chang, J.-Y.**, Yang, Y., and Wang, L.P., 2016, "Enhanced Energy Transfer by Near-Field Coupling of a Nanostructured Metamaterial with a Graphene-Covered Dielectric Plate," *Journal of Quantitative Spectroscopy and Radiative Transfer*, Vol. 184, pp. 58-67.
6. **Chang, J.-Y.**, Wang, H., and Wang, L.P., 2016, "Tungsten Nanowire Metamaterials as Selective Solar Thermal Absorbers by Excitation of Magnetic Polaritons," *ASME Journal of Heat Transfer*, Vol. 139, p. 052401.
7. **Chang, J.-Y.**, Basu, S., Yang, Y., and Wang, L.P., 2016, "Near-field Radiation between Dual Uniaxial Electromagnetic Metamaterials," *Journal of Applied Physics*, Vol. 119, p. 213108.
8. **Chang, J.-Y.**, Yang, Y., and Wang, L.P., 2015, "Tungsten Nanowire Based Hyperbolic Metamaterial Emitters for Near-Field Thermophotovoltaic Applications," *International Journal of Heat and Mass Transfer*, Vol. 87, pp. 237-247.
9. **Chang, J.-Y.**, Basu, S., and Wang, L.P., 2015, "ITO Nanowires as Hyperbolic Metamaterials for Near-field Radiative Heat Transfer," *Journal of Applied Physics*, Vol. 117, p. 054309.

APPENDIX B

DISSERTATION NON-RELATED JOURNAL PUBLICATION LIST

1. Sabbaghi P., Lambert, L., **Chang, J.-Y.** and Wang, L.P., 2017, "Near-Field Radiative Heat Transfer between Multilayered Metamaterials Separated by Polystyrene Particles," in preparation.
2. Ying X., Long, L.S., **Chang, J.-Y.** and Wang, L.P., 2017, "Measurement of Graphene Enhanced Tunable Near-Field Radiative Heat Transfer," in preparation.
3. Taylor S., **Chang, J.-Y.**, and Wang, L.P., 2017, "Materials Characterizations of Vanadium Dioxide Thin Films Fabricated from Thermal Oxidation Method," to be submitted.
4. Wang, H., **Chang, J.-Y.**, Yang, Y., and Wang, L.P., 2016, "Performance Analysis of Solar Thermophotovoltaic Conversion Enhanced by Selective Metamaterial Absorbers and Emitters," *International Journal of Heat and Mass Transfer*, Vol. 98, pp. 788-798.
5. Yang, Y., **Chang, J.-Y.**, Sabbaghi, P., and Wang, L.P., 2016, "Performance Analysis of a Near-Field Thermophotovoltaic Device with a Metallodielectric Selective Emitter and Electrical Contacts for the Photovoltaic Cell," *ASME Journal of Heat Transfer*, Vol. 139, p. 052701.

BIOGRAPHICAL SKETCH

JUI-YUNG CHANG

Jui-Yung Chang was born in Taipei, Taiwan in 1983. He received both his Bachelor's and master's degree from Tam Kang University in mechanical engineering respectively in 2005 and 2009. Jui-Yung was awarded a scholarship for outstanding academic performance during his master study. In the meantime, Jui-Yung was also selected as a lecturer for engineering mathematics by the ministry of education due to his outstanding outcome on his teaching assistant positions. In fall 2012, Jui-Yung entered the School for Engineering of Matter, Transport and Energy at Arizona State University as a PhD student. He joined Prof. Liping Wang's group in the area of nanoscale radiative heat transfer since spring 2013. His research focuses on the radiative heat transfer between nanowire/nanohole metamaterials for thermal energy harvesting applications in both far and near fields.

During his PhD study, he has published over 10 journal papers listed below in *Journal of Quantitative Spectroscopy and Radiative Transfer*, *International Journal of heat and Mass Transfer*, *Journal of Applied Physics*, and other peer-reviewed journals. He has also co-authored 10 conference presentations, and has given several oral and poster presentations in international conferences, such as *3rd International Workshop on Nano-Micro Thermal Radiation*, *ASME 2017 International Mechanical Engineering Congress and Exposition, 8th International Symposium on Radiative Transfer*. He also received the *travel grant award* in 2013, 2014, and 2017 as well as *ASU University Graduate Fellowship* three years in a raw since 2015. Furthermore, he was nominated for the *Outstanding Teaching Assistant Award* in 2017 (to be determined) after working as a teaching assistant for three years in *Experimental mechanical engineering*, *Thermofluids* I, and *Advance Thermodynamics*. Besides, he has been actively contributing to the professional community by reviewing scientific manuscripts such as *Heat Transfer engineering*.